A Feedback Analysis of Outer Hair Cell Dynamics

by
Timothy K. Lu

Submitted to the Department of Electrical Engineering and Computer Science in Partial Fulfillment of the Requirements for the Degrees of Bachelor of Science in Electrical Engineering and Computer Science
and
Master of Engineering in Electrical Engineering and Computer Science
at the
Massachusetts Institute of Technology

May 20, 2003

© 2003 Timothy K. Lu. All rights reserved.

The author hereby grants to M.I.T. permission to reproduce and distribute publicly paper and electronic copies of this thesis and to grant others the right to do so.

Author.....
Department of Electrical Engineering and Computer Science
May 20, 2003

Certified by.....
Rahul Sarpeshkar
Associate Professor of Electrical Engineering
Thesis Supervisor

Accepted by.....
Arthur C. Smith
Chairman, Department Committee on Graduate Theses

MASSACHUSETTS INSTITUTE OF TECHNOLOGY
JUL 3 0 2003
LIBRARIES

BARKER

A Feedback Analysis of Outer Hair Cell Dynamics

by
Timothy K. Lu

Submitted to the
Department of Electrical Engineering and Computer Science

May 20, 2003

In Partial Fulfillment of the Requirements for the Degrees of
Bachelor of Science in Electrical Engineering and Computer Science
and
Master of Engineering in Electrical Engineering and Computer Science

Abstract

Outer hair cells (OHCs) generate active forces in the mammalian cochlea. Acting as cochlear amplifiers, OHCs can counteract viscous drag, generating high gain at characteristic frequencies and allowing for the sharp frequency selectivity and sensitivity observed in mammals. Excitatory displacement of the basilar membrane causes depolarization of OHC membrane potentials which results in contraction. The motor protein prestin is driven by receptor potentials. However, low-pass filtering by the plasma membrane should severely attenuate the receptor potential at high frequencies ($\geq$ 100 kHz) where mammalian hearing has been observed. Thus, an open question is how OHCs can respond at these high frequencies despite their low frequency cutoff. Inspired by the use of feedback in mechanical and electrical systems to accelerate slow poles, I demonstrate that negative feedback from the coupling of two mechanical modes of vibration can lead to a membrane time constant speedup and a sharpening of the mechanical response.

Thesis Supervisor: Rahul Sarpeshkar
Title: Associate Professor of Electrical Engineering

Acknowledgements

An education is never a one man endeavor. There are so many people that have lent me their time and help in support of my educational career.

I would like to thank my thesis supervisor, Prof. Rahul Sarpeshkar, for taking me under his tutelage and showing me what it really means to have a love and passion for science. I am also appreciative of Prof. Peter Dallos' useful advice. I am grateful to my fellow labmates in the Analog VLSI and Biological Systems Group for making me feel welcome and providing me with intellectual (and non-intellectual) stimulation.

I appreciate the guys at Chi Phi for understanding my decision to pursue my graduate degree a year earlier. I may have moved out of the house but I will always be a dedicated brother. Thanks also to my MIT friends for keeping me company at the wee hours of the night and for spending memorable times together.

Thanks to my friends, (in no particular order) Albert, Eugene, Joyce, Amanda, Phyllis, Kevin, Edward Wen, Melinda, Edward Fu, Philip Lee, John King, Powen, Peng, Cat Chen, Austin, Joyce Wang, Philip Sun, and the others which I don't have enough room to name. It is sometimes hard to stay sane at MIT without some people to goof off with.

I am deeply appreciative of Tom Siebel and Siebel Systems for the honor of being named a Siebel Scholar in 2003. Your financial support went a long way in allowing me to pursue my research. Thanks also to the Biological Engineering Division for the Bioengineering Undergraduate Research Award and Johnson & Johnson for their Biomedical Engineering Prize. Your recognition gave me great encouragement.

My parents, Nicky and Sue, and my brother, Jeff, have provided tremendous support despite being thousands of miles away. Thanks for your love and believing in me. Mom and dad, I hope I will make you proud one day. Jeff, good luck in college and I know that you will pursue your interests with all the heart that you can give. My elders, especially Auntie Ming, Auntie Fen-Fen, Uncle C.Y, and my grandfather, Shan-Tung Lu, have always been there for sagacious advice and stories. My cousins have always kept my spirits high and I thank them for that.

To my grandmother, my 奶奶: I am sorry that you had to leave the world before you could see all your grandchildren graduate from college. The four years that I spent living with you in Taipei were some of the most influential times of my life. I learned honesty and compassion from you and I hope that as you watch on our family from Heaven, you are proud and content. We all miss you dearly.

Most of all, I would like to thank God, for without His blessing, I would not be where I am today. I may have strayed many times in the past but I have faith that You will lead me in the right direction. "The Lord is my shepherd, I shall not be in want..."

好仁不好學, 其蔽也愚;

好知不好學, 其蔽也蕩;

好信不好學, 其蔽也賊;

好直不好學, 其蔽也絞;

好勇不好學, 其蔽也亂;

好剛不好學, 其蔽也狂.

論語 17:8

Translation

Adapted from http://www.human.toyogakuen-u.ac.jp/~acmuller/contao/analects.htm
and http://www.confucius.org/lunyu/ed1708.htm

Those who love benevolence instead of learning will be foiled by dim-wittedness;
Those who love wisdom instead of learning will be foiled by aimlessness;
Those who love trustworthiness instead of learning will be foiled by thievery;
Those who love honesty instead of learning will be foiled by betrayal;
Those who love courage instead of learning will be foiled by lack of control;
Those who love persistence instead of learning will be foiled by their own adamancy.

Analects of Confucius 17:8

Table of Contents

List of Figures

List of Equations

List of Equations

1 Introduction

Outer hair cells (OHCs) reside in the organ of Corti in the cochlea and are important for mammalian hearing [1]. Depolarization and hyperpolarization of OHC membrane potentials occur when sound waves trigger mechanical movements in the basilar membrane (BM) and the reticular lamina (RL), which opens or closes ion channels in the stereocilia membrane [2]. Prestin, a transmembrane protein found in OHCs, acts as a molecular motor and causes OHCs to contract in response to depolarization of the membrane potential [2]. It is believed that OHCs act as "cochlear amplifiers" by timing changes in cell length to provide mechanical feedback, amplifying soft sounds and sharpening frequency selectivity at their particular location in the cochlea [3]. Since spontaneous otoacoustic emissions that are attributed to mammalian OHC motility have been observed up to at least 100 kHz and some mammals can hear sounds up to 100 kHz, outer hair cell contraction and elongation is expected to work up to 100 kHz [3]. Furthermore, the mechanical operation of the motor protein of OHCs has been shown to function up to at least 79 kHz without much decrease in performance [4]. However, severe attenuation of the membrane potential by low-pass filtering imposed by the cell membrane at high frequencies suggests that OHC receptor potentials are insufficient to drive a mechanical response. Thus, an open question is how diminished receptor potentials at high frequencies can cause the motor to generate enough mechanical force to provide selective frequency amplification in the cochlea. No one has provided a definitive explanation for the speedup of the OHC membrane time constant.

In this thesis, I investigate the system dynamics of outer hair cells along with their surrounding mechanical structures. Inspired by the use of feedback in engineered

mechanical systems to speed up slow motors and to provide other favorable characteristics, I demonstrate that negative feedback on the reticular lamina by the outer hair cell mechanism can result in a speedup of the outer hair cell membrane time constant and that a near pole-zero cancellation reduces the effect that the time constant has on the transfer function from input force to output basilar membrane displacement. Thus, via negative feedback, OHCs and consequently the cochlear amplifier can achieve amplification at high frequencies despite the seemingly prohibitively slow membrane time constant.

The model that is used in the thesis consists of two spring-mass-damping resonators, representing the basilar membrane and reticular lamina, coupled together via the outer hair cell, represented as a spring and an active force. The electrical analog of this system, adopting the convention that currents are forces and voltages are velocities, contains two LRC tanks interconnected with a single inductor and a dependent current source between the reticular lamina and basilar membrane node. This representation is shown in Figure 1-1. The dependent current source, neglecting the effect of the piezoelectric properties of OHCs, is set by the reticular lamina displacement and has an associated gain and low-pass time constant due to the membrane. The parameters used in this model as described in Section 4 indicate that resonance of the reticular lamina comes first. In that regime, the impedance of the reticular lamina is resistive while the basilar membrane impedance is inductive. The feedback force, I_{fb}, is operating far beyond its cut-off frequency and thus has a $1/s^2$ dependence (1/s from velocity to displacement, 1/s from displacement to force). The resulting combined impedance of the outer hair cell and reticular lamina has a resistive component and an inductive component in addition to

an effective capacitive component created by the OHC force. The effective capacitor resonates with the inductors to produce a sharp peak followed by a sharp dip in the basilar membrane displacement response to an input force. The frequency and Q of the peak and dip increase with larger OHC gain because the effective capacitance is reduced by a greater current (greater force feedback). As a result, the OHC force can be effective at making the basilar membrane response more selective and sensitive.

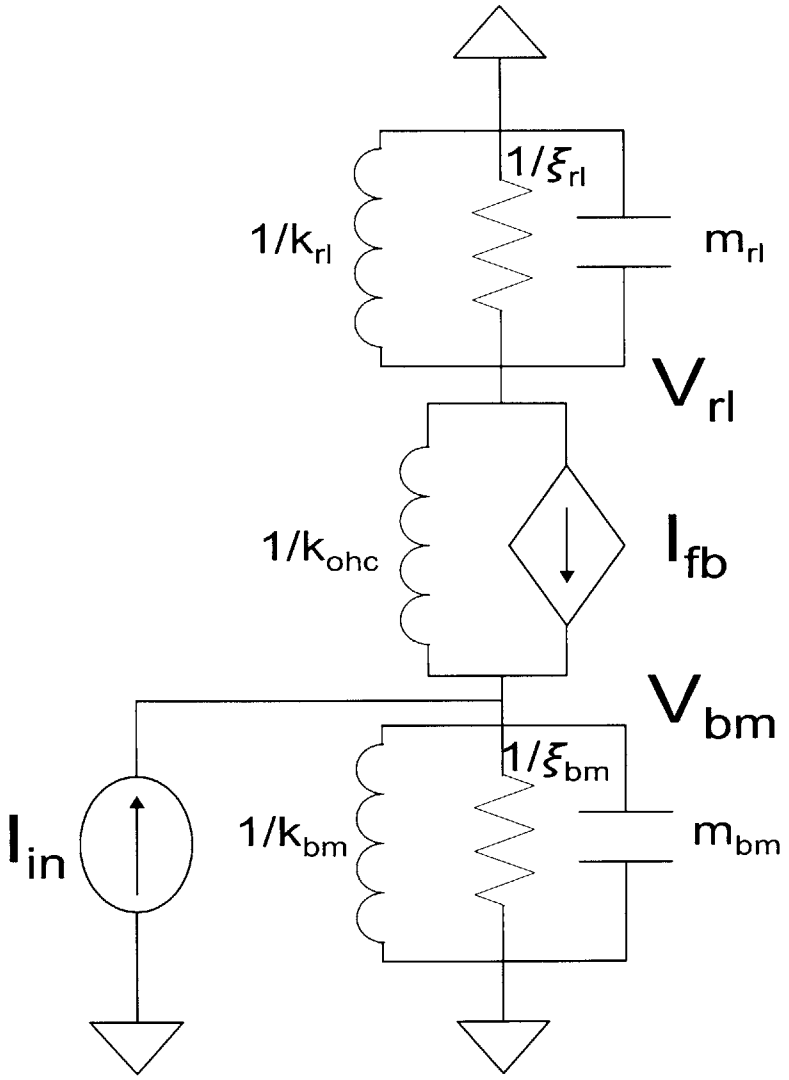

Figure 1-1. Electrical analog of the two resonator model with currents representing forces and voltages representing velocities. Same as Figure 4-29.

In Section 2, I describe how feedback is used in canonical motor systems to accelerate slow motor systems and to generate other favorable characteristics such as

stability and low error. Then, I introduce outer hair cell electromotility and describe previous work on this topic in Section 3. The local outer hair cell model is developed in detail in Section 4. Issues pertinent to combining multiple sections of the local outer hair cell model to form a traveling wave model of the cochlea are discussed in Section 5. Experimental data from the literature is presented in Section 6 and compared with the theoretical model. Future work is described in Section 7 while eight key insights about the operation of the local outer hair cell model and the putative biological cochlear amplifier are presented in Section 8. The main conclusions of the thesis are summarized in Section 9. References are included in Section 10.

2 Feedback in Motor Systems

The performance of mechanical systems is often limited by the speed of motors used to produce motion. In most cases, the electronics that control the mechanics are much quicker since they do not involve physical moving parts. In engineered systems, feedback is often used to minimize the effect of slow motors and to provide other benefits, including noise rejection and insensitivity to poorly-controlled parameters.

2.1 Introduction to Motors

Simple models can characterize the basics of the DC motor shown in Figure 2-1.

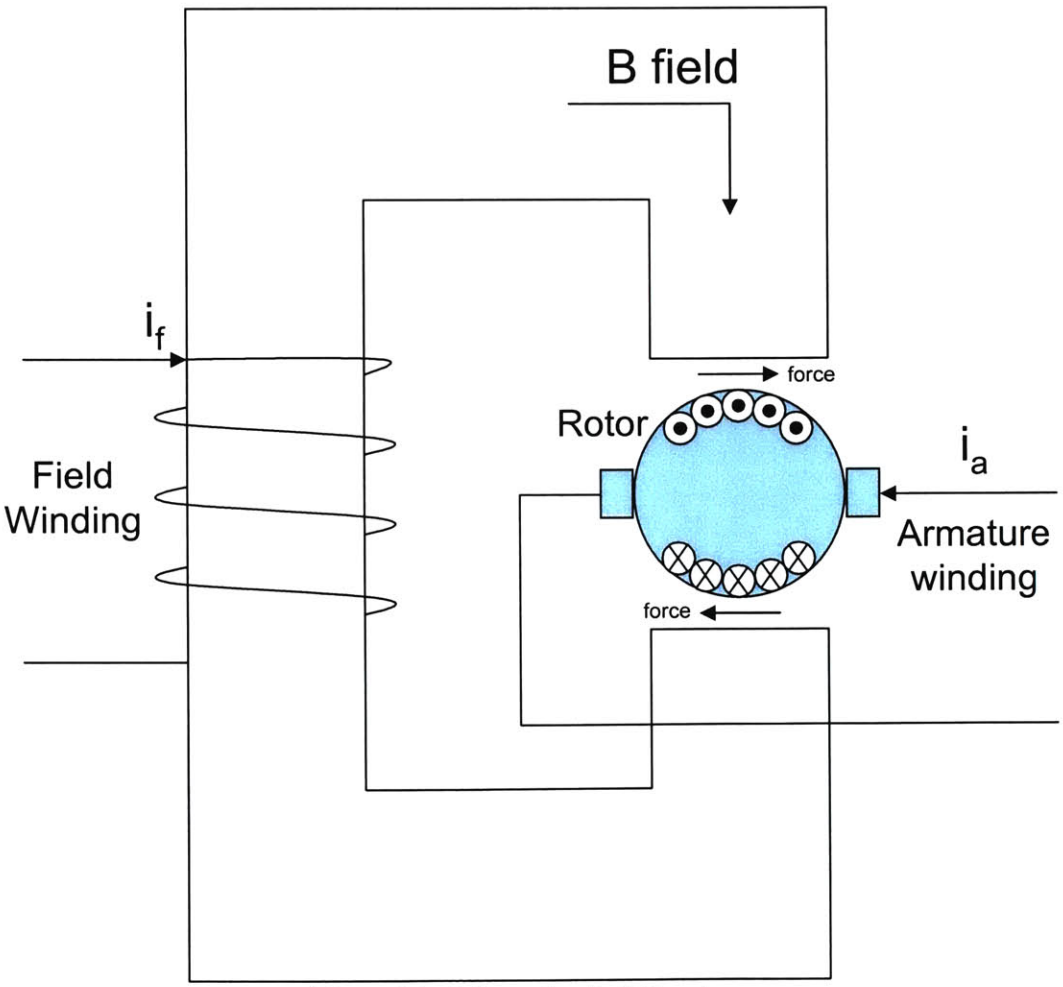

Figure 2-1. Schematic of a DC motor.
Adapted from Lundberg [5].

The magnetic field inside of the motor is generated by the field winding current, i_f. For permanent magnet motors, the B field is constant, which can be modeled by a constant current source attached to the field winding. The B field exerts a clockwise force on the rotor and thus causes mechanical work to be done. The torque on the rotor for a permanent magnet motor, assuming all vector components are perpendicular to each other, is given by Equation 2-1, where k_t is the torque constant.

$$T = k_t i_a$$

Equation 2-1. Torque on the rotor for a permanent magnet motor. k_t is known as the torque constant.

If the armature winding is driven by a voltage source and we ignore the effect of damping on the motor or the armature inductance, which is usually negligible compared to the mechanical components in the system, the transfer function from the armature voltage, V_a, to the motor angle, Θ, is described by Equation 2-2. k_m is the velocity constant, which in a permanent magnet motor is k_t^{-1}. τ_m is the dominant motor electromechanical time constant in the system and is equal to $J \cdot R_a / k_t^2$ in a permanent magnet motor. J is the moment of inertia of the rotor while R_a is the resistance of the armature winding.

$$\frac{\Theta}{V_a}(s) = \frac{k_m}{s(\tau_m s + 1)}$$

Equation 2-2. Transfer function from armature voltage, V_a, to motor angle, Θ. k_m is the velocity constant and is equal to k_t^{-1} while τ_m is the motor electromechanical time constant, which is given by $J \cdot R_a / k_t^2$. J is the moment of inertia and R_a is the armature winding resistance.

DC motors can also be controlled by current sources at the armature winding or by changing the current or voltage at the field winding. Ignoring damping on the motor, the transfer function from armature current, i_a, to the motor angle is given in Equation 2-3. Note that because the system is driven with a current instead of a voltage at the armature, there is no low-pass characteristic in the transfer function.

$$\frac{\Theta}{I_a}(s) = \frac{k_t}{Js^2}$$

Equation 2-3. Transfer function from armature current, I_a, to motor angle, Θ. J is the moment of inertia.

2.2 Feedback Techniques used in Motor Systems

Different feedback techniques are available to compensate motor systems. In this section, methods for controlling the velocity and position of motors are described.

2.2.1 Velocity Control

To control the angular velocity of a flywheel connected to a DC motor, a tachometer is used to sense the velocity and feed it back to the input. The feedback diagram for a velocity control loop using a tachometer with tachometer coefficient, K_{tach}, is shown in Figure 2-2. Note that the pole at the origin in Equation 2-2 is not present in the motor transfer function here because velocity, not position, is being fed back.

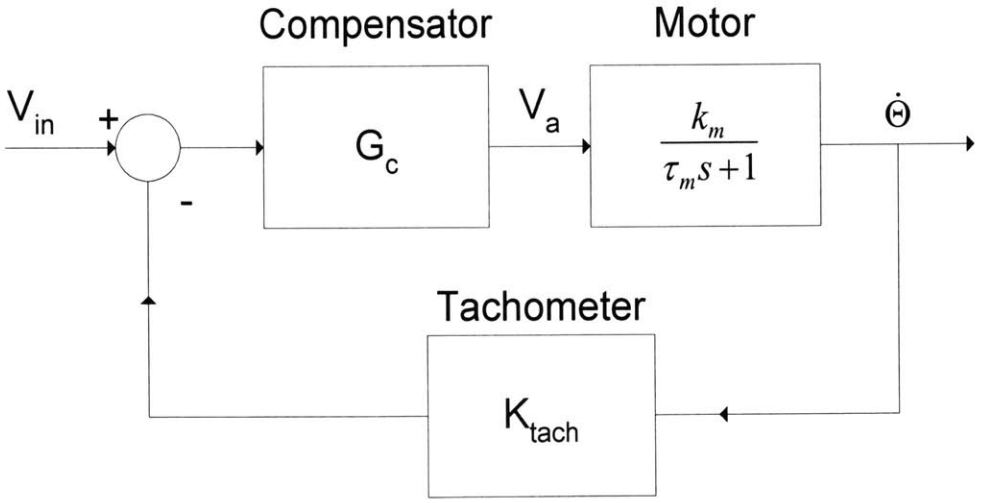

Figure 2-2. Velocity control feedback loop. G_c is the compensator and K_{tach} is the tachometer coefficient.

2.2.1.1 Proportional Compensator

Velocity control can be achieved by using a proportional compensator for G_c in Figure 2-2. A proportional compensator means that G_c is simply given by a constant gain.

The benefit of this form of feedback is that the time constant of the motor, τ_m, is sped up. This effect can be seen in the root locus plot shown in Figure 2-3. However, proportional compensation for velocity control has the drawback that the loop gain at DC is finite and so the steady state error of the system when driven with a unit step is non-zero.

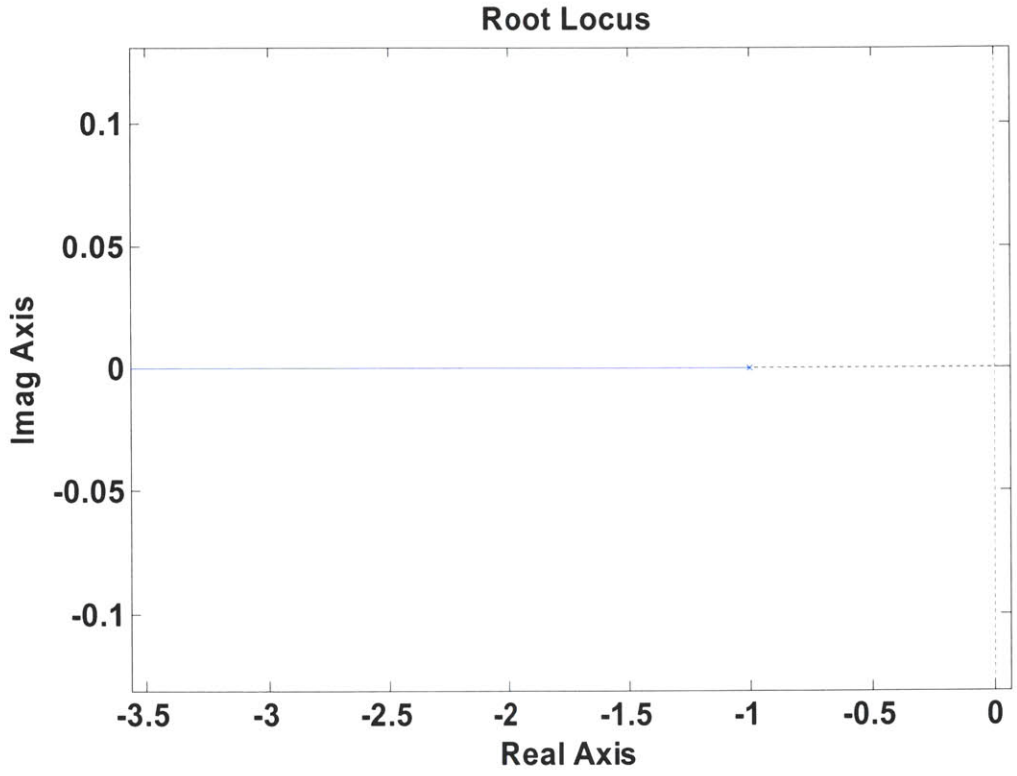

Figure 2-3. Root locus plot of velocity control with a proportional compensator. The time constant of the system is sped up as the pole moves deeper into the left half plane.

2.2.1.2 Proportional-Integrator Compensator

In order to reduce steady state errors and improve the DC gain, proportional plus integral (PI) compensation is also used in velocity control. For systems with a PI compensator,

$$G_c = G\frac{\tau s + 1}{\tau s}$$

Equation 2-4. Proportional plus integral compensator.

As evident from Equation 2-4, the DC loop gain approaches infinity because of the pole at the origin. This results in zero steady state error in response to a step input and thus better tracking. Furthermore, by making the zero of the proportional plus integral compensator be located at a higher frequency than the motor pole, speedup can still be achieved. However, the presence of the zero limits the amount of speedup of the motor time constant since, as seen in Figure 2-4, one of the poles will be attracted to the compensator zero and will remain there in the closed-loop transfer function. Because the compensator is usually implemented with electronics, the compensator zero can often be set to a high enough frequency so that this limitation is not a problem.

Complex closed-loop poles can be obtained by using this compensator but not by proportional compensation. This means that the time response of a PI compensated velocity control system may exhibit ringing, an effect that is often undesirable in mechanical systems.

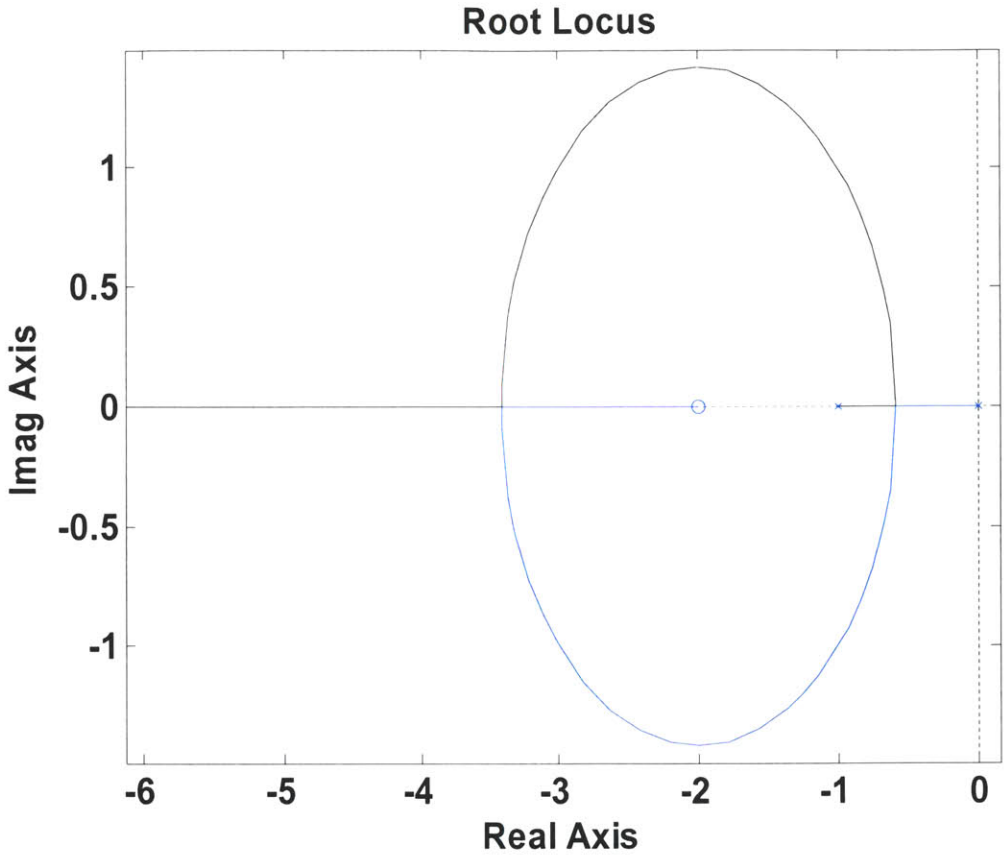

Figure 2-4. Root locus plot of velocity control with a proportional plus integral compensator. The two poles move deeper into the left hand plane, speeding up the system. However, the compensator zero limits the amount of speedup that is possible.

2.2.2 Position Control

In addition to being able to control the velocity of motors, engineered systems often require precise position control. Position control can be achieved by sensing the position of the output flywheel via a potentiometer or other sensors and feeding this information back into the input, as shown in Figure 2-5. The pole at the origin in the loop gain of position control as a result of Equation 2-2 requires different compensators from velocity control to achieve desired system characteristics.

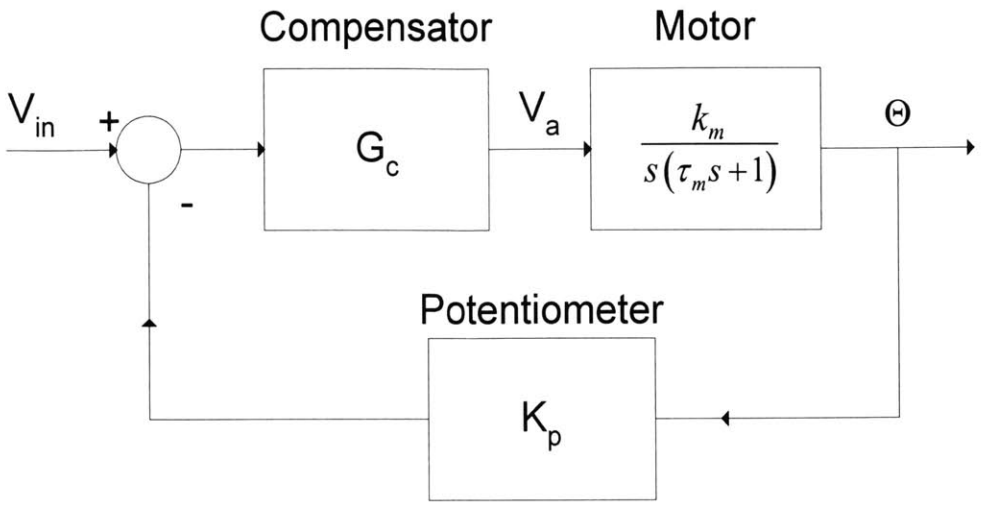

Figure 2-5. Position control feedback loop.
G_c is the compensator and K_p is the potentiometer coefficient.

2.2.2.1 Proportional Compensator

As with proportional compensation in velocity control, proportional compensation for position control is when G_c is simply a constant. In this case, the root locus plot looks like Figure 2-6. As the gain is increased, the closed-loop poles, which start off at $-1/\tau_m$ and the origin, approach each other and eventually split off of the real axis and travel vertically. Thus, complex poles are obtained in the closed-loop system for high gains. While this may result in greater speeds with high enough gain, it may generate undesirable step responses that ring and require a long time to settle to a final value. Because of the pole at the origin, the DC loop gain approaches infinity and the steady state error in response to a unit step input goes to zero.

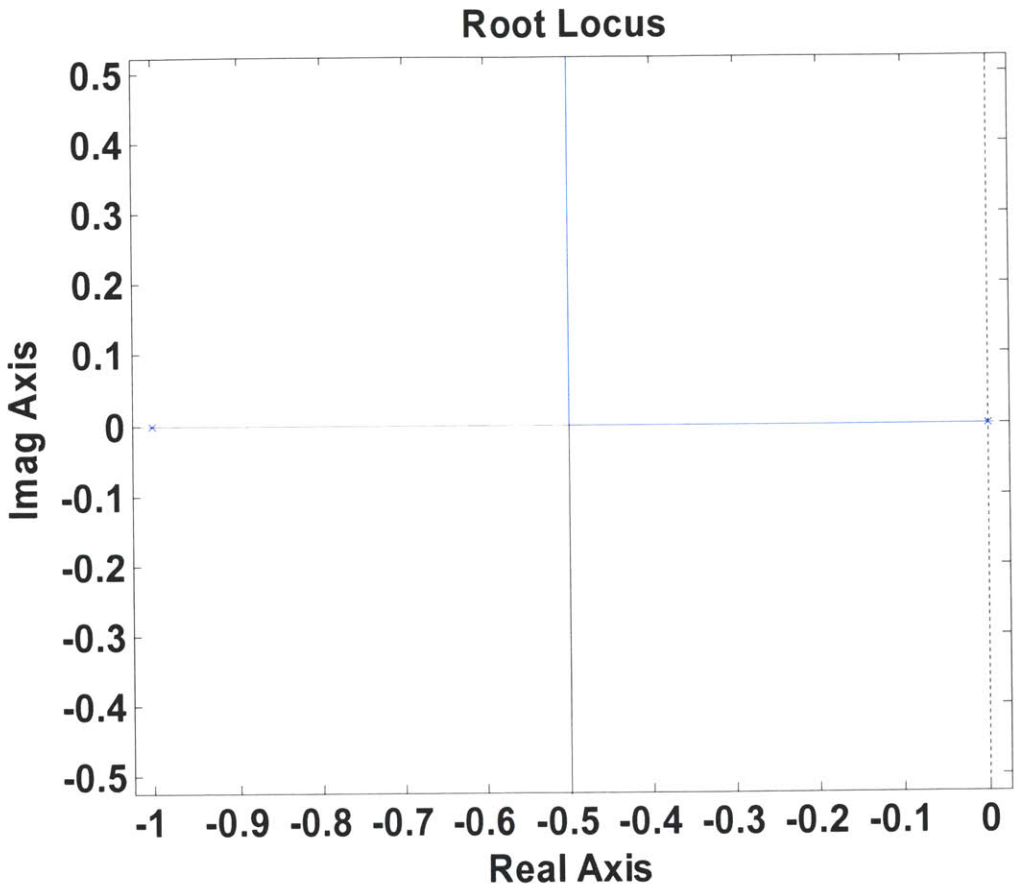

Figure 2-6. Root locus plot of position control with a proportional compensator. The two closed-loop poles become complex with high gain.

2.2.2.2 Proportional-Derivative Compensator

Instead of using a proportional compensator, position control can also be achieved with proportional plus derivative (PD) compensation. In such a system, G_c is ideally given by:

$$G_c = G(\tau s + 1)$$

Equation 2-5. Proportional plus derivative compensator.

However, since physically realizable systems generally do not have more zeros than poles, G_c is usually implemented as a lead compensator with a high-frequency pole. Here, that pole is ignored for simplicity since it is generally too fast to be of interest to the first order. The zero of the proportional plus derivative compensator can be placed at

a frequency higher than the poles of the motor. As seen in Figure 2-7, the two poles move deeper into the left half plane and are thus sped up. Complex poles can be obtained with intermediate gain levels as well. However, the advantage of a proportional plus derivative compensator over a proportional compensator is that the complex closed-loop poles can be eliminated with high gains, thus providing a step response with less ringing and faster settling time.

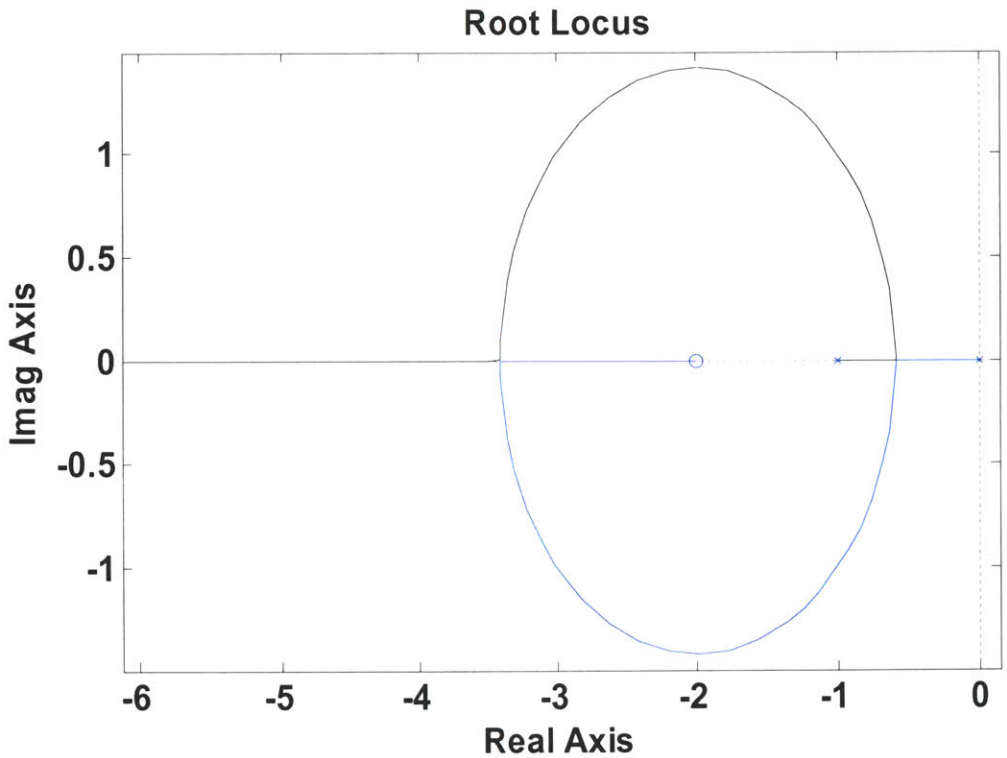

Figure 2-7. Root locus plot of position control with a proportional plus derivative compensator. The two poles move deeper into the left hand plane, speeding up the system. However, the compensator zero limits the amount of speedup that is possible.

Like the proportional compensator for position control, the pole at the origin resulting from the motor transfer function produces an infinite DC loop gain. Since this pole acts as a single integrator in the forward path, the resulting steady state error to a step input is zero.

2.2.3 Minor Loop Feedback

Minor loop feedback was a concept initially applied to servomechanisms in order to minimize the sensitivity of mechanical systems to changes in the moment of inertia of the flywheel that the motor is driving [5]. Minor loop feedback involves nested feedback loops, can shape the resulting open-loop behavior of the forward path, and is useful in reducing the effect of poorly-controlled parameters on system stability and performance. Operational amplifiers use minor loop feedback heavily to stabilize their characteristics.

For example, suppose that position control is implemented using a current amplifier to drive the armature winding. Assuming that the amplifier has a time constant, τ_a, associated with it, a feedback position control system without minor loop feedback is depicted in Figure 2-8. The electromechanical time constant of the motor is not relevant in the transfer function because the motor is being driven with a current instead of a voltage and the torque of a DC motor is directly related to the armature current.

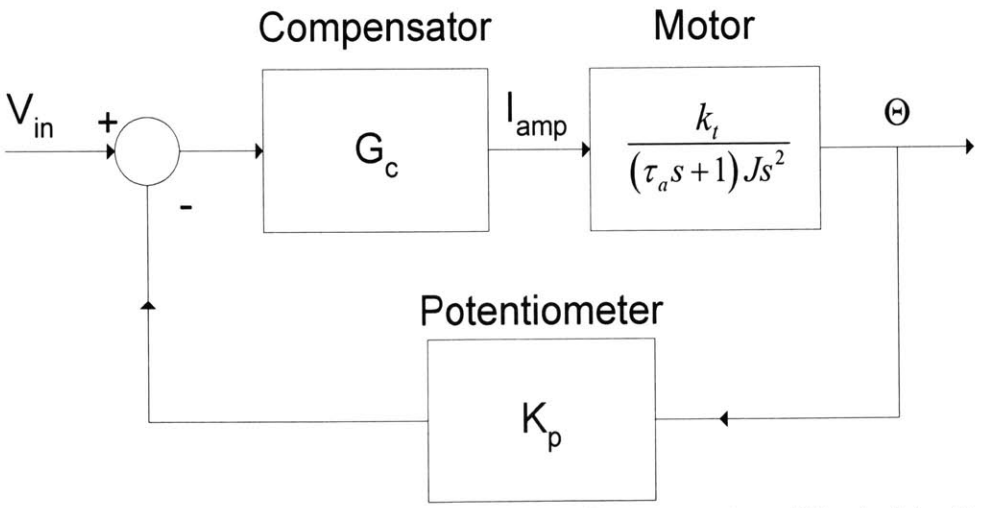

Figure 2-8. Block diagram for a standard feedback loop using a current amplifier to drive the motor.

Because of the double poles at the origin, the closed-loop transfer function is unstable. The system can be compensated with a lead network for G_c, as is done in [5],

where G_c is composed of a low frequency zero and a high frequency pole. Thus, the loop transmission can be written as shown in Equation 2-6, where $\alpha > 1$.

$$L(s) = K\left(\frac{\alpha\tau_L s + 1}{\tau_L s + 1}\right)\left(\frac{k_t}{(\tau_a s + 1)Js^2}\right)$$

Equation 2-6. Loop transmission of Figure 2-8 with a lead compensator.

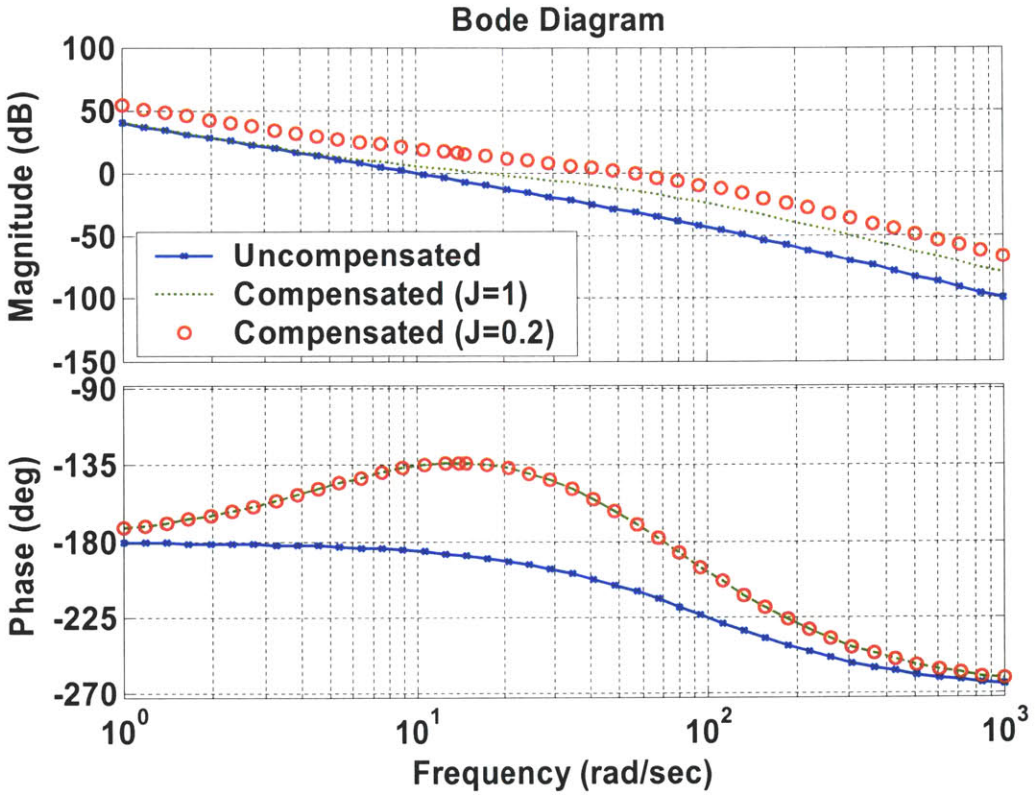

Figure 2-9. Lead compensated (J=1 and J=0.2) and uncompensated Bode plots of the loop transmission in Equation 2-6.
The uncompensated system is unstable while the J=1 compensated system crosses over with about 45° of phase margin. The J=0.2 compensated system crosses over with only about 12° phase margin, demonstrating the sensitivity of this compensation method to J.

As seen in Figure 2-9, lead compensation optimized for J=1 can cause the loop transmission to cross over with 45° phase margin and thus stabilize the closed-loop system. Furthermore, lead compensation can generate a speedup of the system as the crossover frequency of the loop transmission is increased. However, lead compensation of the system in Figure 2-8 is very sensitive to the moment of inertia of the flywheel, J. For example, if the parameter J is reduced by a factor of 5 to J=0.2, the phase margin of

the system in Figure 2-9 drops sharply to only 11°, resulting in a closed-loop system with a very bad time response. In situations such as this where parameters must operate over a wide range, minor loop compensation can be helpful.

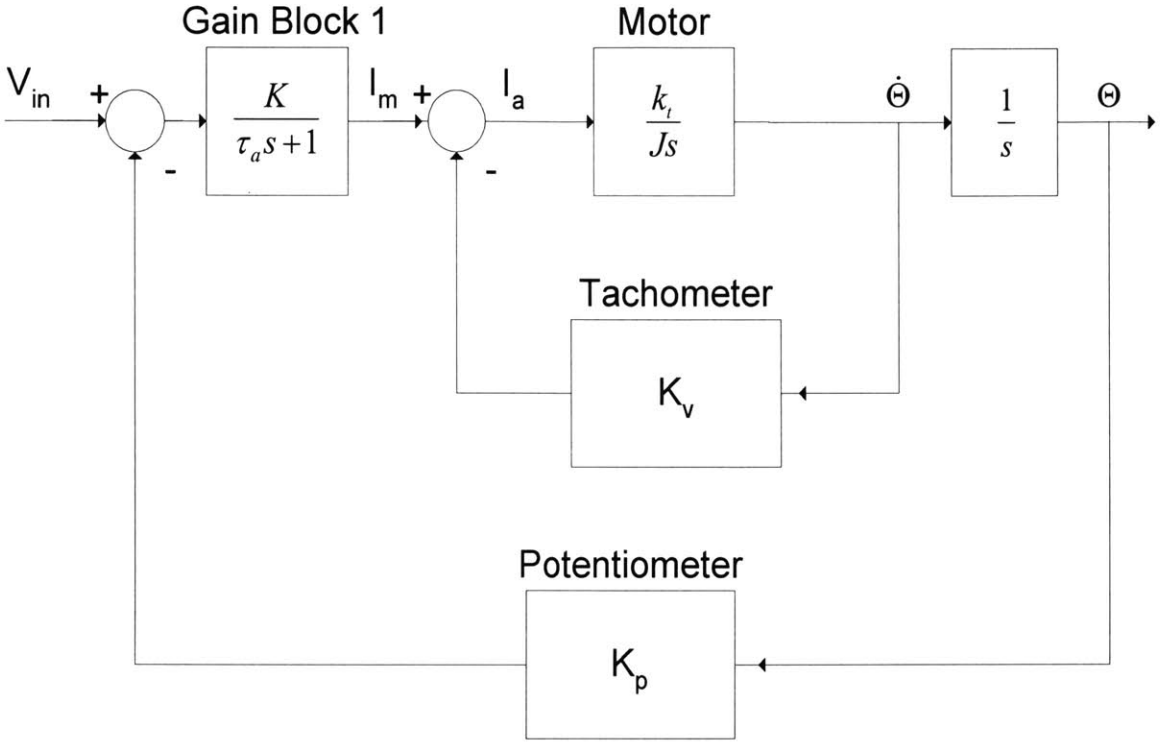

Figure 2-10. Block diagram for minor loop feedback for position control. Both a tachometer and potentiometer are used. τ_a is the time constant of the current amplifier while K is the gain parameter. K_v represents tachometer feedback and gain from angular velocity to current. Adapted from Lundberg [5].

Minor loop feedback for position control is depicted in Figure 2-10. The velocity of the flywheel is sensed by a tachometer and fed back in an inner loop around the motor, which is driven by a current amplifier with time constant τ_a. The outer loop is composed of sensing the position of the motor and feeding it back to the input. The effect of the inner loop is to move one of the original poles at the origin into the left half plane depending on the gain of the tachometer, K_v. The closed-loop transfer function for the inner loop is given in Equation 2-7.

$$\frac{\dot{\Theta}}{I_m}(s) = \frac{k_t}{Js + K_v k_t}$$

Equation 2-7. Closed-loop transfer function for the inner loop in Figure 2-10.

Thus, instead of having an immediately unstable uncompensated root locus plot like that in Figure 2-11 with two poles at the origin and one on the real axis in the left hand plane, only one pole is at the origin while the other two are on the real axis in the left hand plane, as shown in Figure 2-12. This allows the designer the ability to stabilize the system without using lead or lag compensation.

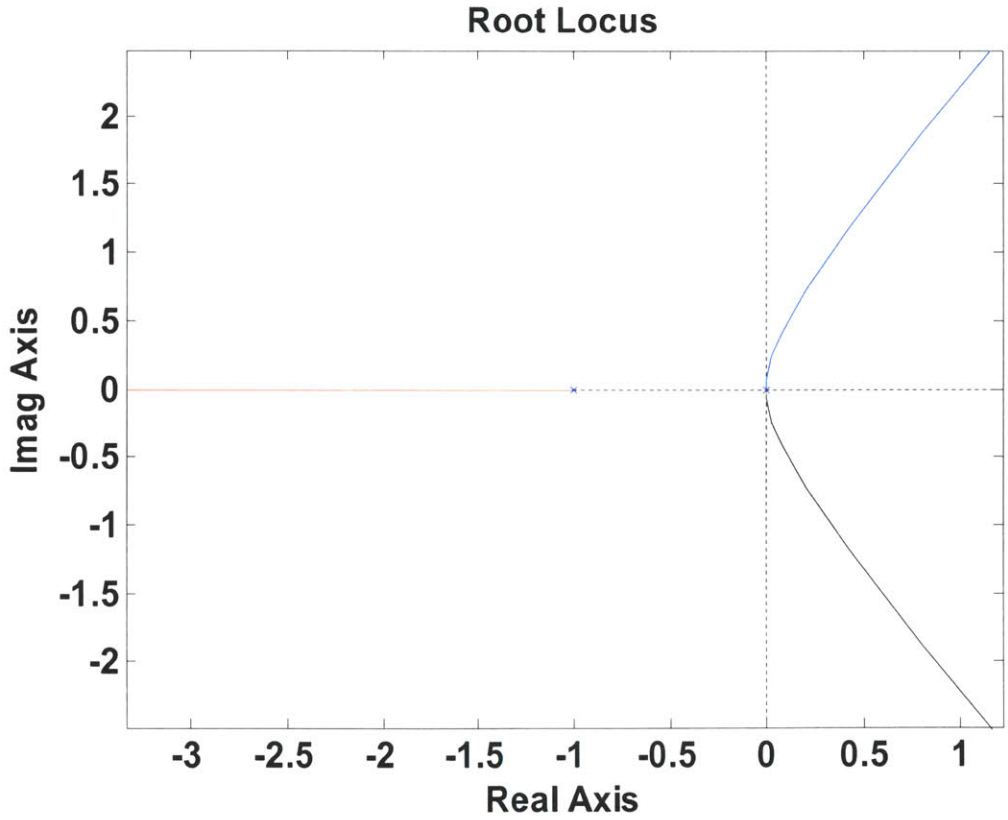

Figure 2-11. Root locus of the uncompensated motor system is immediately unstable because of the two poles at the origin.

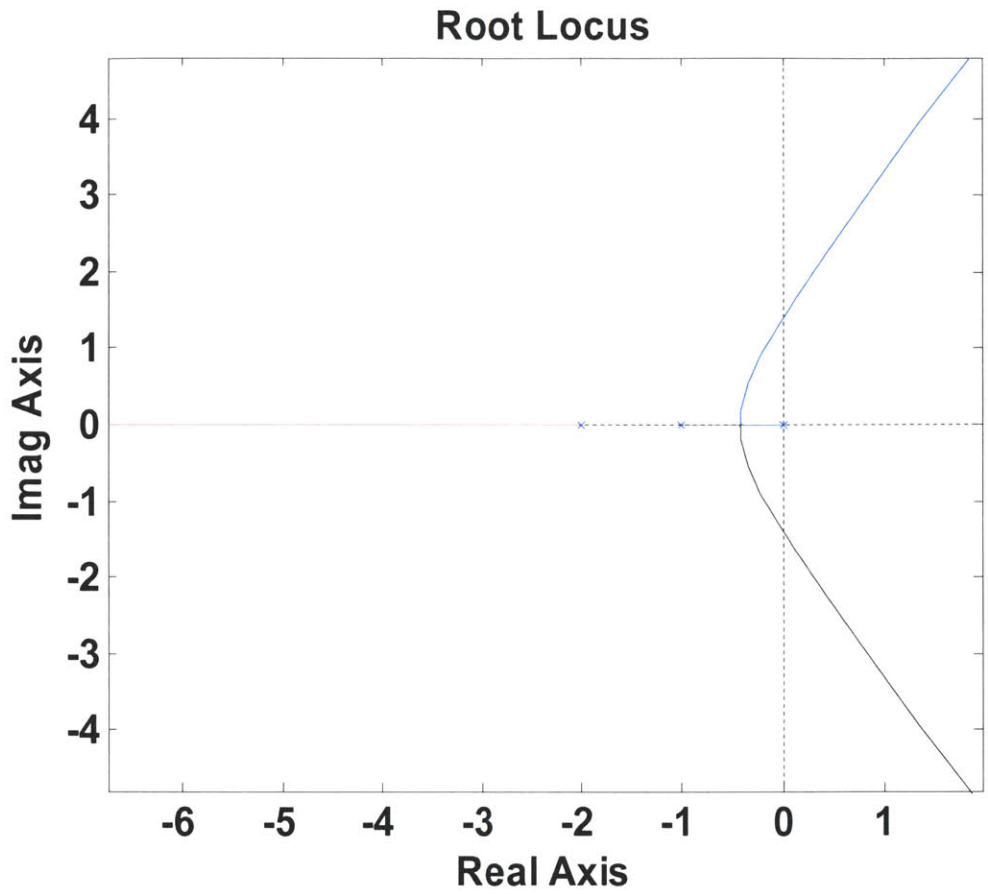

Figure 2-12. Root locus of motor system with minor loop compensation. Note that one of the poles originally at the origin has moved to the left and thus the system can be stabilized.

Minor loop compensation can thus stabilize systems and also generate speedup of slow time constants by providing an additional degree of freedom that can be manipulated to drive poles into faster regimes. For example, one of the poles at the origin in Figure 2-12 was forced further into the left half plane. If the plant had only a single pole, the effect of speedup would be even more obvious, for the minor loop would push the pole into the left half plane while the outer loop pushed the pole out even further.

As stated above, however, one of the primary advantages of minor loop feedback is to reduce sensitivity to varying parameters. This property is evident in Figure 2-13 as the moment of inertia is reduced from J=1 to J=0.2. Whereas in lead compensation, the

reduction of J resulted in a loss of phase margin, with minor loop compensation, reduction of J actually increases the phase margin and thus the stability of the system. As a result, designers can design for an upper bound on the varying parameter and be confident that decreases in that parameter will not cause instability. In addition, speedup of the system via minor loop feedback is evident from the increase in the crossover frequency of the loop transmission in Figure 2-13.

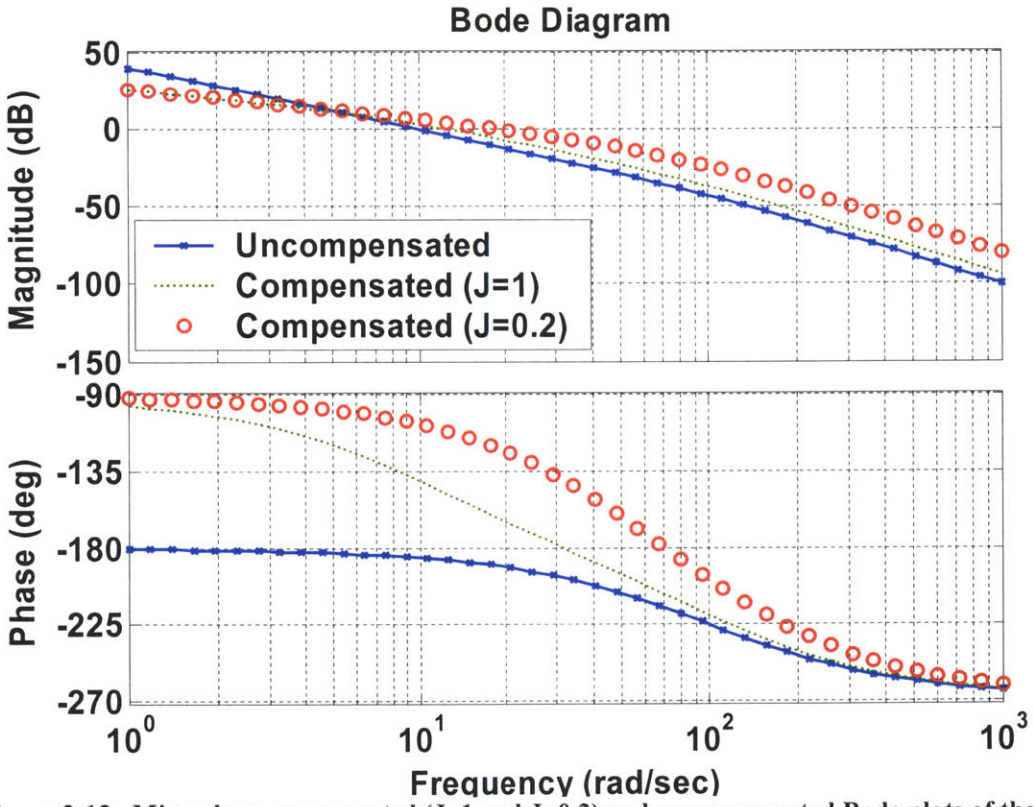

Figure 2-13. Minor loop compensated (J=1 and J=0.2) and uncompensated Bode plots of the loop transmission depicted in Figure 2-10.
Note that the reduction of J from 1 to 0.2 that led to decreased phase margin in the lead compensation without a minor loop actually increases the phase margin here.

Instead of using a constant gain in the minor loop feedback path, K_v, or in the major loop forward path, K, different compensator forms can be used. For example, using the frequency dependent network, H_{min}, expressed in Equation 2-8 in the minor loop feedback path in place of K_v is known as acceleration feedback and can produce

zero steady-state error in response to a step input [5]. Minor loop provides an additional mode of flexibility in shaping the closed-loop system and is thus a useful technique for designing systems and speeding up motors.

$$H_{\min}(s) = K_{tach}\frac{\tau s}{\tau s + 1}$$

Equation 2-8. Acceleration feedback network to be used in the minor loop feedback path.

2.3 Conclusions

In this section, various feedback methods were presented in the context of motor systems, either for velocity or position control. Negative feedback with various compensators was capable of producing stable systems and speeding up slow time constants. Minor loop feedback was described as a method for obtaining an additional degree of design freedom and provided increased insensitivity to varying parameters. Since motors and systems with mechanical parts often have slow dynamics, designers use electronic feedback to increase gain, reduce steady state errors, and generate faster and improved responses. These concepts of feedback are also prevalent in biological systems such as the cochlea and outer hair cells in striking analogy with engineered motor systems. As a result, I will demonstrate in later sections that adopting a feedback view of the cochlear amplifier can explain how outer hair cells amplify incoming sounds at frequencies far beyond their intrinsic membrane cutoff frequency and how force feedback can generate increases in sensitivity and selectivity when the cochlear amplifier is operating.

3 Introduction to Outer Hair Cell Electromotility

3.1 Overview of the Cochlea

The mammalian cochlea is located in the inner ear; in humans, it is about 35 mm in length but exists in coiled form [1]. Filled with cochlear fluid, the cochlea is partitioned into three compartments, the scala vestibule (vestibuli), the scala media, and the scala tympani, as shown in Figure 3-1 [6].

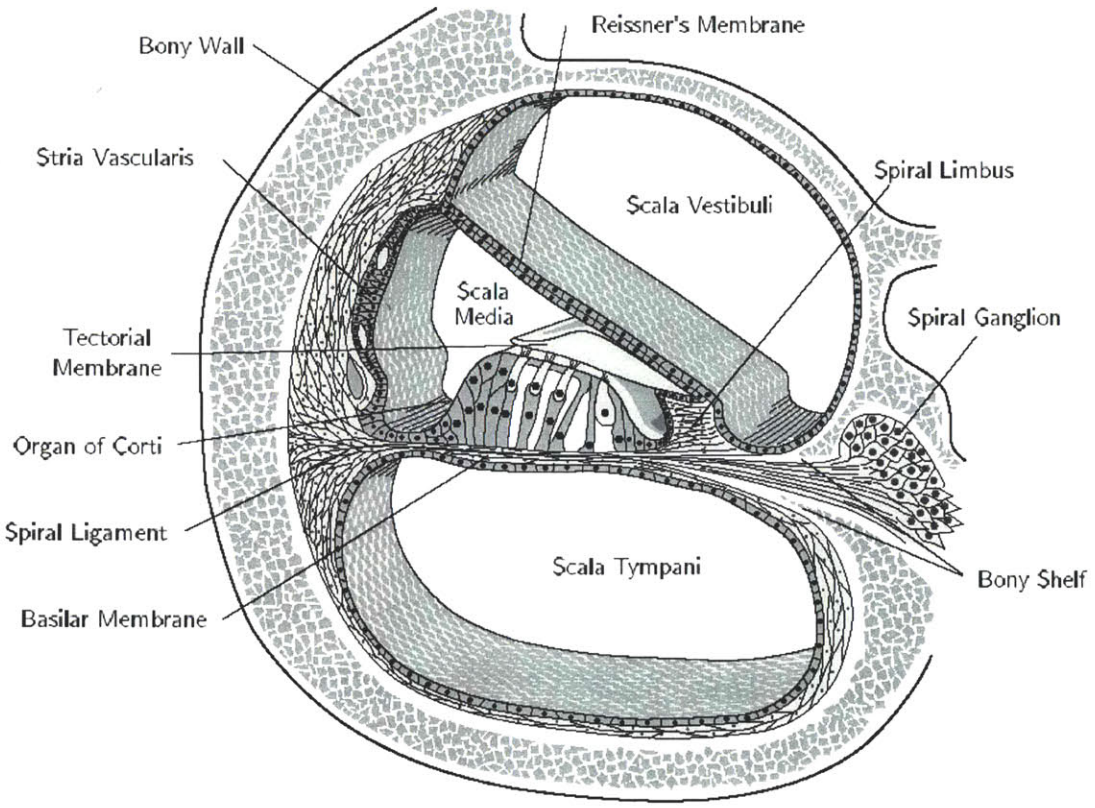

Figure 3-1. Cross-section of the cochlea showing the three compartments. Reproduced from Watts [7].

When sound energy that has been transduced into mechanical energy vibrates the stapes, the oval window displaces fluid in the cochlea and generates a traveling wave of fluid pressure down the length of the cochlea [1]. This fluid pressure causes a wave of displacement along the basilar membrane, which composes a boundary of the cochlear

partition [6]. Since the basilar membrane varies from being stiff at the basal end, the end near the stapes, to being flexible at the apical end, the displacement of the basilar membrane increases as the wave moves from the base to the apex, peaking at a location that has a characteristic frequency which matches the frequency of the incoming wave [1]. Thus, the cochlea performs a frequency-to-place transformation on incoming sounds.

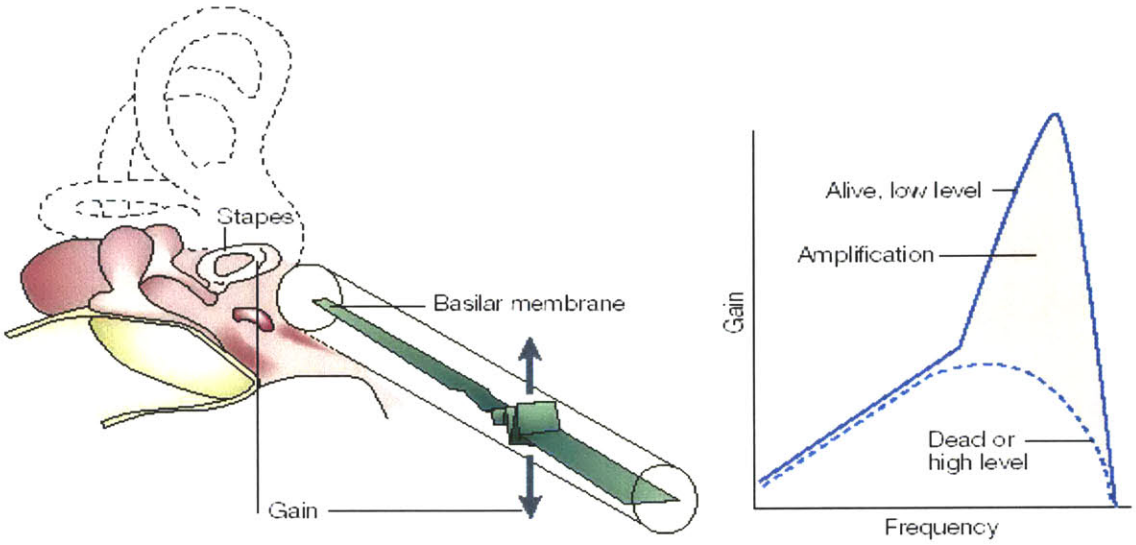

Figure 3-2. The motion of the stapes generates a traveling wave down the basilar membrane. The gain between BM movement and stapes movement requires active amplification to give the selectivity and sensitivity observed in live cochleas. Reproduced from Dallos and Fakler [2].

Measurements made by von Békésy in the 1940s on dead mammalian cochleas demonstrated relatively highly damped and poorly damped cochlear vibrations [6]. In comparison, modern measurements performed on living cochleas exhibit much sharper frequency localization and much less damping for low sound levels, as demonstrated pictorially in Figure 3-2 [6]. This is necessary for the auditory pathway to be able to resolve and interpret information encoded in varying sound frequencies. A great deal of experimental evidence suggests that a local mechanical feedback mechanism, termed the "cochlear amplifier," is responsible for the sensitivity and the frequency selectivity observed in living cochleas [3].

3.2 Cochlear Amplifier

The frequency selectivity of living cochleas at low sound levels is diminished when larger sound levels are applied or when the cochlea is damaged [6]. To obtain sharp responses at low sound levels, negative damping must be introduced into the system to reduce the effect of friction on the movement of the basilar membrane. This, combined with the observation of spontaneous otoacoustic emissions from the ear, led to the hypothesis that outer hair cells located in the cochlea may provide the mechanical energy necessary to produce the effects of the cochlear amplifier [6]. The cochlear amplifier has been measured to produce gains of up to 1000 in living cochleas for frequencies around the characteristic frequency (CF) of a given location compared to no gain in dead cochleas [1]. The CF is the frequency at a certain location where the cochlear partition response is most significant. It is believed that an active feedback mechanism involving the outer hair cells is responsible for the cochlear amplifier [6]. As often seen in analog circuit design and other engineered systems, feedback can sharpen the frequency response and provide amplification for a system.

3.3 Overview of Hair Cells

Two types of hair cells exist in the mammalian cochlea: inner and outer hair cells. The former is responsible for transducing sound energy into neural pulses that are sent to the brain [6]. The latter is believed to provide the mechanical energy necessary for the cochlear amplifier to function. Both these cells are located in the organ of Corti, which sits atop the basilar membrane, with the apical face of the cells embedded in the reticular lamina [6]. Hair cells are named for the row of microvilli or stereocilia that protrude from the apical end. The microvilli are ordered from tallest to shortest and are connected

together at the tips via tip links [6]. Outer hair cells have their tallest stereocilia embedded in the tectorial membrane while inner hair cells have free-standing hair bundles [6]. The anatomy of the organ of Corti and the placement of the hair cells are shown in Figure 3-3. The modiolus is to the right of the structure in Figure 3-3.

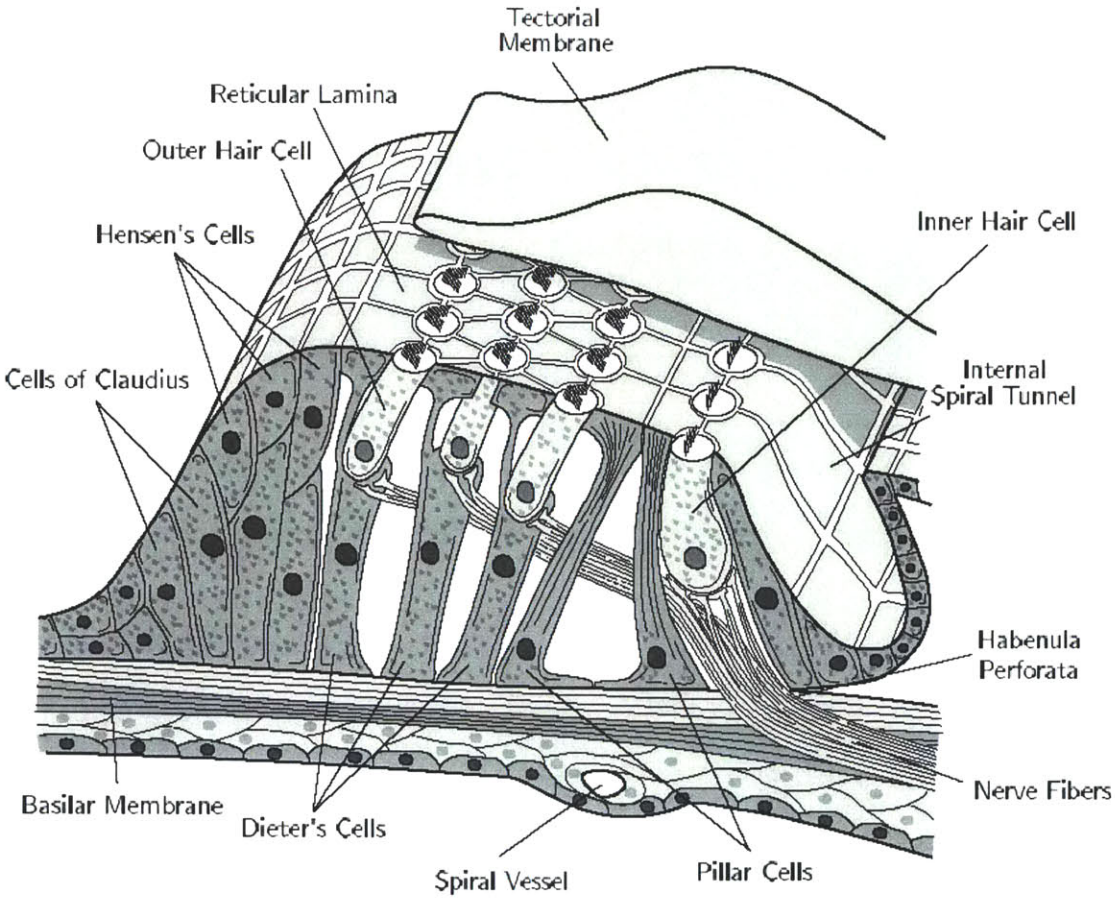

Figure 3-3. The organ of Corti and associated structures. Reproduced from Watts [7].

It is believed that tip links are essential for these hair cells to transduce mechanical motion of the fluid into electrical potentials. One theory suggests that tip links are connected to cation channels that are embedded in the stereocilia [6]. Upon excitatory displacement in the direction towards the tallest cilia, the tip links are pulled taut and the cation channels are opened, allowing K^+ ions to flow into the cell to

depolarize the membrane potential, as shown in Figure 3-4 [6]. Excitatory displacement is associated with rotation away from the modiolus. In the case of inhibitory displacement in the direction away from the tallest cilia, the tip links are limp and the cation channels are consequently closed [6]. As a result, the membrane potential hyperpolarizes.

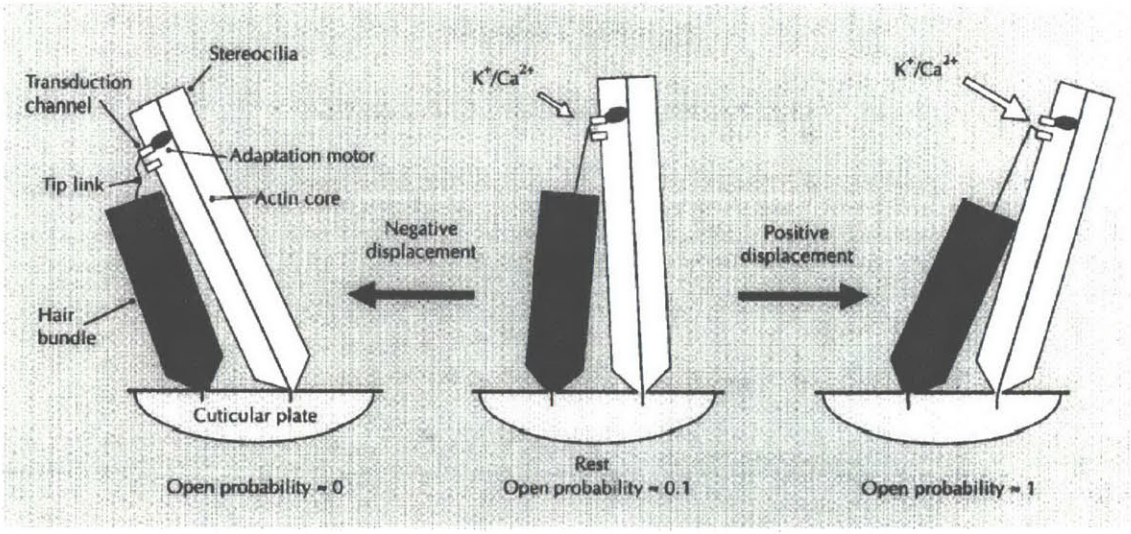

Figure 3-4. Proposed mechanism for the operation of transduction channels in hair cell stereocilia. Excitatory displacement towards the tall cilia causes tension in the tip link and opening of the ion channel, allowing K^+ ions to flow into the cell. Inhibitory displacement results in a decrease of the tension and thus a much smaller open probability of the ion channel. Reproduced from Gillespie [9].

Changes in the membrane potential are translated into neural pulses in inner hair cells while they trigger motion in outer hair cells [8]. Inner hair cells (IHCs) that sit on the basilar membrane depolarize in response to basilar membrane movement and other structures in the organ of Corti, stimulating the auditory nerve fibers connected to the IHCs and causing nerve impulses to be fired. Outer hair cells are also depolarized or hyperpolarized by movement of the basilar membrane, the reticular lamina, and the tectorial membrane (TM). This general process is illustrated in Figure 3-5. Movement of the TM-RL gap causes a shearing fluid force on the inner hair cell hair bundle while it causes the direct bending of stereocilia on the outer hair cells. In Figure 3-5, the

stereocilia are bent to the left away from the modiolus in an excitatory manner. Another mechanism for the depolarization of inner hair cells may be that the Hensen's stripe, which is a protrusion from the tectorial membrane, contacts or squeezes fluid through the inner hair cell hair bundle, causing it to move and modulate the stereocilia conductance.

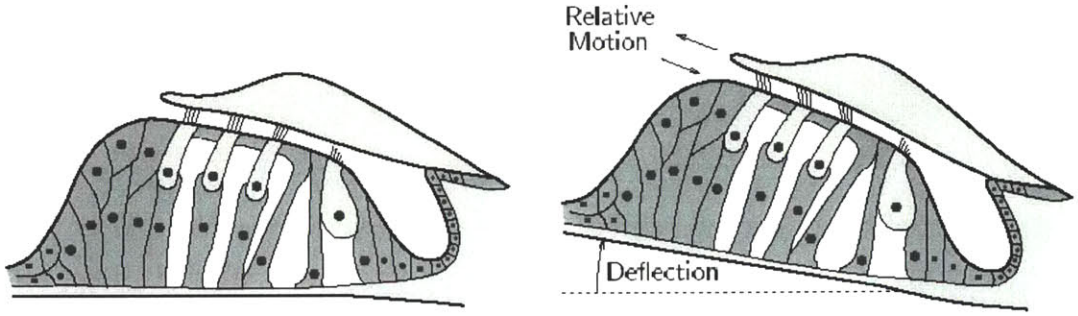

Figure 3-5. The relative motion between the reticular lamina and the tectorial membrane causes a bending of stereocilia of the outer hair cells. Fluid shearing in the TM-RL gap may cause the inner hair cell stereocilia to bend as well.
Reproduced from Watts [7].

If hair cells are subjected to static displacement of their stereocilia, adaptation occurs and the transfer curve from displacement to inwards K^+ current shifts to become recentered at the new operating point [6]. The presence of Ca^{2+} ions in the cell interior seems to be intimately connected with this process but a myosin adaptation mechanism is possible as well. Essentially, the process of adaptation serves to provide a form of automatic gain control for the auditory system.

3.4 Mechanical Properties of OHCs and Associated Structures

Outer hair cells respond to depolarization of the membrane potential by contracting while they elongate when hyperpolarized [1]. The sensitivity of this process versus the membrane potential has been fit as a Boltzmann curve with a maximum low-frequency gain of about 20 nm/mV [6]. OHC lengths can vary from 20 μm in the base to 90 μm at the apex in guinea pigs [6]. Bats and other mammals with higher hearing have been found to have shorter outer hair cells [10]. Since the tips of the tallest stereocilia of

the OHCs are embedded in the stiff tectorial membrane, when the basilar membrane moves upwards, the triangular pillar cell complex containing the OHCs pivots in a towards the modiolus [6]. The stereocilia are arranged so that this movement displaces them in the excitatory direction away from the modiolus, causing the membrane potential to depolarize and the OHC to contract [1]. This contraction pulls the basilar membrane further upwards and pulls the reticular lamina downwards. The mechanical energy from the OHCs counteracts the frictional forces the basilar membrane and reticular lamina encounter while moving and provides the active force generation responsible for the cochlear amplifier [6].

Experiments performed on both the reticular lamina and the basilar membrane suggest that the basilar membrane is 5-10 times stiffer than the reticular lamina [11]. This means that upon OHC contraction, the reticular lamina moves 5-10 times more than the basilar membrane.

A great deal of effort has gone into characterizing the mechanical properties of outer hair cells. Somatic axial stiffness of OHCs has been estimated to be 0.544 nN/μm, 1.6 nN/μm, 6.6 nN/μm, and 10 nN/μm by different research groups [1]. The stiffness of outer hair cells is dependent on the membrane potential; OHCs become less stiff with depolarization [11].

3.5 Electrical Properties of OHCs and Associated Structures

The endolymph fluid that fills scala media and encompasses the cilia and apical surface of outer hair cells contains a high concentration (150 mM in guinea pigs) of potassium ions and a low concentration (1 mM in guinea pigs) of sodium ions [6]. This extracellular fluid composition is intriguing since it seems to be closer to what is found in

the interior of most mammalian cells. The scala media sits at a potential of about +60 to +100 mV above that of the vascular system [6]. The perilymph fluid that contacts the basolateral surface of OHCs is composed of a high concentration of sodium ions and a low concentration of potassium ions and has an electrical potential that is approximately neutral compared to the vascular system [6]. The large positive voltage of the endolymph may act as a battery to power the electromotile response of outer hair cells.

The intracellular potential of outer hair cells is about -60 ± 10 mV [6]. Thus, a large potential gradient is established across the apical surface by the positive endolymph potential and the negative potential inside the cell. This means that when more ion channels in stereocilia are opened, more K^+ ions are able to depolarize the membrane receptor potential. These potassium ions leave the cell via selective potassium channels in the basolateral membrane [6].

The input-output curve of outer hair cells, where acoustic pressure is the input and receptor potential is the output, is S-shaped and saturates at higher levels of input [6]. The nonlinear membrane capacitance of outer hair cells exhibits a bell-shaped dependence on the membrane potential [1]. This capacitance is added to the linear membrane capacitance determined by the membrane surface area and dielectric constant itself. The specific capacitance, defined as the capacitance for a unit area of plasma membrane, has been characterized at about 2 $\mu F/cm^2$ [6]. Specific conductances have been measured to vary from 70 $pS/\mu m^2$ for short OHCs to less than 10 $pS/\mu m^2$ for long OHCs [6]. The capacitance and membrane conductance generate a first-order low-pass filter with a corner frequency that is higher for shorter cells and lower for longer ones [6]. Characterizations of the corner frequencies of this low-pass filter indicate an upper bound

of about 1 kHz [6]. This low-frequency cutoff may limit the receptor potential at high frequencies, making it questionable whether or not the receptor potential is adequate at high frequencies to drive the motor protein in outer hair cells.

3.6 Previous Work

The motor protein of outer hair cells, prestin, has been shown to directly convert voltage to force by sensing voltages via cytoplasmic anions [1]. The proposed model of prestin's behavior is shown in Figure 3-6. The default state of prestin is not extended, but when a Cl^- binds to the cytoplasmic side of the protein, it increases in length, causing a net lengthening of the outer hair cell.

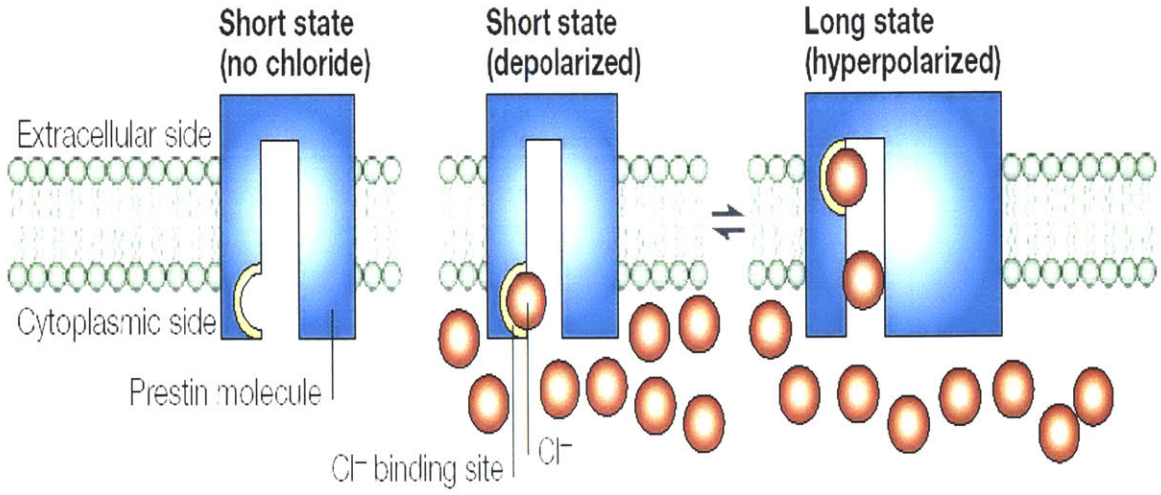

Figure 3-6. The proposed model for the operation of the OHC motor protein, prestin. Binding of Cl^- ions causes a conformational change in prestin, leading to a net extension in molecular length and thus outer hair cell length. Reproduced from Dallos and Fakler [2].

Frank et al. [4] has demonstrated that the response of the motor protein itself is second-order with a -3dB bandwidth of at least 79 kHz. The electromotile response up to 100 kHz was characteristic of an overdamped second-order system with a Q of 0.42 [4]. This suggests that the mechanical limitations of the electromotile response are both damping and inertia, at least *in vitro* [4]. At frequencies of up to 50 kHz, OHCs have

been measured to produce up to 53 pN/mV of force [4]. Thus, it appears that the motor protein itself is able to operate in the upper limits of hearing; the remaining question is how the severely attenuated receptor potential can drive the motor up at such frequencies.

Mammano and Ashmore [11] estimate the magnitude of the average sensitivity of outer hair cells isolated from guinea pigs to external current to be about 24.8 V/A. They found this by injecting external current with a stimulus pipette. Based on this value, a 100 μA input current would give rise to a depolarization of the membrane potential by about 2.5 mV and a contraction of isolated hair cells by about 50 nm, at least at low frequencies [11]. *In* vivo, such a stimulus resulted in a 20 nm differential displacement between the reticular lamina and the basilar membrane, where the absolute basilar membrane displacement was about 2 nm [11].

There have been several theories that attempt to explain how outer hair cells may generate enough force at high frequencies to provide mechanical feedback to overcome the damping experienced by the cochlea.

3.6.1 Extracellular Potential Gradients

Dallos and Evans postulated that extracellular potential gradients are responsible for the electromotile response at high frequencies [3]. In their model, extracellular potential gradients can be modeled by the injection of current into the extracellular fluid by OHCs that are basal to the OHCs being analyzed [3]. To analyze this system, consider Figure 3-7, where OHC1 is basal to OHC2. R_a models the apical resistance, R_b represents the basolateral resistance, and C_a and C_b are the apical and basolateral capacitances, respectively, in Figure 3-7. The apical resistance R_a may represent the stereocilia ion channels instead of ion channels in the apical face of the cell itself.

Extracellular stimulus-related potential gradients arise from the voltage drop generated by outer hair cell receptor current across various tissues and membranes [3]. This effect is modeled by a current source, I_1, inside OHC1 in Figure 3-7 for simplicity, which produces an extracellular voltage V.

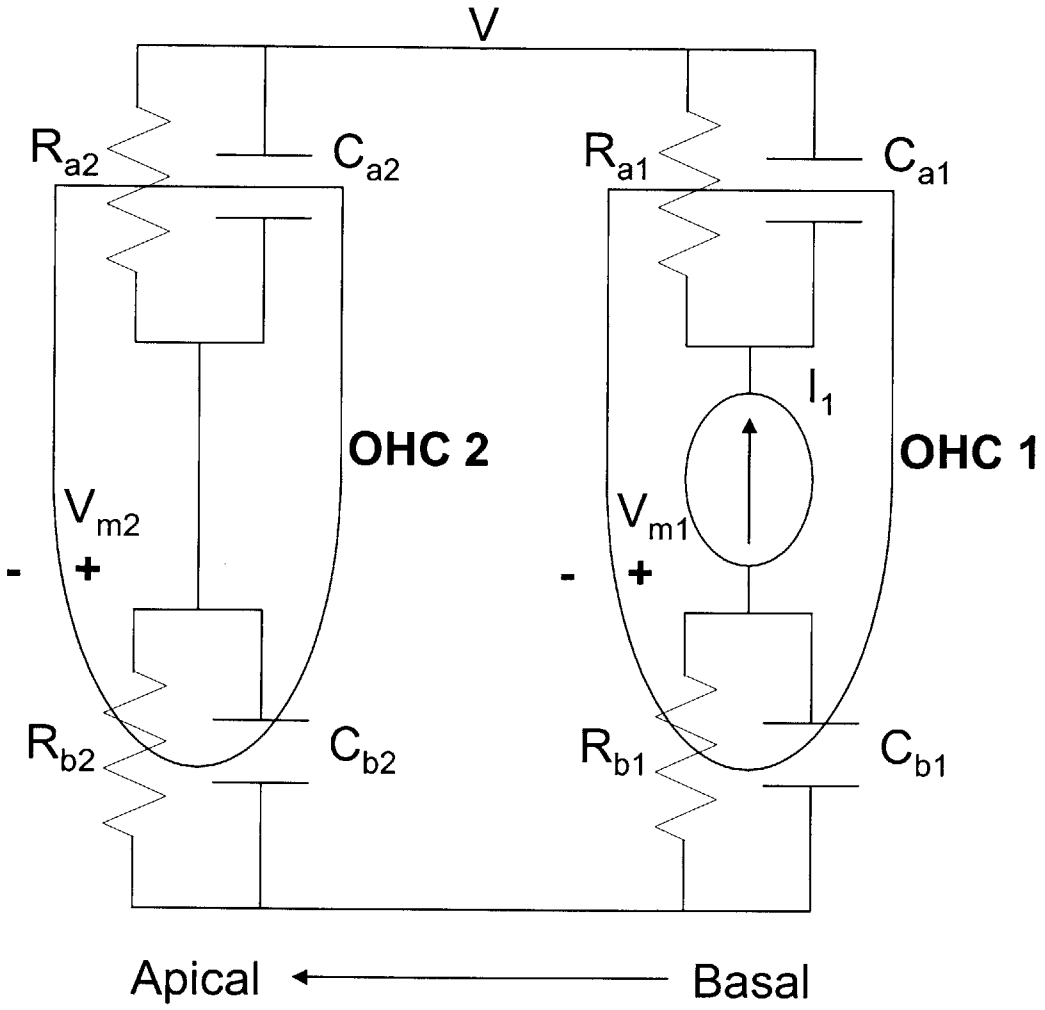

Figure 3-7. Simplified model of the Dallos and Evans extracellular potential gradient theory. Outer hair cells basal (OHC1) to the outer hair cell of interest (OHC2) modulate the extracellular potential. At high frequencies, the membrane voltage of OHC2 is set by a capacitive divider and thus does not tend to zero. Adapted from Dallos and Evans [3].

Based on Figure 3-7 and assuming that the time constant of the apical face of outer hair cells is faster than that of the basolateral face, which is reasonable since the basolateral area is much greater, the resulting transfer function from extracellular

potential, V, to V_{m2} has a low frequency pole followed by a high frequency zero. Thus, at low frequencies, the incoming current drive of OHC2, the outer hair cell of interest, is primarily dominated by the resistive divider across the apical and basolateral sides of the cell. At DC, V_{m2} is simply given by $VR_{b2}/(R_{a2} + R_{b2})$ with no phase shift. At high frequencies, however, the apical and basolateral impedances are dominated by the respective capacitors and thus V_{m2} is $VC_{a2}/(C_{a2} + C_{b2})$. As a result, current is coupled into the OHC of interest through a capacitive divider at higher frequencies [3]. Thus, the membrane voltage of the OHC of interest does not tend to zero at high frequencies (provided that V does not tend to zero) and may be sufficient to generate a motile response. Furthermore, there is no phase shift at very low frequencies or very high frequencies; in the mid-frequency transition region, the phase shift is bounded by $\pm\pi/2$.

Dallos and Evans tested the ability of outer hair cells to operate with a capacitive divider at high frequencies by isolating a single OHC in a microchamber and modulating the extracellular potential with a voltage source; their results are shown in Figure 3-8. The displacement, which is presumably driven by the membrane voltage, does not tend to zero at higher frequencies because of the capacitive divider. Dallos and Evans fit the model described above to the data quite accurately. Thus, a capacitive divider that couples extracellular potential gradients into intracellular membrane voltages at high frequencies may be able to produce enough force and displacement to operate *in vivo*.

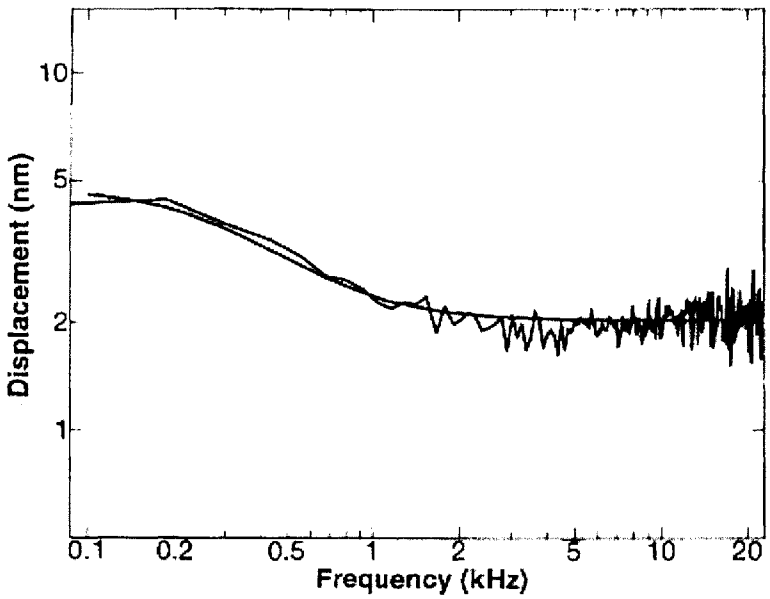

Figure 3-8. Experimental results of the Dallos and Evans model where a single OHC isolated in a microchamber was driven by an external voltage source. The model was fit to the data quite accurately and the displacement of the outer hair cell did not tend to zero at high frequencies. Reproduced from Dallos and Evans [3].

The problem with this model is the lack of experimental evidence to show that capacitively coupled extracellular potential gradients dominate over the stereocilia transducer current at high frequencies. Yates and Kirk [12] measured electrically evoked otoacoustic emissions generated by current that was injected into the scala media that bathes the apical sides of outer hair cells. In addition to simulating with current injection, Yates and Kirk [12] introduced a low-frequency acoustic bias to change the mean conductivity of the ion channels. The observed electrically evoked otoacoustic emissions were modulated by the low-frequency bias, suggesting that capacitive coupling may not be the dominant mechanism for coupling extracellular potential gradients into the outer hair cells [3]. Thus, while the presence of a capacitive divider in outer hair cells has been verified experimentally *in vitro*, it is unclear whether this effect is relevant *in vivo* or *in situ*.

3.6.2 Piezoelectricity and Mechanical Resonance

Mountain and Hubbard suggest that mechanical resonance can reduce the effective impedance seen by the electrical system due to the piezoelectric relationship of OHCs [13]. By assuming that the outer hair cell has a radius R and the motor molecule undergoes an area change, δA, as it transitions between its long and short states and transfers charge z in the process, the ratio of OHC length change to total charge movement satisfies the relationship given by:

$$\frac{\Delta L}{\Delta Q} = \frac{\delta A}{\pi R z}$$

Equation 3-1. Direct coupling of OHC length change with charge displacement in the Mountain and Hubbard piezoelectric model [13].

The coupling in Equation 3-1 is characteristic of piezoelectric systems. Thus the model in Figure 3-9 was adopted with the transformer ratio given by Equation 3-1 [13].

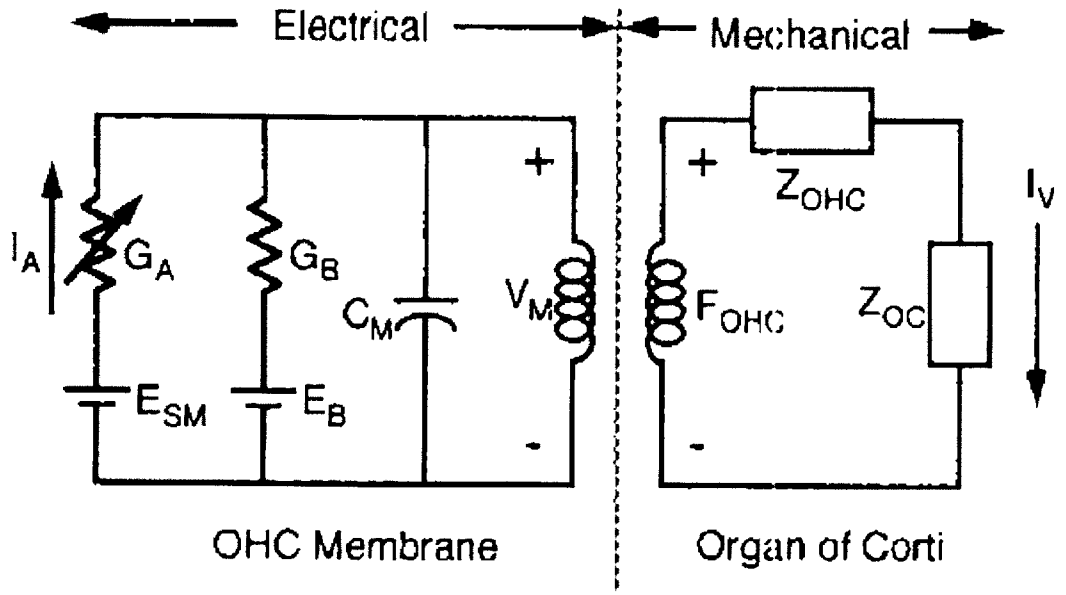

Figure 3-9. Piezoelectric model presented by Mountain and Hubbard [13]. The transformer represents the piezoelectric coupling between the electrical and mechanical subsystems. G_A is the conductance of the stereocilia ion channels, G_B is the basolateral conductance, C_M is the membrane capacitance, and the batteries represent the scala media and basolateral potentials. The mechanical impedances are given by Z_{OHC} and Z_{OC}. I_v is velocity and F_{OHC} is force. Reproduced from Mountain and Hubbard [13].

In such a system, if the mechanical subsystem composed of the OHC and the organ of Corti impedances operated at resonance, the effective mechanical impedance reflected onto the electrical side would be very small. Thus, at mechanical resonance, the membrane voltage would be very low and the majority of the transducer current would be converted into velocity because of the small mechanical impedance. As a result, not much force is needed at resonance to drive the mechanical system and so intracellular voltages, albeit attenuated, may be sufficient [13]. The concept that mechanical resonance can affect the membrane voltage is explored in later sections of this thesis in greater detail, in part inspired by this model.

3.6.3 Piezoelectric Back Displacement Current

Spector et al. have presented a model of OHC electromotility that incorporates the piezoelectric properties of the cell wall and demonstrates that piezoelectricity may prevent severe attenuation of the membrane potential in short OHCs by generating a strain-dependent displacement current [14]. This model assumes that the OHC cell wall satisfies the linear relationships:

$$N_x = C_{11}\varepsilon_x + C_{12}\varepsilon_\theta + e_x\Delta\Psi_c$$
$$N_\theta = C_{12}\varepsilon_x + C_{22}\varepsilon_\theta + e_\theta\Delta\Psi_c$$
$$\frac{dQ}{dS} = -e_x\varepsilon_x - e_\theta\varepsilon_\theta + c\Delta\Psi_c$$

Equations 3-2, 3-3, and 3-4. Linear piezoelectric relationships assumed to hold true for the outer hair cell wall in the Spector et al. model [14].
N_x and N_θ are the stresses in the longitudinal and circumferential directions, ϵ_x and ϵ_θ are the strain components, C_{11}, C_{12}, and C_{22} are the orthotropic elastic moduli, e_x and e_θ are the coefficients of stress per change in membrane voltage, $\Delta\Psi_c$ is the change in the membrane potential, Q is the electrical displacement across the membrane, S is the surface area of the OHC cell wall, and c is the specific capacitance.

Spector et al. assume the current that enters through the stereocilia either exits the cell via membrane ion channels or is displaced across the membrane according to the charge variable, Q, in the equations described above. Assuming that the conductances of

the stereocilia and ion channels in the membrane are given by G_s and G_c and that the voltage drop across the stereocilia is $\Delta\Psi_s$, Kirchkoff's current law yields

$$G_c \Delta\Psi_c + \frac{dQ}{dt} = G_s \Delta\Psi_s$$

Equation 3-5. Current entering the outer hair cell via the stereocilia conductance, G_s, exits through the membrane conductance, G_c, or is displaced across the membrane by the piezoelectric effect via Q. $\Delta\Psi_s$ is the voltage drop across the stereocilia [14].

Assuming that the longitudinal and circumferential strains vary sinusoidally with no DC offset and peak strains ϵ_x^0 and ϵ_θ^0, respectively, that $G_s = G_s^0 + G_s^1 \sin \omega t$, that the strain is uniform throughout the OHC cell wall, and defining the endocochlear potential $\Psi = \Delta\Psi_s + \Delta\Psi_c$, Equation 3-5 can be written as shown in Equation 3-6. In Equation 3-6, the DC value of the membrane potential has been removed, C_c is the whole-cell capacitance, $G = G_c + G_s^0$, and $\beta = -S(\epsilon_x^0 e_x + \epsilon_\theta^0 e_\theta)$, as described by Spector et al. [14].

$$C_c \frac{d\Delta\Psi_c}{dt} + \left(G + G_s^1 \sin \omega t\right)\Delta\Psi_c = G_s^1 \Psi \sin \omega t - \beta\omega \cos \omega t$$

Equation 3-6. Kirchkoff's law for the Spector et al. model assuming sinusoidally varying strains and stereocilia conductance and ignoring constant contributions to the membrane potential [14]. Ψ is the endocochlear potential, which is $\Delta\Psi_c + \Delta\Psi_s$.

To obtain an analytical solution to this problem, Spector et al. assume that in the second term on the left hand side of Equation 3-6, G is the dominant term over $G_s^1 \sin \omega t$ and that the resulting membrane potential, $\Delta\Psi_c$, is sinusoidal. This leads to the solution in Equation 3-7. Essentially, the approximate membrane potential is given by a left half plane pole followed by a right half plane zero.

$$\Delta\Psi_c = \frac{G_s^1 \Psi - s\beta}{sC_c + G}$$

Equation 3-7. Solution for the membrane potential $\Delta\Psi_c$ in the Spector et al. model [14].

However, Spector et al. present their results in magnitude and phase form. The magnitude and phase of the membrane potential can be found by substituting $s = j\omega$, multiplying the numerator and denominator by the complex conjugate of the denominator,

and finding the magnitude and phase of the resulting complex vector. The resulting answers are given in Equation 3-8 and Equation 3-9 and are consistent with Equation 3-7.

$$|\Delta\Psi_c| = \frac{\sqrt{[f_1(\omega)]^2 + [f_2(\omega)]^2}}{f_3(\omega)}$$

where

$$f_1(\omega) = G_s^1 G\Psi - \beta\omega^2 C_c$$

$$f_2(\omega) = \omega\left(C_c G_s^1 \Psi + \beta G\right)$$

$$f_3(\omega) = \omega^2 C_c^{\,2} + G^2$$

Equation 3-8. Magnitude of the membrane potential in the Spector et al. model [14].

$$\Theta = -\frac{180^\circ}{\pi}\arctan\frac{f_2(\omega)}{f_1(\omega)}$$

Equation 3-9. Phase of the membrane potential in the Spector et al. model [14].

By assuming appropriate values for the parameters in the system, Spector et al. conclude that the magnitude asymptotes to a value of β/C_c as the frequency approaches infinity while the phase approaches 0 in short cells [14]. Thus, in short OHCs, the receptor potential reaches a finite value for high frequencies and does not exhibit the sharp rolloff that would be expected in the traditional RC analysis of the system ($\beta = 0$). This effect, however, is weaker in long cells, which is concomitant with the experimental result that the apical region of the cochlea does not require great action of the cochlear amplifier to operate at low frequencies. The Bode magnitude plot for varying values of β in short OHCs is shown in Figure 3-10, with a low-frequency value of 2.5 mV. The corresponding phase plot is available in Figure 3-11 and indicates that the phase tends to 0° at high frequencies.

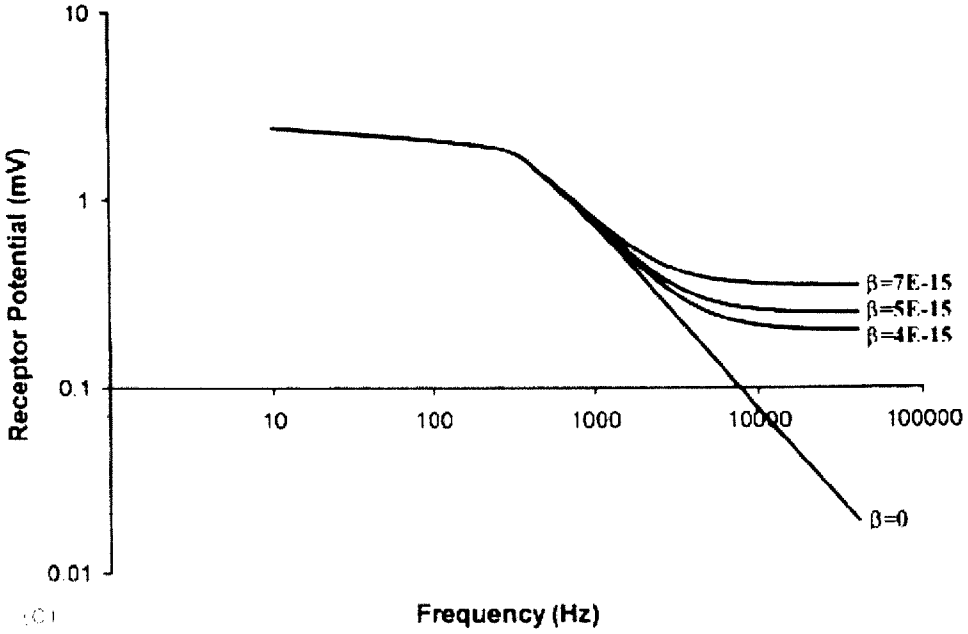

Figure 3-10. Bode magnitude plot of the receptor potential in short OHCs in the Spector et al. model. For finite values of β, the receptor potential does not tend to zero as the frequency increases but instead approaches an asymptotic value. Reproduced from Spector et al. [14]

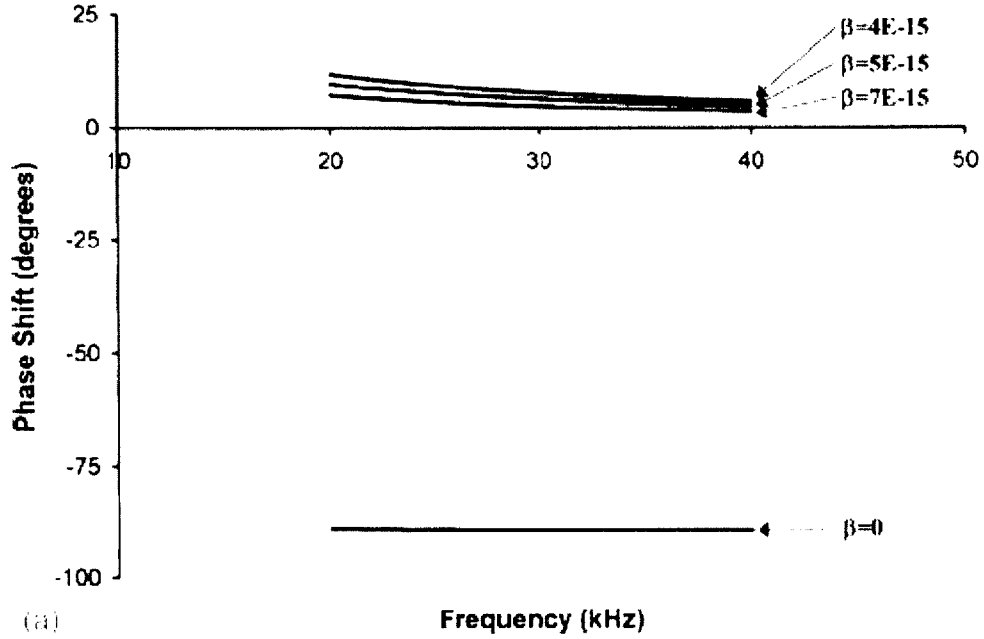

Figure 3-11. Bode phase plot of the receptor potential in short OHCs in the Spector et al. model. According to Spector et al., for finite values of β, the phase of the receptor potential tends to 0°. However, as shown in Section 3.6.3, this is incorrect; instead, the phase of the receptor potential should tend to -180°. Reproduced from Spector et al. [14]

However, the phase data shown exhibits incorrect behavior; instead, the phase should tend to -180° according to the model. The error made by Spector et al. in

calculating the phase of the voltage stems from their use of Equation 3-9. As ω approaches infinity, $f_2(\omega)/f_1(\omega)$ tends towards zero; using arctangent in the first quadrant (or fourth) yields $\Theta \rightarrow 0^\circ$. However, upon closer inspection, $f_1(\omega)$ approaches $-\infty$ as ω increases while $f_2(\omega)$ always stays positive. Thus, arctangent in the second quadrant must be used, resulting in $\Theta \rightarrow -180^\circ$ instead! This conclusion is bolstered by finding the phase of Equation 3-7 for large values of $s = j\omega$, which tends towards -180° as well.

The fact that the receptor potential is almost -180° out of phase with the input current calls into question the validity of this model. This suggests that for high frequencies, incoming current will cause hyperpolarization of the membrane instead of depolarization. Whether or not such a system is biologically realistic is questionable and must be verified with empirical data. Furthermore, the assumption made by Spector et al. that the peak strain is a constant which is essentially independent of the frequency of operation needs to be justified with experiment to confirm or reject this model. The authors also assume zero phase shifts between the strains and stereocilia conductance but do not justify this simplification, which may be untrue depending on the mechanical characteristics of the system. Lastly, the idea that the receptor potential asymptotes at high frequencies rather than approaching zero is unlikely from an engineering viewpoint. In most engineered systems, filtering is imposed at frequencies outside those of interest to limit the noise that can affect the system, resulting in a sharp cutoff in the transfer function generally at high frequencies. Failure to bandlimit the frequency response of a sensory system would probably result in a tremendous loss of precision due to noise. Nonetheless, the idea that the piezoelectric properties of the outer hair cell may assist in

limiting the loss of membrane potential due to the membrane time constant is important and should be addressed, albeit in a different fashion, in future work.

3.6.4 Multiple Mode Traveling Wave Model of the Cochlea

In a traveling-wave model of the cochlea developed by Hubbard, local negative feedback that couples two modes of vibration together can generate realistic results when compared with experimental data [15]. The electrical analog for the mechanical system is shown in Figure 3-12. The top line is a traditional resonant basilar membrane model while the bottom line is not composed of resonant sections [15]. The coupling between the two modes results from the two current sources, I_{t1} and I_{t2}, which are dependent on gain constants, capacitances, and voltages across the capacitors. Since the gain factors, $g_{2\text{-}1}$ and $g_{1\text{-}2}$ are both negative, the coupling generated by I_{t1} and I_{t2} is negative in sign. For example, if V_2 increases, I_{t1} decreases, V_1 increases, and I_{t2} decreases, which attempts to reduce V_2 and thus the coupling exhibits negative feedback. It is interesting to note that negative feedback instead of the oft-assumed positive feedback is used in this model.

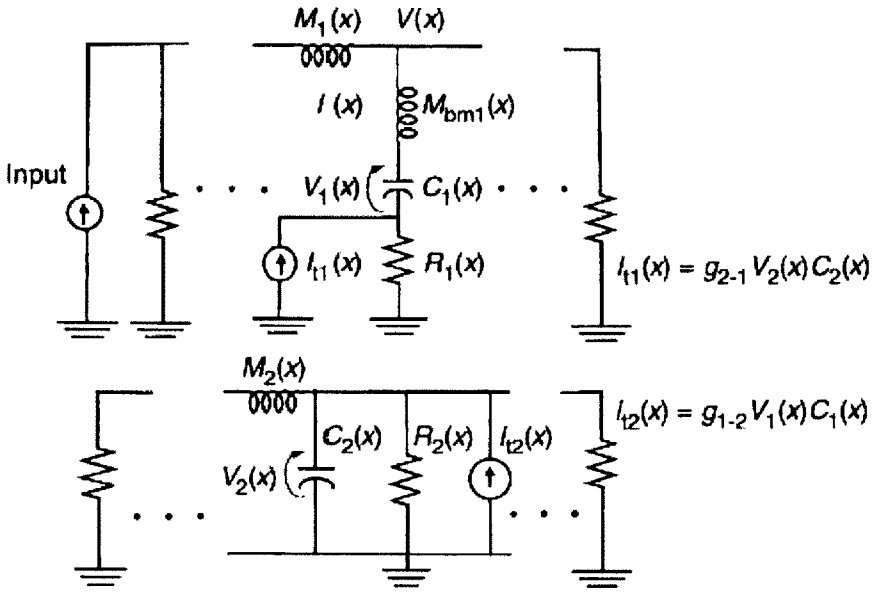

Figure 3-12. Hubbard's traveling-wave model of the cochlea. Currents represent volume velocity while voltages correspond to pressure. Inductors are acoustic mass, capacitors are compliance, and resistors are damping. Reproduced from Hubbard [15].

According to Hubbard, waves travel at the same velocity on both the lines when they are coupled together [15]. In the sections basal to the resonant location, the wave velocity is essentially set by the top line. However, near resonance, the velocity slows down to that of the bottom line. Over this region, amplification of the incoming signal is considerable and produces the active peak expected from the action of the cochlear amplifier. This model matches experimental data closely in both phase and magnitude, as shown in Figure 3-13 and Figure 3-14.

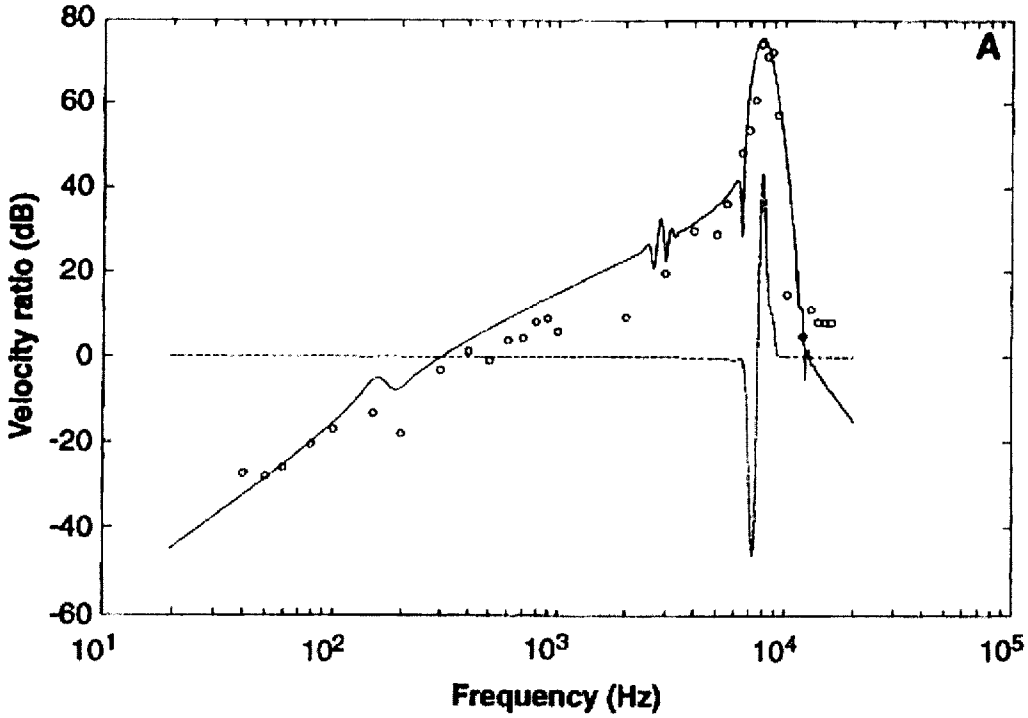

Figure 3-13. The velocity ratio between the basilar membrane and the stapes for the model (solid line) with experimental data from a chinchilla (open circles).
The dashed line is the power calculated from the model. Reproduced from Hubbard [15].

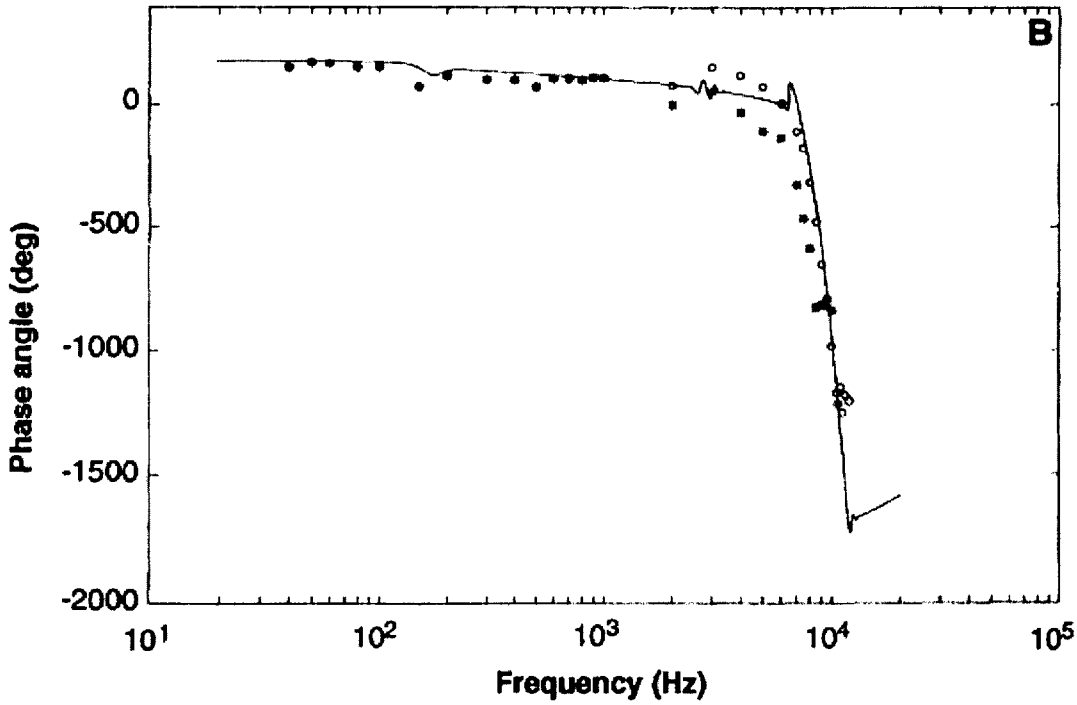

Figure 3-14. The phase angle for the model (solid line) and experimental data from chinchillas (open and closed circles).
Reproduced from Hubbard [15].

Although Hubbard's model does not identify a clear mechanism for OHC electromotility or clear analogs between the parameters and cochlear micromechanics, it suggests that intermode coupling via negative feedback may be responsible for cochlear amplifier characteristics [15]. Perhaps multiple traveling-wave lines exist in the biological cochlea with beneficial system characteristics. This idea is explored later in this thesis along with the concept of multiple resonating modes.

3.6.5 Inductive Ion Channels

Ospeck et al. posit that a voltage-dependent ion channel may add an inductive component to the membrane to resonate out the membrane capacitance and extend the limiting frequency of the intracellular voltage [16]. In their study, the authors assume that multiple modes of vibration in the organ of Corti allow OHC vibration to have the correct phase to optimally counter viscous drag, which they claim is dominated by gap drag between the reticular lamina and tectorial membrane [16]. These simplifications are not based on cochlear micromechanics but on the assumption of optimality.

Ospeck et al. present a hypothetical two-state ion channel and demonstrate that it can have certain inductive characteristics for $\omega\tau >> 1$, where ω is the frequency and τ is the relaxation time constant of the channel assuming Hodgkin-Huxley dynamics, as in Equation 3-10 [16]. In the two-state model, P is the open probability of the channel. The transition from the closed and open state has the rate constant k_+ while the transition from the open to closed state has the rate constant k_- and thus $\tau = (k_+ + k_-)^{-1}$ [16]. The addition of an inductive ion channel helps to cancel out the effect of the membrane capacitance by resonant effects and may lead to an effective speedup of the membrane time constant. Based on this model, Ospeck et al. estimate that the OHC inductance needs to be about

130 H [16]. Multiple-state ion channels with more complex gating characteristics may provide better inductive characteristics. As seen in Figure 3-15, the four-state model provides a more realistic fit to a pure inductor in response to a step in voltage.

$$\frac{dP(V_m,t)}{dt} = \frac{P_\infty(V_m) - P(V_m,t)}{\tau}$$

Equation 3-10. Hodgkin-Huxley differential equation governing the open probability of the two-state ion channel presented by Ospeck et al. [16]

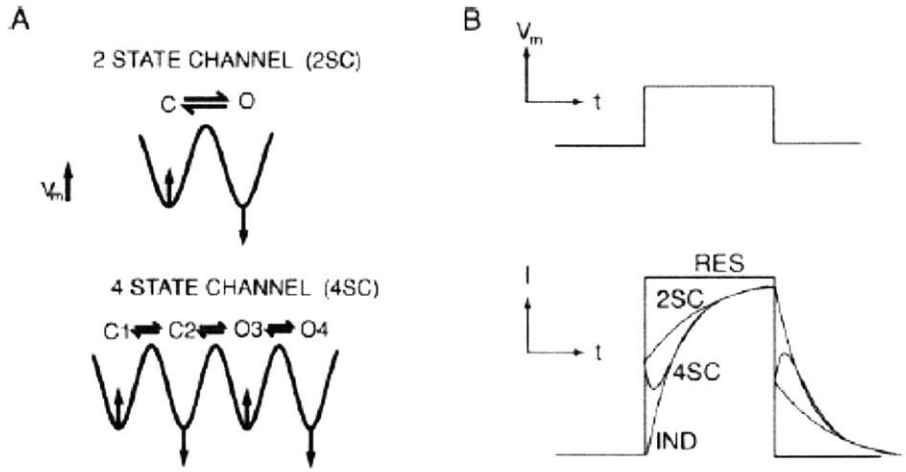

Figure 3-15. (A) Hypothetical free energy profiles of two state and four state ion channels are shown. (B) The four state ion channel (4SC) matches the inductive response to a step in voltage (IND) better than the two state model (2SC). The resistor (RES) response in current follows the voltage exactly. Reproduced from Ospeck et al. [16]

Inductive ion channels are known to exist in the squid giant axon but have not been found in OHCs yet [16]. The validity of this analysis rests on the assumption that outer hair cells have optimal phase to counteract viscous drag and that inductive ion channels can be eventually found. Whether or not these assumptions can be confirmed via experimental data remains to be seen.

3.6.6 Hair Bundle Amplification

Despite all the possible explanations presented by the studies described above, perhaps somatic OHC electromotility is not responsible for the cochlear amplifier in mammals. Martin and Hudspeth report physiological evidence that the hair bundles

present on hair cells of bullfrogs can become entrained with mechanical stimulation [17]. They posit that hair bundle motion may act to amplify incoming signals and could thus the cochlear amplifier. They placed a fiber tip against the stereocilia of outer hair cells and observed the motion of the fiber base as well as the hair bundle. Without any stimulation by the fiber, the hair bundle shown in Figure 3-16 spontaneously oscillated at about 9 Hz. Thus, spontaneous oscillation of the hair bundle is a candidate mechanism for the generation of spontaneous otoacoustic emissions [17]. The fiber base was swept from 5 Hz to 21 Hz and at about 7.5 Hz, the hair bundle entrained the fiber motion, indicating that active amplification is possible, at least at low frequencies [17]. Martin and Hudspeth found that the mechanical energy they inputted was less than that dissipated by viscous drag and thus concluded that the hair bundles provided power into the system [17].

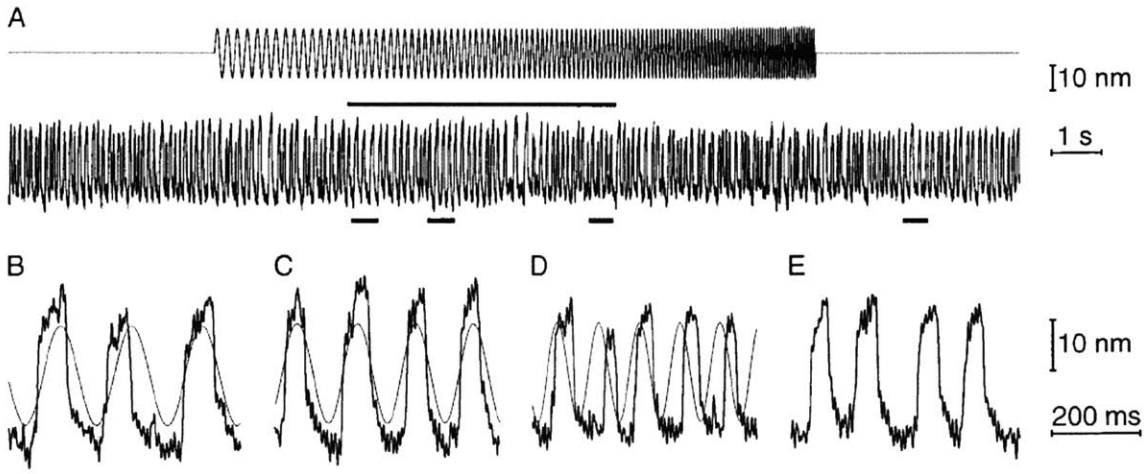

Figure 3-16. A bullfrog OHC hair bundle can entrain the motion of a fiber placed against it. Part A shows the motion of the stimulus fiber as it is swept from 5 Hz to 21 Hz (top) and the oscillation of the hair bundle (bottom). Without mechanical stimulation, the hair bundle spontaneously oscillated at ~9 Hz. At ~7.5 Hz stimulation (part C), the hair bundle entrained the mechanical motion. At ~6.5 Hz (part B), the hair bundle led the fiber while at ~11 Hz, the hair bundle lagged. Reproduced from Martin and Hudspeth [17].

There are two candidates in the literature for the motor that may drive hair bundle amplification. The first is a myosin motor in the hair bundle that could be activated by

stress experienced as a result of hair bundle motion, thus undergoing abrupt power strokes to amplify the signal [18]. Myosin may also be responsible for adaptation in hair cells and could perhaps play a dual role in acting as a power source. The other potential mechanism for hair bundle motion is the mechanical operation of transduction channels in the stereocilia themselves [18]. As shown at the top of Figure 3-17, excitatory displacement of the hair bundle allows an ion, potentially Ca^{2+}, to enter, bind to the ion channel, and promote closure of the channel. This effect cause the tip link tension to increase, thus pulling the hair bundle in the opposite direction (bottom). If timed to coincide with the negative phase of the input, this mechanisms may provide mechanical amplification and entrainment.

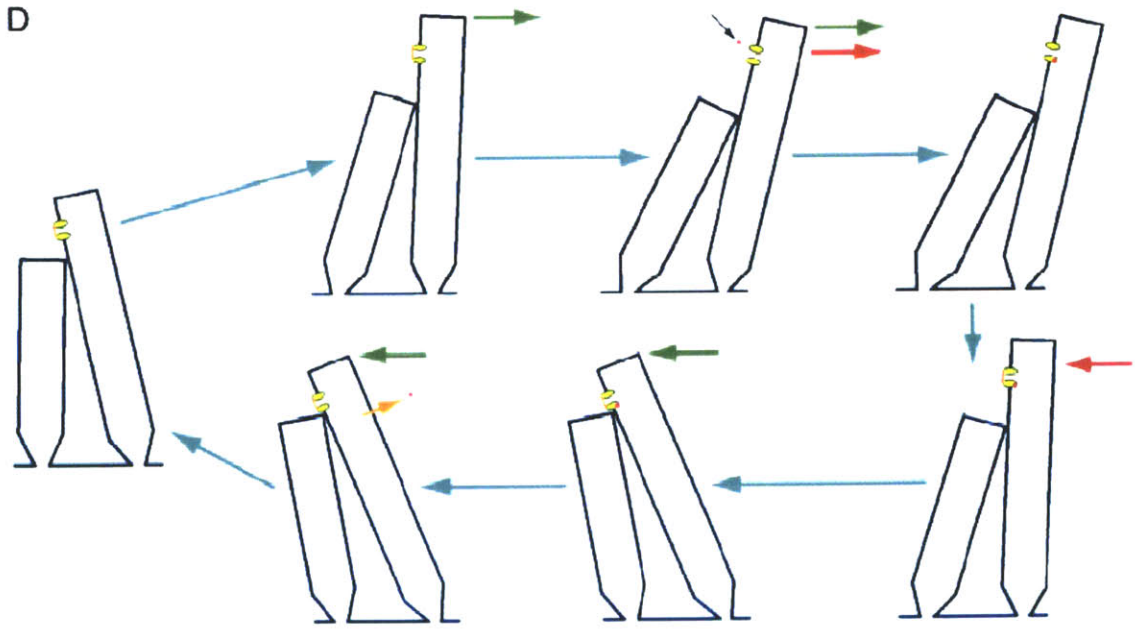

Figure 3-17. Hypothetical mechanism for hair bundle amplification involving transduction channels in hair cells and Ca^{2+} ions (red dot).
Displacement in the positive direction by the input allows Ca^{2+} to enter the ion channel and bind to the channel, promoting closure. This effect snaps the channel shut, resulting in additional tip link tension that pulls the hair bundle in the opposite direction during the negative phase of the input, providing amplification. Reproduced from Hudspeth et al. [8]

Since OHCs in non-mammals do not exhibit somatic motility, it is likely that hair bundle amplification is responsible for the cochlear amplifier in lower animals. However,

whether or not this mechanism is significant in mammals has yet to be resolved by experiment. It is also unclear if hair bundle amplification can operate at the extremely high frequencies of hearing that can be attained by bats and other mammals since the data that has been presented has been taken for very low frequencies.

4 Local Outer Hair Cell Model

Outer hair cells are embedded in between the reticular lamina and the basilar membrane. When OHCs contract, the reticular lamina experiences a downwards force while the basilar membrane is pulled upwards. Because depolarization of the outer hair cell, which leads to contraction, is generated by upwards movement of the reticular lamina, there is negative feedback around the RL. Essentially, displacement of the RL in the positive vertical direction (towards the modiolus) causes the stereocilia to pivot away from the modiolus, which depolarizes the membrane and causes OHCs to shorten. This tends to tilt the stereocilia back towards the modiolus and hyperpolarizes the membrane. This argument relies on the physiological anatomy of the system shown in Figure 3-5. Similarly, there is positive feedback by the basilar membrane, since upwards movement of the BM generates depolarization, which then tends to increase the upwards displacement of the BM by OHC contraction.

However, since the reticular lamina exhibits more displacement than the basilar membrane with OHC contraction and elongation, negative feedback should dominate in this system. This negative feedback loop includes the outer hair cell membrane time constant because the outer hair cell force determines the movement of the associated mechanical structures. As seen in Section 2, negative feedback in motor systems is often used to speed up slow systems. Thus, in this section, I will demonstrate how negative feedback can accelerate the slow membrane time constant and generate a sharpening of the basilar membrane and reticular lamina displacements.

4.1 Mechanical Model with One Resonator and One Source of Damping

The electrical analog of the mechanical system described in this section can be represented as shown in Figure 4-1. In this representation, the currents, I_{in} and I_{fb}, represent the input force on the basilar membrane structure and the feedback force resulting from the electromotile response of the OHCs, respectively. The dependent current source I_{fb} represents the feedback force and will be described later. The voltages, V_{rl} and V_{bm}, represent the velocities of the reticular lamina and basilar membrane, respectively. The mechanical admittances of the reticular lamina, the outer hair cell, and the basilar membrane are given by Y_{rl}, Y_{ohc}, and Y_{bm}, respectively.

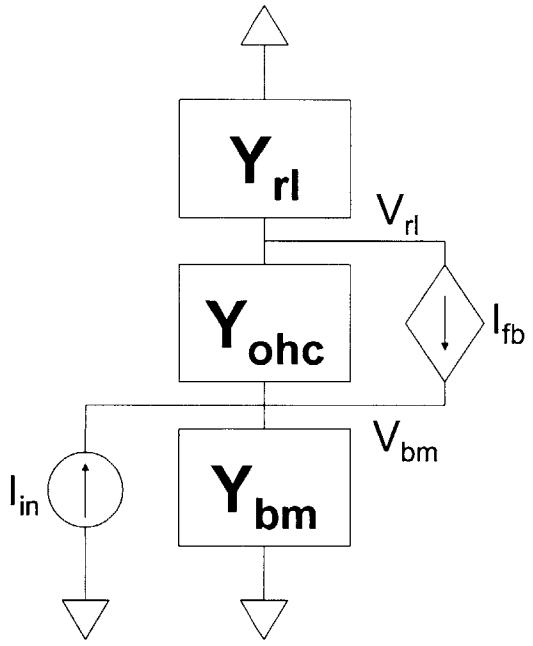

Figure 4-1. The block representation of the OHC system with surrounding structures using currents to represent forces and voltages to represent velocities. Same as Figure 4-5.

Even without inserting any parameters in for the admittances, this model assumes, for simplicity, that the tectorial membrane is rigid and does not move. The validity of this assumption will need to be evaluated in future work. Since the tectorial membrane does move in the biological system, the effective values of the parameters used for the

reticular may lump in the properties of the tectorial membrane. Dynamic properties of the tectorial membrane have been measured and should be incorporated in later work [19].

Determining the appropriate parameters for the admittances is crucial for a functional model of the cochlea. In particular, there must be at least one source of viscous damping that acts on the motion of the cochlea according to Gold [20]. Ospeck et al. assume that the drag that results from the gap between the tectorial membrane and the reticular lamina (gap drag) is dominant over any other sources of viscous damping in the system [16]. The boundary layer for periodic motion in a fluid is given by:

$$\delta = \sqrt{\frac{2\upsilon}{\omega}}$$

Equation 4-1. Boundary layer δ for periodic motion with frequency ω [21]. υ is the kinematic viscosity, which is given by the viscosity η divided by the density ρ.

Evaluating Equation 4-1 at 100 kHz, where $\eta = 0.72 \times 10^{-3}$ Pa·s for perilymphatic fluid and $\rho = 1.0 \times 10^{3}$ kg/m^3, assuming a density close to that of water, $\delta = 1.51$ μm. Given that the tallest stereocilia in the basal turn of the cochlea, and thus the gap between the TM and the BM, in the guinea pig and the leaf-nosed bat are about 1.0 μm, the viscous forces from the gap drag may be on the same order of magnitude as inertial forces [10][22]. For now, however, the inertial effects are ignored though this assumption needs to be verified in future work. This is accurate for low Reynolds number flow. The viscous force acting on an oscillating plate of area A with velocity V can be expressed as:

$$F = \frac{\eta V A}{\delta}$$

Equation 4-2. The viscous force acting on an oscillating plate of area A with velocity V for a fluid with viscosity η and boundary layer dimension δ [21].

Since the dimension of the gap between the TM and the BM is slightly smaller than that of the boundary layer δ, the force is evaluated by using $\delta = 1.0$ μm, the gap size. According to Brownell et al., a single OHC can be modeled as a cylinder with a diameter of about 9 μm [1]. Assuming that the area of the oscillating plate in Equation 4-2 is equal to the area of the top of the OHC, $A = \pi \cdot (4.5\ \mu m)^2$. The outer hair cell's effect on the reticular lamina or basilar membrane is similar to indenting a cell membrane with a cylindrical probe. As described by Kamm [23], the volume of deformation scales as the third power of the outer hair cell radius ($\sim r^3$) and so the area of deformation should be approximately $\sim r^2$. This is an estimate of the space constant of the system and should be confirmed by experiment, though it suggests that assuming the area of the oscillating plate is equal to that of the area of the top of the OHC is a valid approximation. This analysis yields a damping coefficient $\xi_{rl} = 4.58 \times 10^{-8}$ N·s/m.

The stiffness of the basilar membrane measured in the pectinate zone with a 20 μm diameter probe is 1.1 N/m [24]. Scaling to the area of a single OHC yields a basilar membrane stiffness, $k_{bm} = 0.22275$ N/m. Since the motion of the reticular lamina is greater than that of the basilar membrane by about 5 to 10 times in cochlear turn 3 of the guinea pig in response to OHC contraction, we approximate the stiffness of the RL to be about 8.5 times less than that of the BM [11]. Thus, $k_{rl} = 0.0262$ N/m. According to personal communications with Prof. Peter Dallos, the stiffness of a single outer hair cell is approximately 360/L mN/m, where L is the cell length given in μm [25]. Given that the shortest hair cell in basal portion of the bat cochlea is about 8 μm [8], the stiffness of the OHC is about $k_{ohc} = 45$ mN/m. The mass of the basilar membrane is estimated by assuming a density of water ($\rho = 1.0 \times 10^3$ kg/m^3) and considering a volume defined by

the area of an OHC cell times the thickness of the basilar membrane. The thickness at the basal end is about 7 μm and thus the mass of the BM is about $m_{bm} = 4.45 \times 10^{-13}$ kg [26]. The effective mass of the basilar membrane, however, may need to take into account the fluid mass displaced by movement of the basilar membrane as well as the mass of the Deiters' cells in later revisions. For now, these masses are assumed to be negligible.

With these parameter values, we can assemble a mechanical model of the system. Assuming that the gap drag is the only significant source of viscous damping in the system, the model used is shown in Figure 4-2. Translating between this and the electrical analog shown in Figure 4-1,

$$Y_{bm} = \frac{k_{bm}}{s} + m_{bm} \cdot s$$

Equation 4-3. Basilar membrane admittance for the electrical analog of the model in Figure 4-2.

$$Y_{rl} = \frac{k_{rl}}{s} + \xi_{rl}$$

Equation 4-4. Reticular lamina admittance for the electrical analog of the model in Figure 4-2.

$$Y_{ohc} = \frac{k_{ohc}}{s}$$

Equation 4-5. Outer hair cell admittance for the electrical analog of the model in Figure 4-2.

$$I_{fb} = F_{fb}$$

$$I_{in} = F_{in}$$

Equations 4-6 and 4-7. Currents for the electrical analog of the model in Figure 4-2.

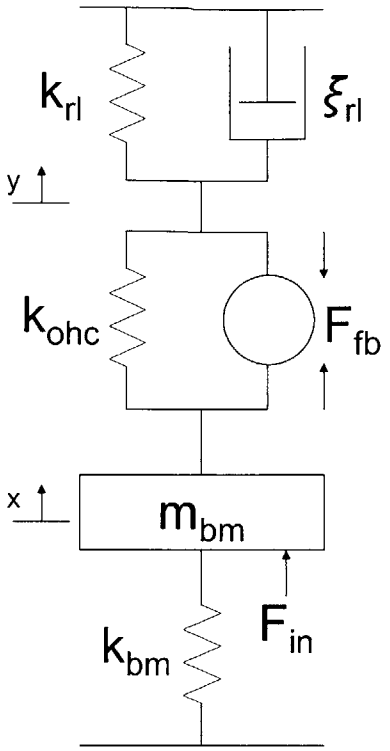

Figure 4-2. Simple mechanical model for the local system.
k represents a spring constant, m represents mass, and ξ represents a damping coefficient. The position of the basilar membrane is given by x while the position of the reticular lamina is given by y.

4.2 Mechanical Model with One Resonator and Two Sources of Damping

However, the simple mechanical model of Figure 4-2 is likely to be inadequate. For example, assume that the feedback force is completely off, so that $F_{fb} = 0$. Then, the free-body equations are given by:

$$F_{in} = k_{bm} \cdot x + m_{bm} \cdot \ddot{x} + k_{ohc}(x - y)$$
$$0 = k_{rl} \cdot y + \xi_{rl} \cdot \dot{y} + k_{ohc}(y - x)$$

Equation 4-8 and Equation 4-9. Free-body equations with no feedback forces ($F_{fb} = 0$) for the model in Figure 4-2.

Solving, we find that:

$$\frac{x}{F} = \frac{1}{k_{bm} + m_{bm} \cdot s^2 + \frac{k_{ohc}(k_{rl} + s \cdot \xi_{rl})}{k_{ohc} + k_{rl} + s \cdot \xi_{rl}}}$$

Equation 4-10. Input-output relationship for the model in Figure 4-2 with no OHC motility.

As expected, if ξ_{rl} is made arbitrarily small, the system becomes purely resonant with no damping. However, if the damping coefficient ξ_{rl} is made arbitrarily large, the system also tends towards pure resonance with no damping at all because the third term in the denominator of Equation 4-10 will not depend on s. This goes against the intuition that increased damping should lead to an increasingly damped system. Essentially, the dashpot in Figure 4-2 becomes so exceedingly slow that there is almost no motion in the RL and so the resonant BM mass and spring can move as if they see no damping at all. Only at an intermediate value of ξ_{rl} will significant damping be seen. This effect is seen in Figure 4-3 as the intermediate value of ξ_{rl} yields the most damped (lowest Q) system while the lower and higher values of the damping coefficient yield less damping.

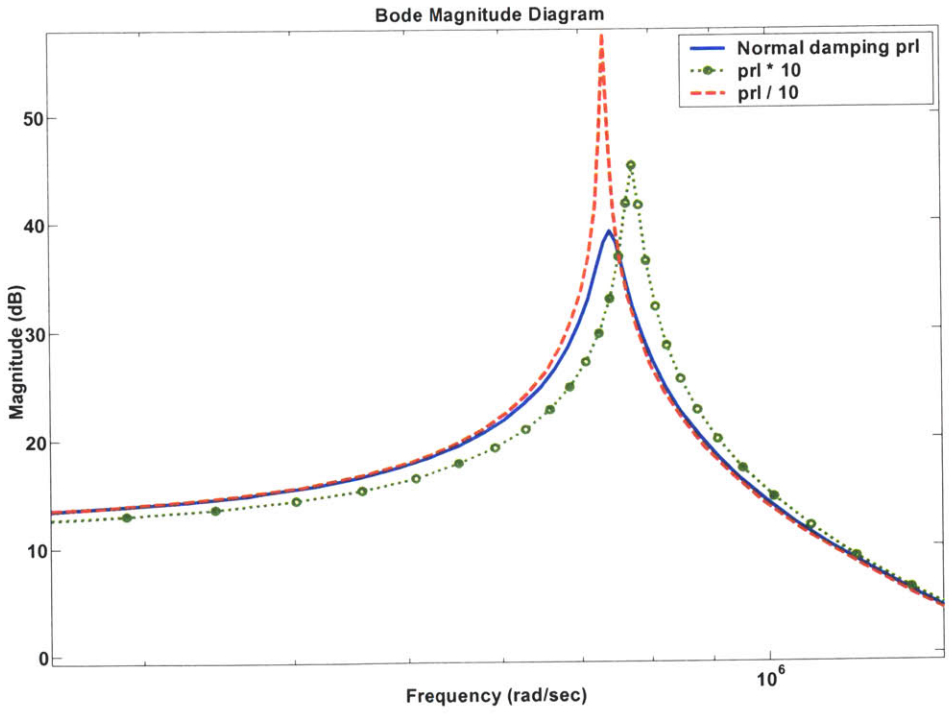

Figure 4-3. The Bode magnitude plot from input force to output BM displacement of Equation 4-10 for different values of ξ_{rl} (prl on the plot).
The solid blue line represents the value for ξ_{rl} derived above. The dotted and circled green line represents ξ_{rl} x 10 while the dashed red line represents ξrl / 10.

As a result of this anomaly, we may need to introduce another source of damping into the system of Figure 4-2 to produce realistic BM motion. A dashpot in parallel with k_{bm} and m_{bm} would yield a damping term that would clearly lower the Q of the BM as it increases and raise the Q as it decreases. Since the boundary layer derived above has a dimension of about 1.51 μm and the BM vibration has a dimension of about 100 nm peak-to-peak [16], we approximate the BM damping coefficient according to Equation 4-2, yielding $\xi_{bm} = 3.033 \times 10^{-8}$ N·s/m. Thus, we modify Equation 4-3 to include this extra damping term, which gives a new expression for Y_{bm}:

$$Y_{bm} = \frac{k_{bm}}{s} + \xi_{bm} + m_{bm} \cdot s$$

Equation 4-11. Modified version of Equation 4-3 to include a damping term.

Thus, the new mechanical model is shown in Figure 4-4.

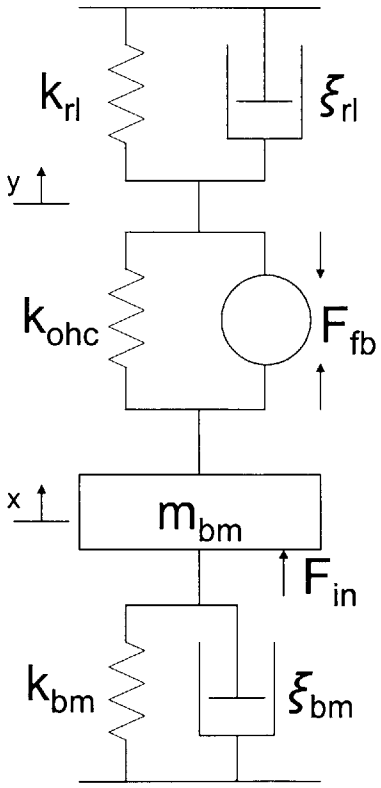

Figure 4-4. Modified mechanical model of Figure 4-2 to include damping for the basilar membrane.

4.3 Active Component Model Derivation

Before we can derive the equivalent block diagrams for the system, we must determine the relevant feedback forces generated by the active components. In this thesis, I assume that the feedback force F_{fb} is composed solely of F_{ft}, the forward transduction force which is due to the displacement of the RL tilting the stereocilia, causing a membrane potential change and a resulting force. Whether or not a piezoelectric force that is generated by a strain-dependent back displacement current should be included will be determined in future work. For estimating F_{ft}, we assume that a 14.6 nm RL displacement causes a 1° cilia rotation according to Dallos [25], the height of the a hair bundle is 1 μm, and the probability that the hair bundle is open for a given hair bundle displacement is $(25\ \text{nm})^{-1}$ [27], where hair bundle displacement is given by the height of the hair bundle times the angle of deflection. We also assume that the maximum hair bundle conductance (g_t) is 28 nS, the gain from membrane potential to force is 0.1 nN/mV, that the endocochlear potential (v_{ec}) is 80 mV, the resting potential (v_r) of an OHC is about -70 mV, the basolateral potassium conductance (g_K) is 50 nS, and the membrane capacitance (C_m) is 15 pF, according to Ospeck et al. [16]. Then, the linearized gain from reticular lamina displacement to force is given by:

$$F_{ft} = 0.1\frac{nN}{mV}\cdot\frac{1/g_K}{\frac{C_m}{g_K}s+1}\cdot(v_{ec}-v_r)\cdot g_t\cdot\frac{1}{25nm}\cdot 1\mu m\cdot\frac{\pi\, rad}{180^\circ}\cdot\frac{1^\circ}{14.6nm}\cdot y = \frac{k_t\cdot y}{\tau s+1},$$

$$\tau = 0.3ms, k_t = 0.402\frac{N}{m}$$

Equation 4-12. The linear forward transduction gain from reticular lamina displacement to force.

4.4 Block Diagrams of the Two Proposed Systems

To more clearly understand the relationships between the active feedback and the resulting BM and RL responses, given by the variables x and y in the models above,

block diagrams can be drawn for the two proposed systems. The variables used in the block diagrams are summarized in Table 4-1. Of course, as for most biological systems, these parameters may vary but are probably good estimates within an order of magnitude.

Table 4-1. Parameters and variables used in block diagrams for models described above.

Name	Description	Value
x	Basilar membrane displacement	N/A
y	Reticular lamina displacement	N/A
k_{bm}	Basilar membrane stiffness	0.22275 N/m
ξ_{bm}	Basilar membrane damping	3.033×10^{-8} N·s/m
m_{bm}	Basilar membrane mass	4.45×10^{-13} kg
k_{ohc}	Outer hair cell stiffness	45 mN/m
k_{rl}	Reticular lamina stiffness	0.0262 N/m
ξ_{rl}	Reticular lamina damping	4.58×10^{-8} N·s/m
F_{ft}	Force generated by forward transduction	$\frac{k_t \cdot y}{\tau s + 1}$
k_t	Reticular lamina displacement to force gain for F_{ft}	0.402 N/m
τ	Outer hair cell membrane time constant	0.3 ms

4.4.1 Is there sufficient membrane voltage?

One of the primary questions that exists in the literature is whether or not there is sufficient voltage at high frequencies to produce the necessary feedback force. To examine this question, we simplify the block diagram by ignoring the piezoelectric force and only considering F_{ft}. We know from the derivation above that the membrane voltage that drives somatic motility is given by F_{ft} divided by the voltage to force gain, 0.1 nN/mV. Thus, using the electrical analog of the mechanical system, we can derive the block diagram shown in Figure 4-6, which can be simplified into Figure 4-7. Figure 4-1 is reproduced here as Figure 4-5 for reference.

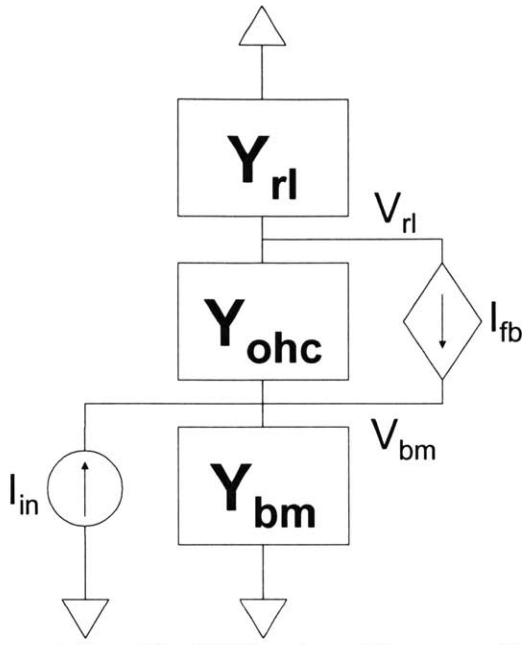

Figure 4-5. The block representation of the OHC system with surrounding structures using currents to represent forces and voltages to represent velocities. Same as Figure 4-1.

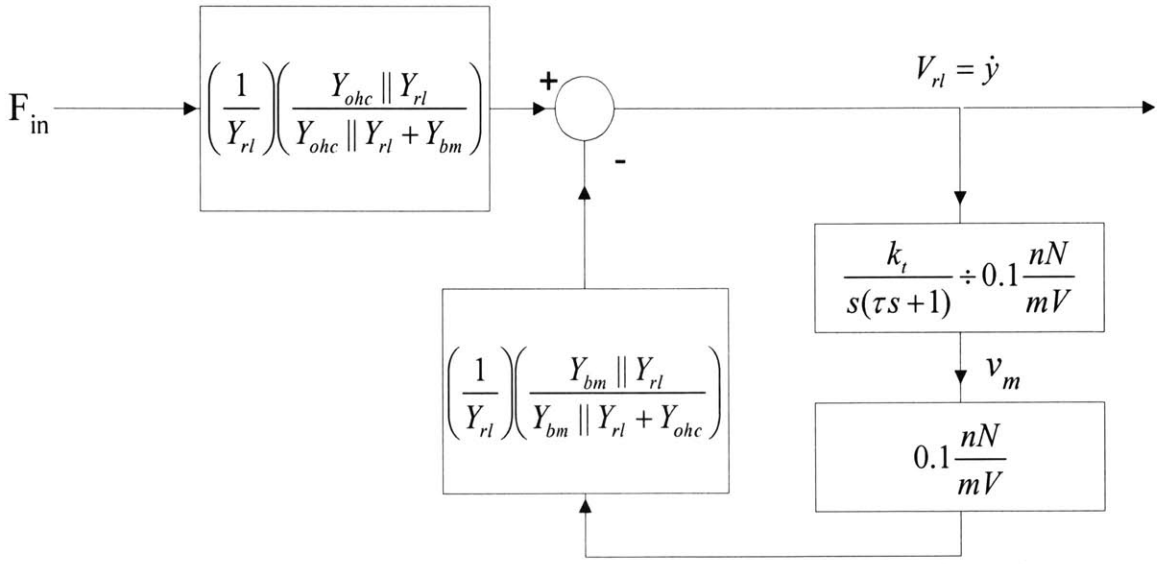

Figure 4-6. Block diagram of both models with the piezoelectric force ignored.

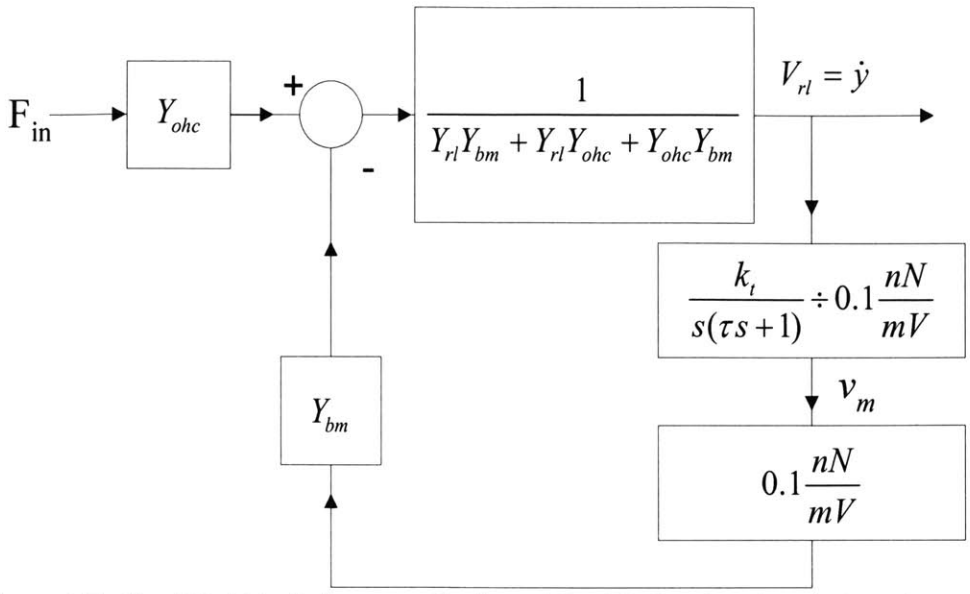

Figure 4-7. Simplified block diagram of both models with the piezoelectric force ignored.

The loop transmission is given by Equation 4-13 and is general for the two models except that the piezoelectric force is ignored.

$$L(s) = \frac{k_t}{s(\tau s+1)} \frac{Y_{bm}}{Y_{bm}Y_{ohc} + Y_{bm}Y_{rl} + Y_{rl}Y_{ohc}}$$

Equation 4-13. Loop transmission of the block diagram shown in Figure 4-6.

4.4.1.1 Model with One Source of Damping and No Piezoelectric Force

Substituting in values for the model with only one source of damping, we find that the system can be written in standard root locus form as shown in Equation 4-14. The root locus plot is included in Figure 4-8 and shows poles located at s = -3333, -1.51 x 10^6, and -1.71 x $10^4 \pm$ j 7.41 x 10^5 and zeros at $\pm$ j 7.08 x 10^5.

$$L(s) = \frac{\left(\frac{k_t}{\tau \cdot \xi_{rl}}\right)\left(s^2 + \frac{k_{bm}}{m_{bm}}\right)}{\left(s+\frac{1}{\tau}\right)\left(s^3 + s^2\left(\frac{k_{rl}+k_{ohc}}{\xi_{rl}}\right) + s\left(\frac{k_{bm}+k_{ohc}}{m_{bm}}\right) + \left(\frac{k_{bm}\cdot k_{ohc} + k_{bm}\cdot k_{rl} + k_{rl}\cdot k_{ohc}}{m_{bm}\cdot \xi_{rl}}\right)\right)}$$

Equation 4-14. Loop transmission with parameters for single damper model with no piezoelectric force.

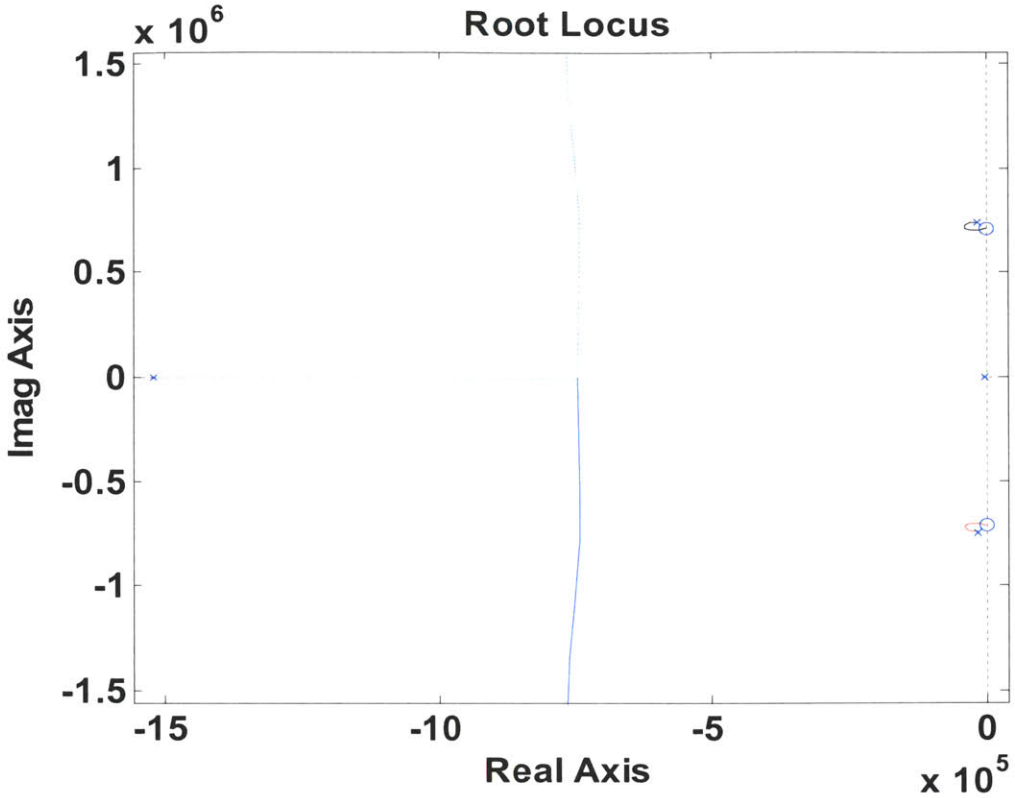

Figure 4-8. Root locus plot for single damper model with no piezoelectric force.

The system with F_{in} as the input to the output v_m, the membrane voltage, has a Bode plot which is shown in Figure 4-9. The presence of the membrane time constant causes a single pole roll-off but the presence of mechanical resonance gives a peak at higher frequencies, which may be sufficient to drive the somatic motility of the outer hair cell. The time constant has been sped up past $1/\tau$ but not significantly in this case. An examination of the pole-zero plot in Figure 4-10 demonstrates that the pole arising from the membrane time constant has moved from -3333 rad/sec to about -21.1 x 10^4 rad/sec.

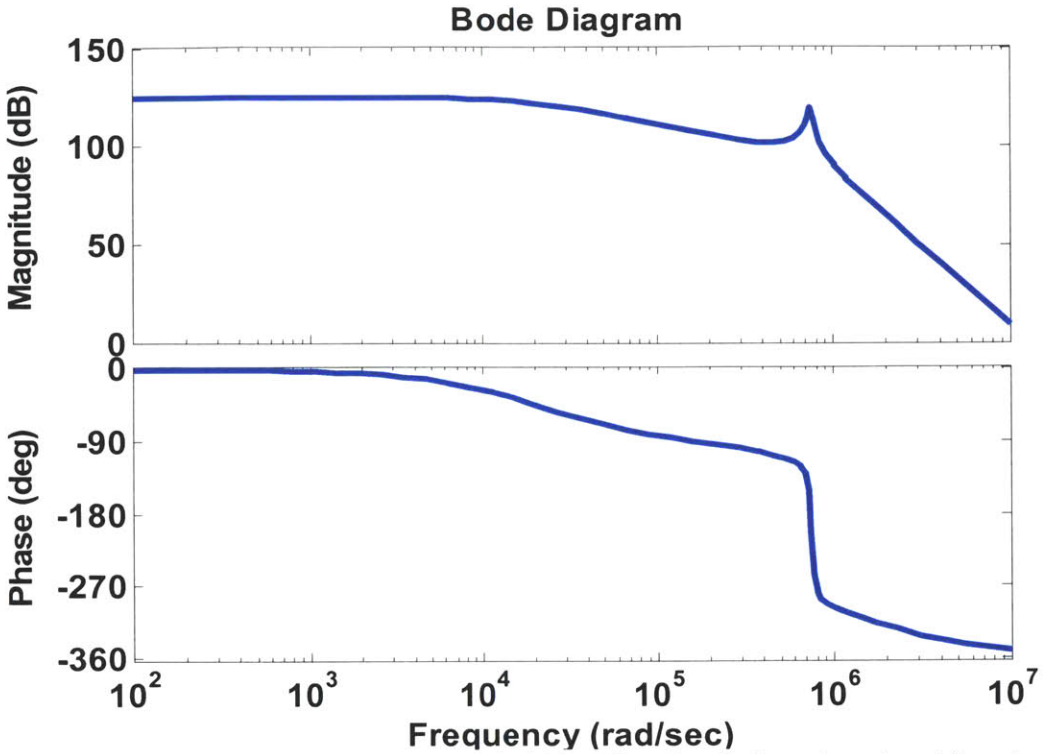

Figure 4-9. Bode plot for single damper model with no piezoelectric force from input force to output membrane voltage.

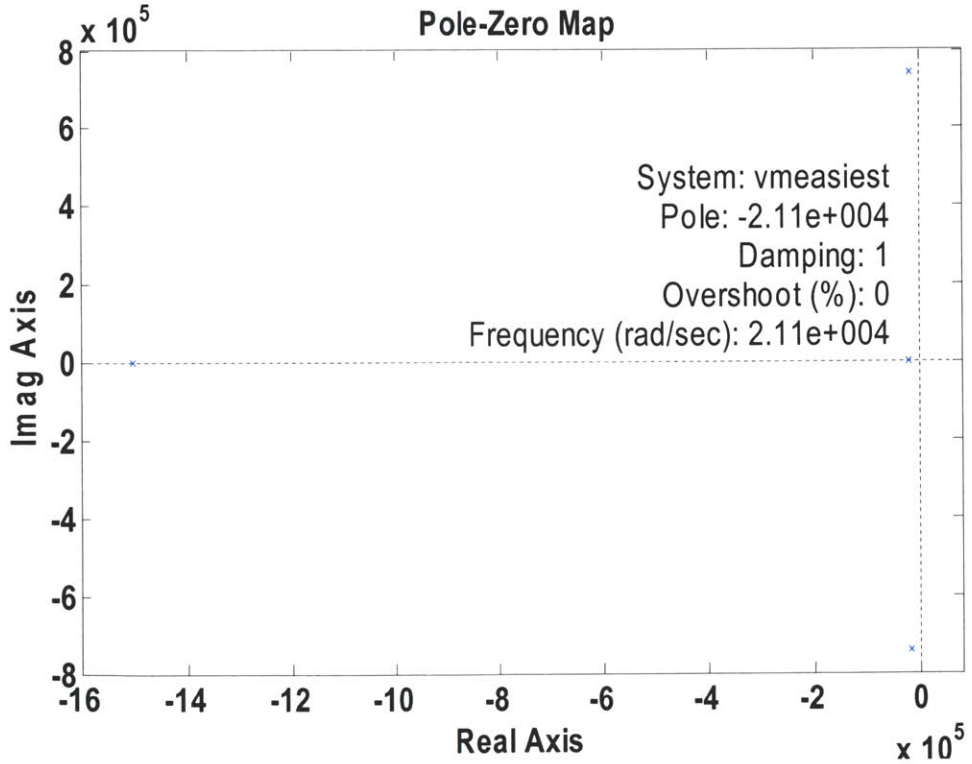

Figure 4-10. Pole-zero plot for single damper model from input force to output membrane voltage with no piezoelectric force.

Since some of the parameters obtained here were for the guinea pig and not the bat, this system may not be optimized to provide enough loop gain to push the membrane time constant out past 100 kHz. For example, if the gain of forward transduction, k_t, were increased 10-fold, the membrane time constant could be sped up 10-fold as well, to -2.11 x 10^5 rad/sec, as shown in Figure 4-11. If the membrane time constant, τ, was smaller, perhaps because bat outer hair cells are shorter than guinea pig OHCs and thus have less surface area for membrane capacitance, the speedup could be enhanced as well. For example, if τ is decreased 3-fold, as in Figure 4-12, the overall system pole resulting from the membrane time constant is sped up by approximately three times.

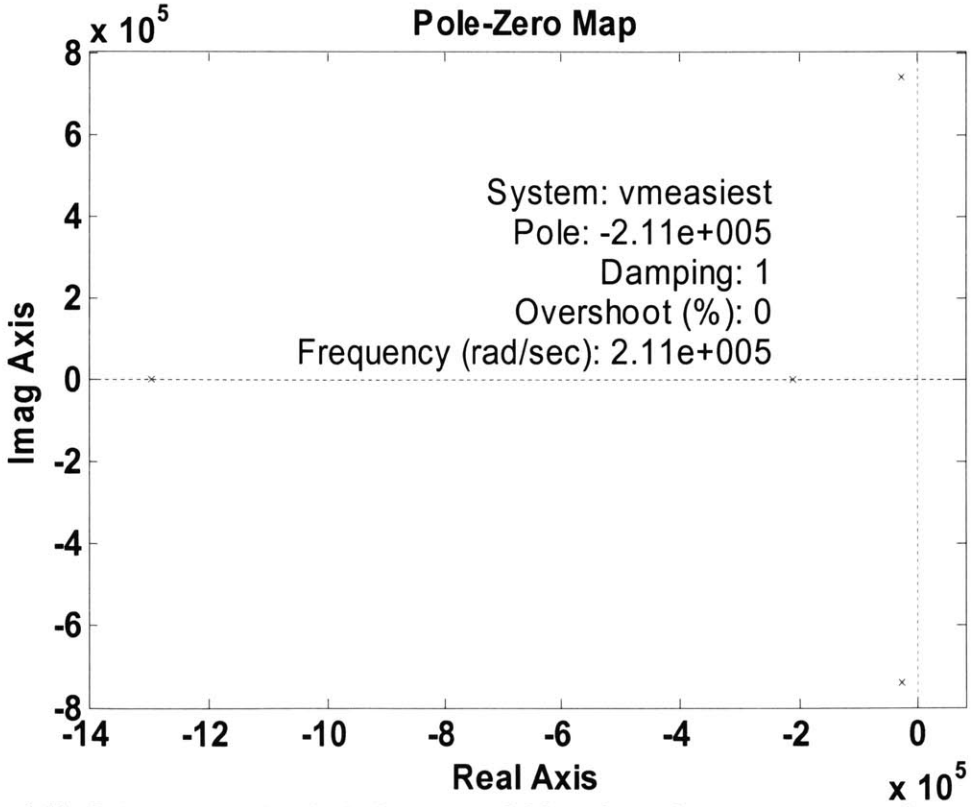

Figure 4-11. Pole-zero plot for single damper model from input force to output membrane voltage with no piezoelectric force and k_t increased 10-fold.

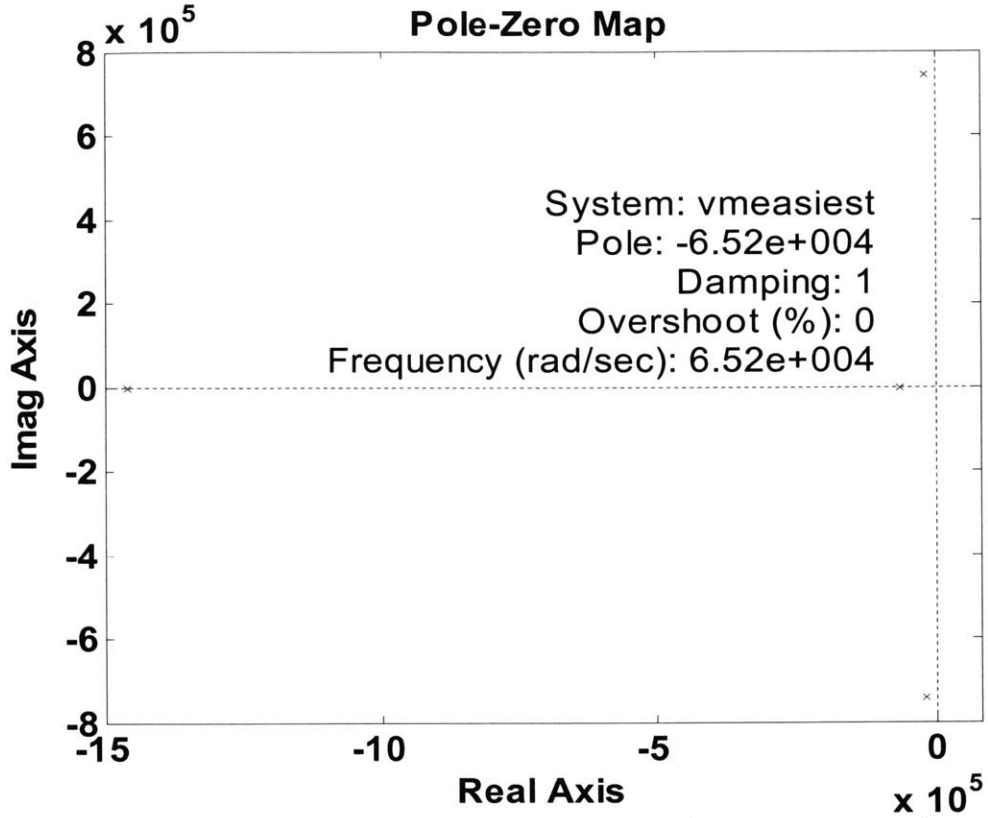

Figure 4-12. Pole-zero plot for single damper model from input force to output membrane voltage with no piezoelectric force and τ decreased 3-fold.

Thus, the negative feedback that is acting on the reticular lamina and controlling the OHC membrane voltage is able to speed up slow membrane time constants. This is due to the force feedback and the characteristics of the surrounding mechanical structures.

4.4.1.2 Model with Two Sources of Damping and No Piezoelectric Force

For the model with two sources of damping, one each on the RL and the BM, the primary effect of the extra BM damping is to shift the complex poles. The loop gain is:

$$L(s)=\frac{\left(\frac{k_t}{\tau\cdot\xi_{rl}}\right)\left(s^2+\frac{\xi_{bm}}{m_{bm}}s+\frac{k_{bm}}{m_{bm}}\right)}{\left(s+\frac{1}{\tau}\right)\left(s^3+s^2\left(\frac{m_{bm}\left(k_{rl}+k_{ohc}\right)+\xi_{rl}\cdot\xi_{bm}}{m_{bm}\cdot\xi_{rl}}\right)+s\left(\frac{\xi_{bm}\left(k_{rl}+k_{ohc}\right)+\xi_{rl}\left(k_{bm}+k_{ohc}\right)}{m_{bm}\cdot\xi_{rl}}\right)+\left(\frac{k_{bm}\cdot k_{ohc}+k_{bm}\cdot k_{rl}+k_{rl}\cdot k_{ohc}}{m_{bm}\cdot\xi_{rl}}\right)\right)}$$

Equation 4-15. Loop transmission with parameters for two damper model with no piezoelectric force.

As is shown in Figure 4-13, the zeros of the root locus plot are moved off of the jω-axis compared to the single damper system, which results in a lower Q. However, because the movement is not too great, the effect on the speedup of the slow membrane time constant is not too great either, according to Grant's rule. This is verified by the closed loop pole-zero plot in Figure 4-14, which shows that the pole due to the membrane time constant is at approximately the same location as in the single damper case.

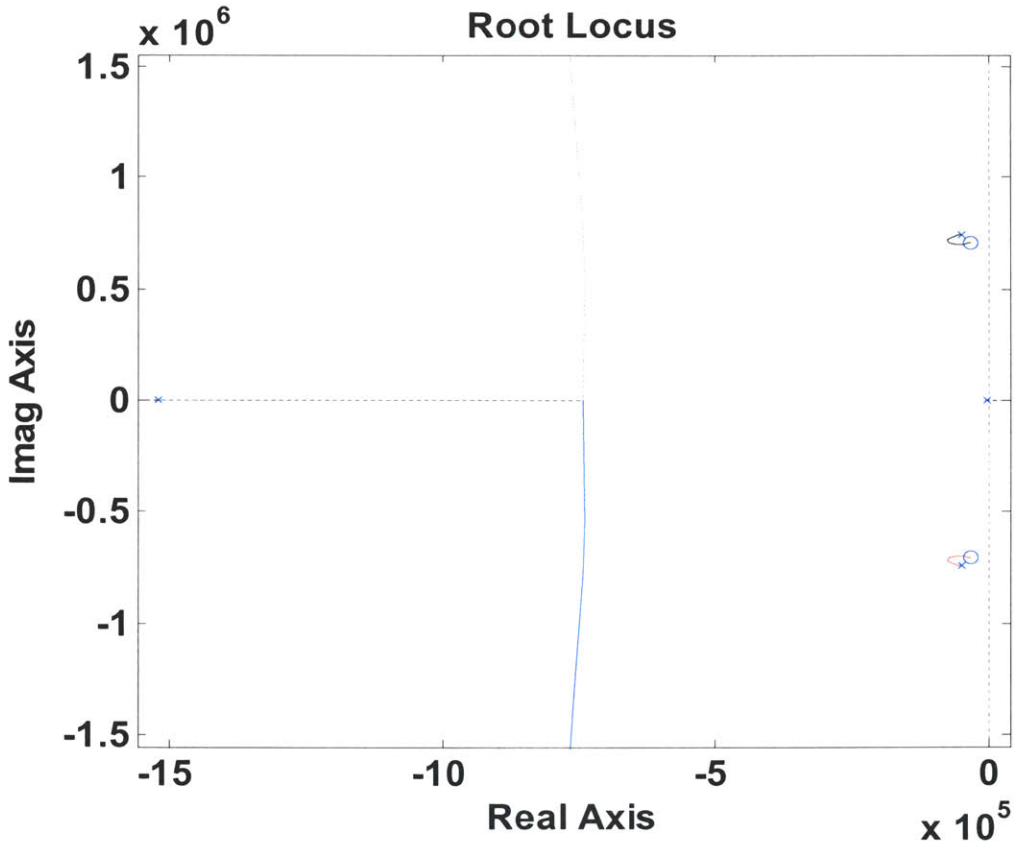

Figure 4-13. Root locus plot for two damper model with no piezoelectric force.

The Bode plot of this system, however, demonstrates that the addition of the extra damping on the basilar membrane decreases the Q of the system compared to the single damper system. This is demonstrated in Figure 4-15.

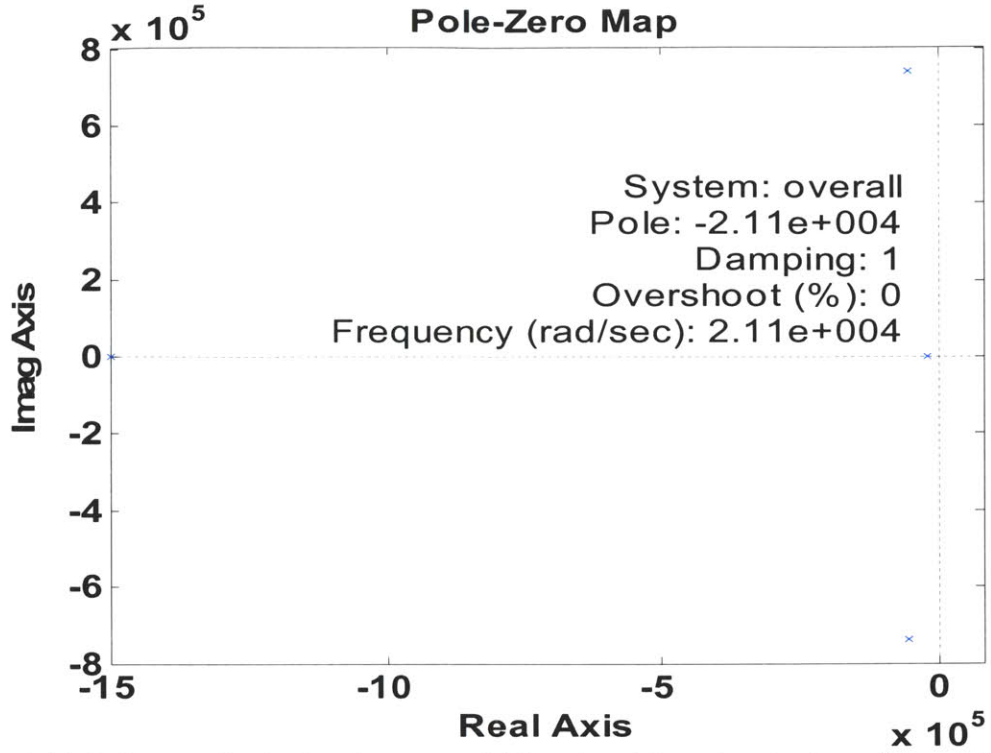

Figure 4-14. Pole-zero plot for two damper model from input force to output membrane voltage with no piezoelectric force.

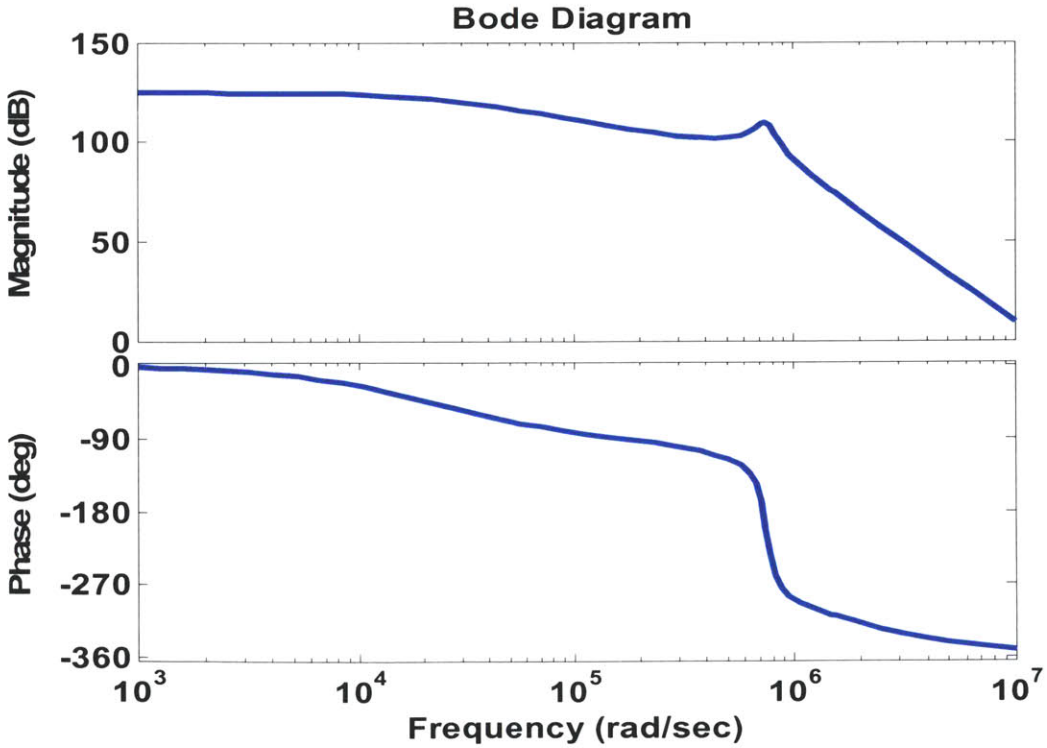

Figure 4-15. Bode plot for single damper model with no piezoelectric force from input force to output membrane voltage.

4.4.1.3 Problems with Proposed Models with No Piezoelectric Force

There are some possible problems with the two models described here. As seen in the root locus plots in Figure 4-8 and Figure 4-13, the complex zeros which the complex poles will move to are below the poles themselves. Thus, as the loop gain is increased, the poles move away from the jω-axis and downwards before they approach the zeros. This does not lead to an increased Q and identifies the need for some closer evaluation of the dynamics and interactions of the various components since the primary purpose of the cochlear amplifier is to improve the Q of the mechanical response.

Additionally, the speedup of the membrane time constant, although significant and perhaps unnecessary because of the resonance of the mechanical system, is not so great that the slow pole is pushed beyond 100 kHz. On one hand, this may be due to inaccurate parameters. On the other hand, it may be the case that the resonance of the mechanical system with the moderate speedup of the membrane time constant is enough to produce voltages for OHC somatic motility and the putative cochlear amplifier.

4.5 Revised Mechanical Model with Two Resonators

The first problem mentioned in Section 4.4.1.3 can be resolved by adding an additional mode of resonance into the system. In the previous two mechanical models, the effective mass that must be displaced when the RL moves was ignored. As we can see from the root locus plots shown above, an additional set of complex poles in the loop gain would cause the Q of the system and thus the gain at resonance to increase as k_t is increased. An additional set of poles can be added by introducing another source of resonance into the system. Suppose, as in [11], that the effective mass of the reticular lamina is approximately equal to that of the basilar membrane. The mass of the fluid in

the TM-RL gap and the TM mass may add to the effective mass of the RL in this model. Though Mammano and Ashmore [11] observed that motion of the RL was an underdamped system with the tendency to overshoot in response to a step input, the additional source of resonance being added here may not literally be only from the RL but may include the effective properties of surrounding structures. Note that Mammano and Ashmore actually state that their responses were overdamped, but the overshoot and ringing observed does not back up this claim [11]. The properties of the TM and the stereocilia may add their dynamics to the system and need to be examined in future work. Nonetheless, we model the system as shown in Figure 4-16 for the time being. Basic characteristics of two resonators coupled by a spring were presented by Dallos [24].

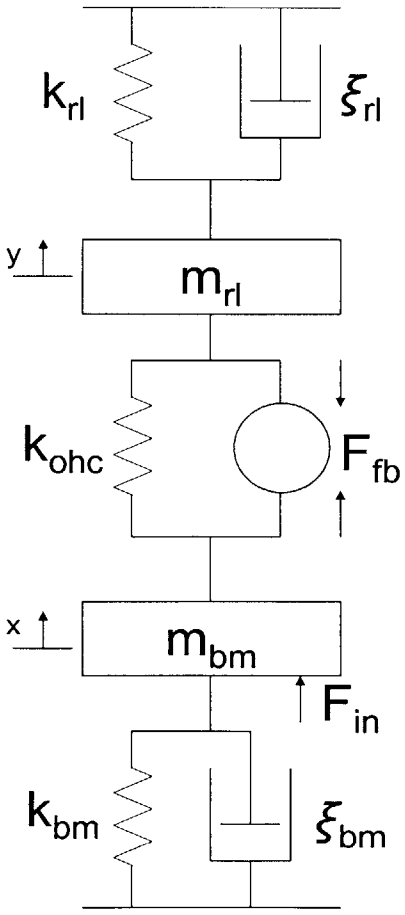

Figure 4-16. Modified mechanical model with two sources of resonance, one at the basilar membrane and the other at the reticular lamina.

We allow a new variable, m_{rl}, which is set to be equal to m_{bm}. Thus, the admittance equivalent of the reticular lamina is now given by:

$$Y_{rl} = \frac{k_{rl}}{s} + \xi_{rl} + m_{rl} \cdot s$$

Equation 4-16. Modified admittance of the reticular lamina to include an effective mass.

According to this new model, the loop gain has another pole added by the additional source of resonance. The loop transmission is expressed in Equation 4-17. Note that the gain is controlled by the value of m_{rl} in this case instead of ξ_{rl} as before.

$$\frac{\left(\frac{k_t}{\varpi m_n}\right)\left(s^2 + \frac{\xi_{bm}}{m_{bm}} s + \frac{k_{bm}}{m_{bm}}\right)}{\left(s + \frac{1}{\tau}\right)\left(s^4 + s^3\left(\frac{m_{bm}\xi_{rl} + m_{rl}\xi_{bm}}{m_{rl} \cdot m_{bm}}\right) + s^2\left(\frac{m_{rl}\left(k_{bm} + k_{dc}\right) + m_{bm}\left(k_{rl} + k_{dc}\right) + \xi_{rl}\xi_{bm}}{m_{rl} \cdot m_{bm}}\right) + s\left(\frac{\xi_{bm}\left(k_{rl} + k_{dc}\right) + \xi_{rl}\left(k_{bm} + k_{dc}\right)}{m_{rl} \cdot m_{bm}}\right) + \left(\frac{k_{bm}\left(k_{dc} + k_{rl}\right) + k_{rl}k_{dc}}{m_{rl} \cdot m_{bm}}\right)\right)}$$

Equation 4-17. Loop transmission with parameters for two modes of resonance model with no piezoelectric force.

The additional source of resonance adds another set of complex poles to the root locus diagram of the loop transmission shown in Figure 4-17. While one pair of the poles must travel to the zeroes established by the basilar membrane dynamics, the other pair of poles can travel towards the right half plane while the amplifier time constant pole moves further into the left half plane. Thus, the closed loop transfer function from the input force to the membrane voltage speeds up the amplifier time constant but at the same time increases the Q of the system, resulting in a larger gain and more selectivity. This effect is reflected in the pole-zero plot of the transfer function from input force to the membrane voltage as there are two sets of complex poles, as plotted in Figure 4-18. However, whether or not these local characteristics improve the gain and selectivity of the overall traveling wave model remains to be seen.

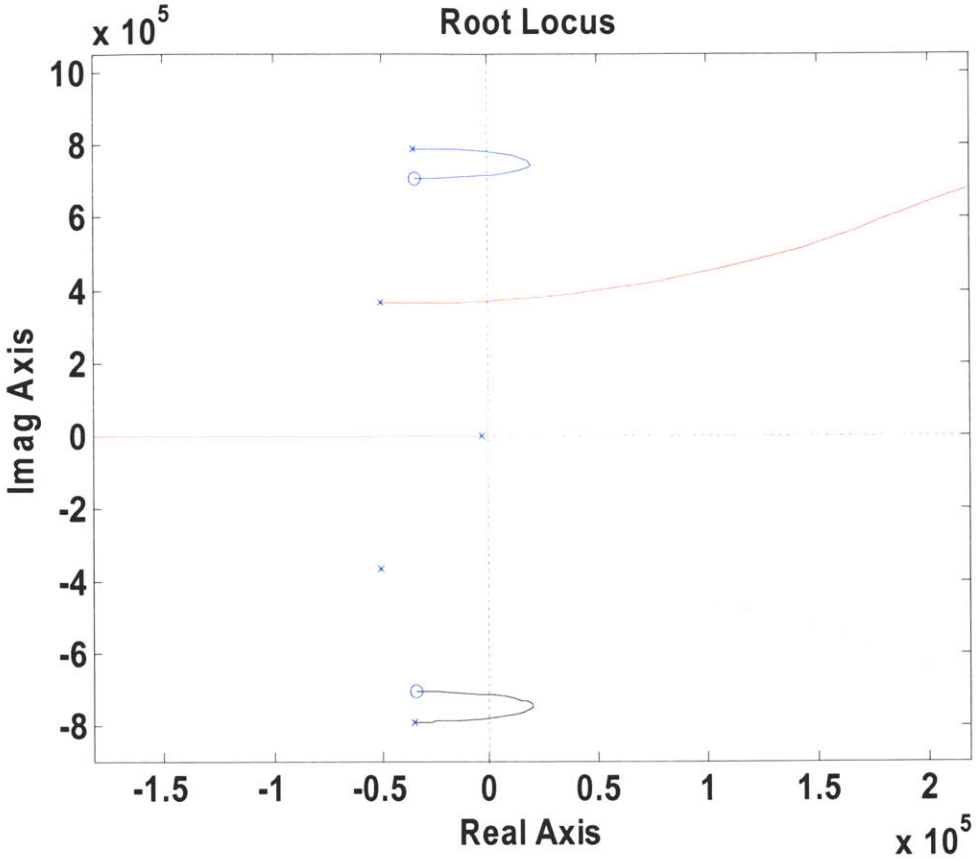

Figure 4-17. Root locus plot for two modes of resonance model with no piezoelectric force.

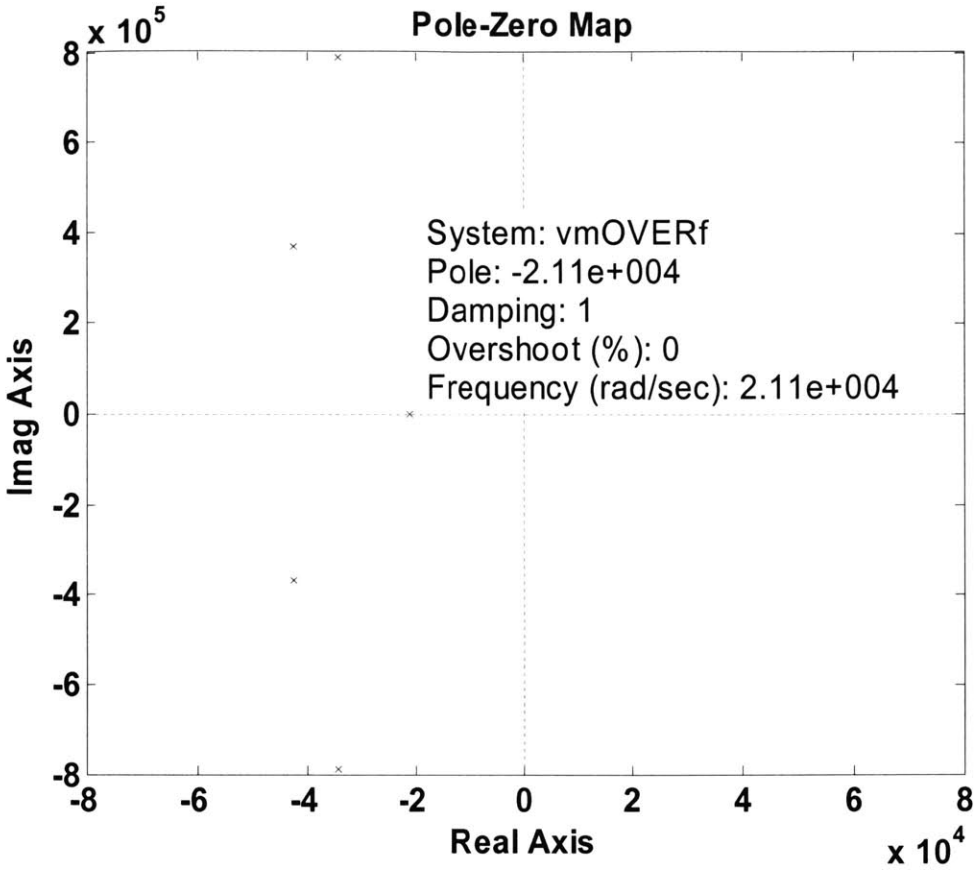

Figure 4-18. Pole-zero plot for two modes of resonance model from input force to output membrane voltage with no piezoelectric force.

The Bode plot of the membrane voltage for a given input force in Figure 4-19 also shows two peaks resulting from the two pairs of complex poles. To demonstrate how this system can result in a greater gain and speedup with larger feedback force coefficient, k_t, we artificially increase k_t to be 5 times larger than that shown in Figure 4-19 (k_t = 0.402 x 5 = 2.01). The Bode plot of the membrane voltage in this new system is shown in Figure 4-20 and clearly has a higher peak with a greater speedup of the amplifier time constant since the first order rolloff occurs at a higher frequency. If k_t is increased even further, instability may arise as the complex poles are pushed over into the right half plane. Thus, as the gain is adjusted by adaptation mechanisms in the cochlea, the characteristics of the

local feedback model are modified as well. The effect of changes in the local model on the overall traveling-wave response of the cochlea will be discussed in later work.

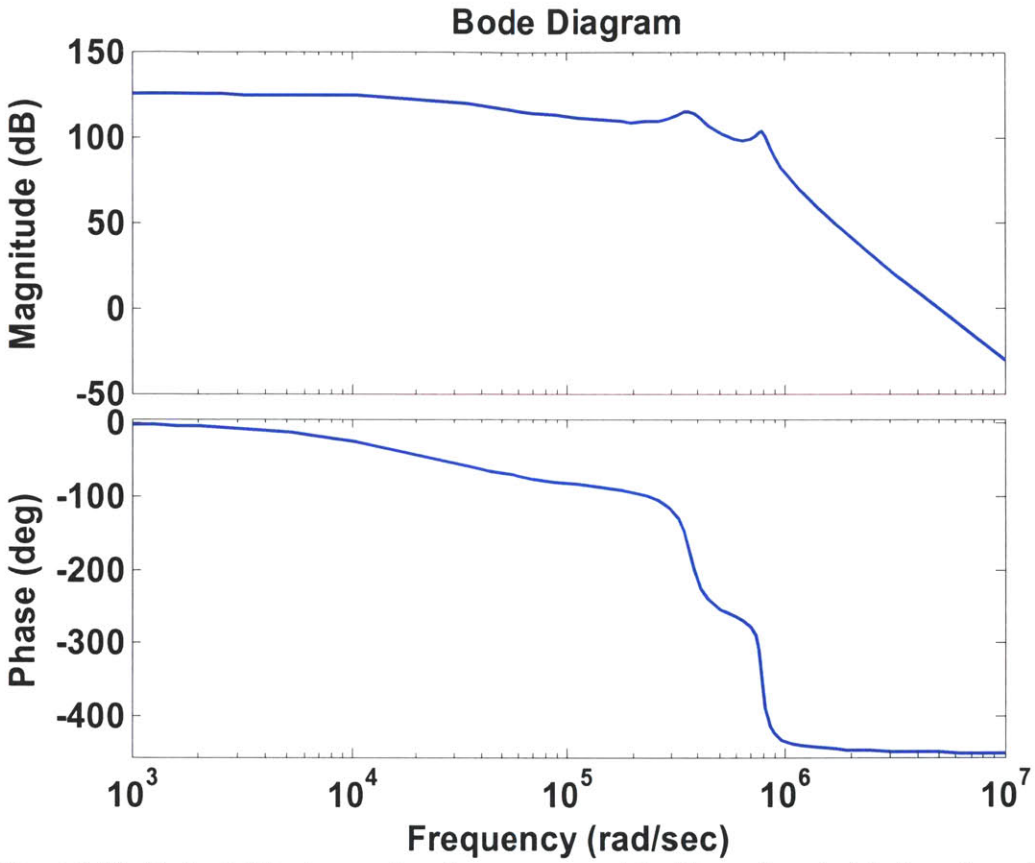

Figure 4-19. Bode plot for two modes of resonance model with no piezoelectric force from input force to output membrane voltage.

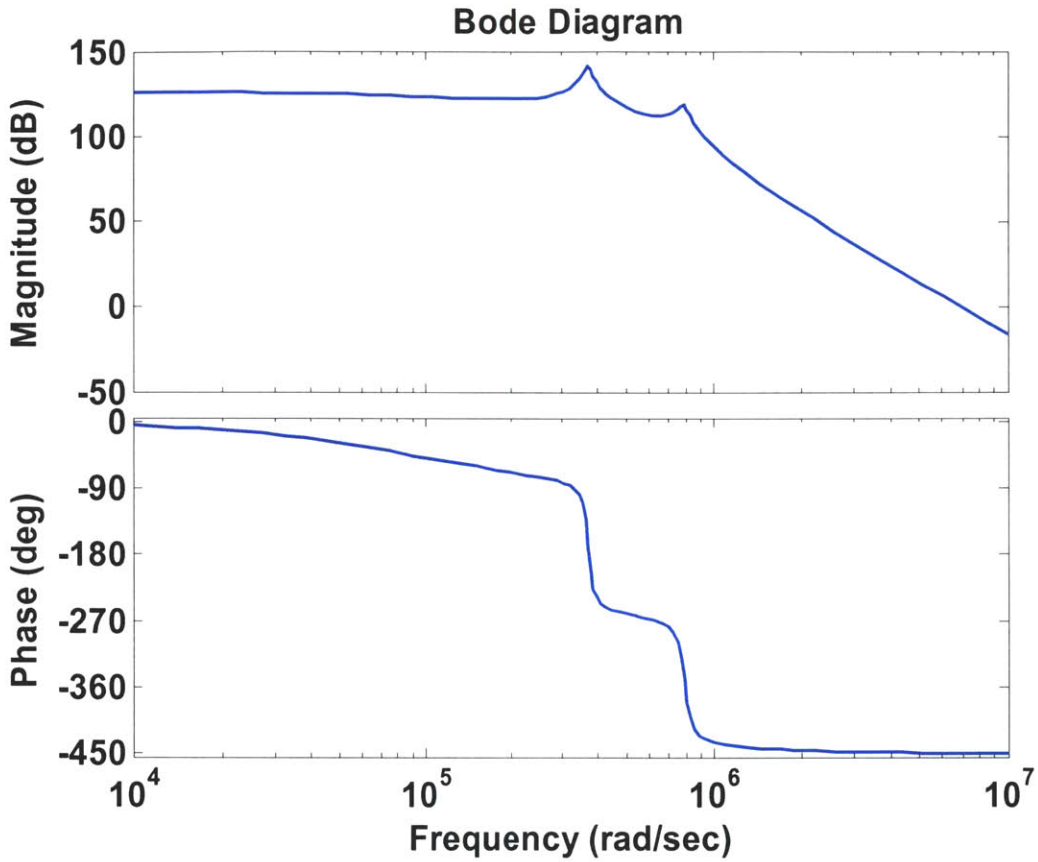

Figure 4-20. Bode plot for two modes of resonance model with no piezoelectric force from input force to output membrane voltage using $k_t = 2.01$.

4.5.1 Possible Mechanism for Spontaneous Otoacoustic Emissions

The ability of this system to produce instability in the membrane voltage of the outer hair cell with increased OHC gain could lead to oscillations that may be the basis of observed spontaneous otoacoustic emissions [6]. Spontaneous otoacoustic emissions are observed in the absence of any external stimulation. In order to enhance sensitivity and selectivity for very soft sounds in times of silence or low sound input levels, it is likely that outer hair cell gain is increased in the biological cochlea. This would cause the complex poles shown in the root locus plot of Figure 4-18 to move closer and closer to the jω-axis and perhaps cross it in certain cases, leading to instability and spontaneous

emissions. Concomitant with this possible mechanism of spontaneous otoacoustic emissions is the fact that aspirin is known to reduce the force produced by outer hair cells and also reduce the production of spontaneous otoacoustic emissions [29][30]. Further study that incorporates known physiological conditions that can trigger spontaneous otoacoustic emissions with a full traveling-wave model that includes the local model described here and nonlinearities is necessary to confirm or refute the possible connection between outer hair cell instability and observed spontaneous otoacoustic emissions. For example, in addition to reducing the magnitude of spontaneous otoacoustic emissions, aspirin may also cause small shifts in the frequency of these emissions [31].

4.5.2 Basilar Membrane Response

The block diagram in Figure 4-7 yields a transfer function from input force to reticular lamina velocity. To prepare the local model for incorporation into a traveling-wave model, we use the free-body equation expressed in Equation 4-18 to derive the block diagram shown in Figure 4-21. Essentially, the conversion from the reticular lamina velocity to basilar membrane displacement introduces two poles, one at the origin and one at $-1/\tau$, as well as three zeros governed by the reticular lamina and OHC mechanical characteristics and the OHC amplifier gain. The two poles introduced by the conversion cancel out with the zeros at the origin and at $-1/\tau$ that show up in the transfer function from input force to RL velocity. As seen in Figure 4-22, one of the zeros added by the conversion falls quite close to the sped up amplifier time constant, providing a near pole-zero cancellation. This reduces the effect of the amplifier time constant on the basilar membrane and solves the second problem in Section 4.4.1.3. The two other zeros are complex and are in the vicinity of the complex poles generated by the feedback loop.

$$0 = k_{rl} \cdot y + \xi_{rl} \cdot \dot{y} + m_{rl} \cdot \ddot{y} + k_{ohc}(y - x) + \frac{k_t}{\tau s + 1} \cdot y$$

Equation 4-18. Free-body equation for two sources of resonance model with no piezoelectric force.

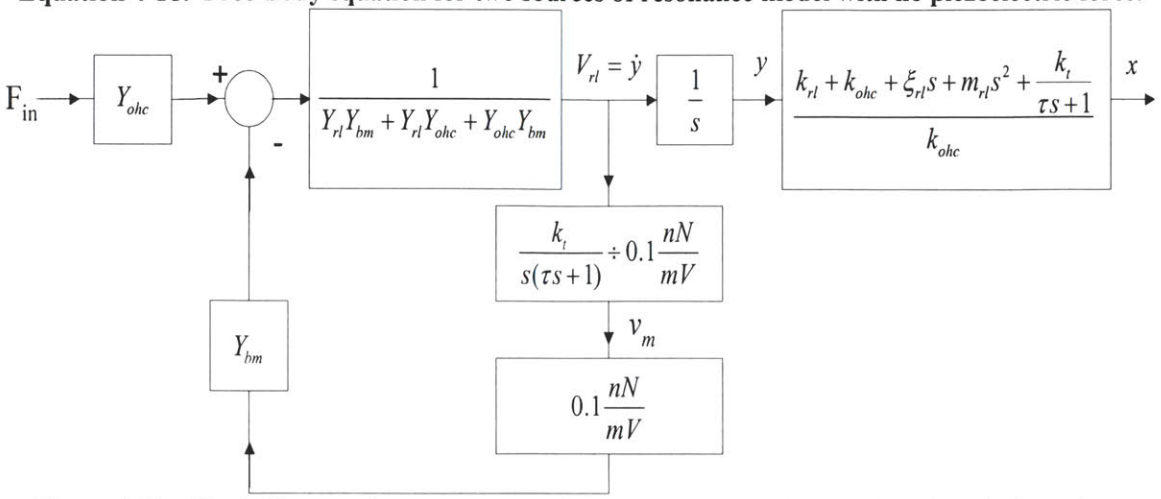

Figure 4-21. Block diagram for two sources of resonance model with no piezoelectric force from input force to basilar membrane displacement, x.

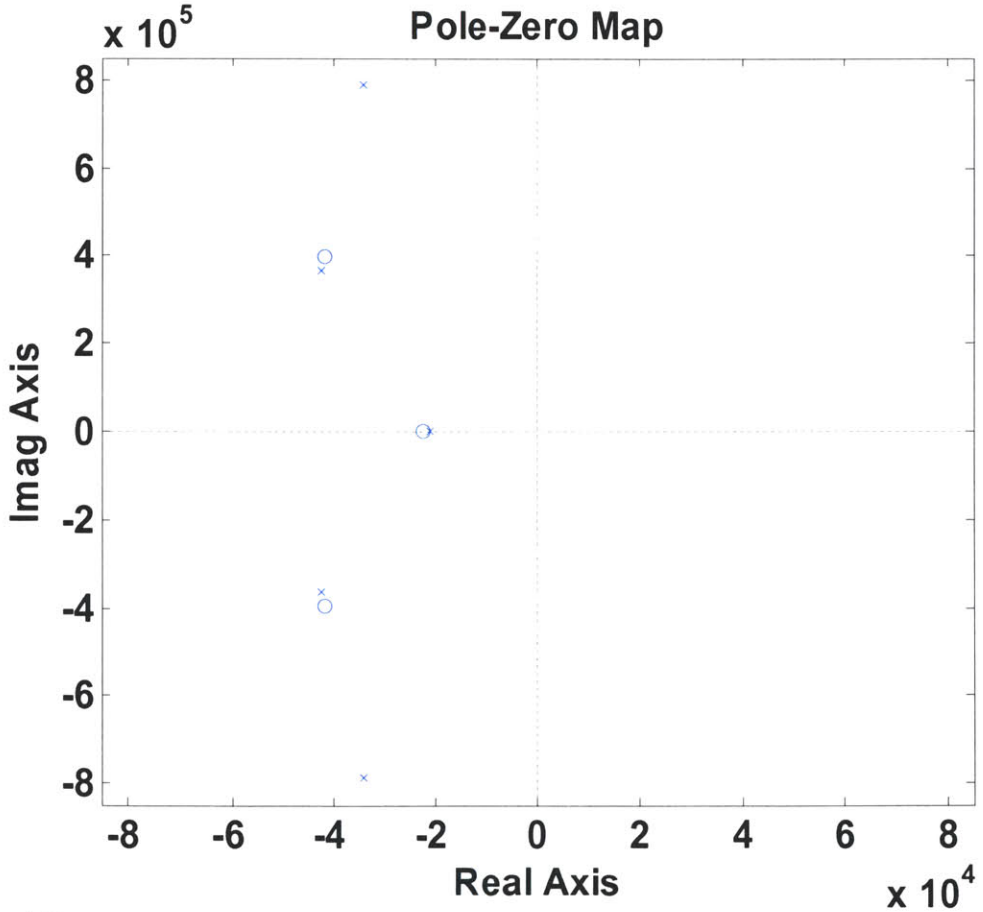

Figure 4-22. Pole-zero plot of two sources of resonance model with no piezoelectric force from input force to basilar membrane displacement. Note the many near pole-zero cancellations.

The Bode plot of this system in Figure 4-23 has a peak that is probably too sharp to be realistic. However, as expected, the effect of the amplifier time constant is minimal because of the pole-zero cancellation. The first peak results from the near pole-zero cancellation of the complex poles and complex zeros closer to the origin. The second peak results from the complex poles farther from the origin.

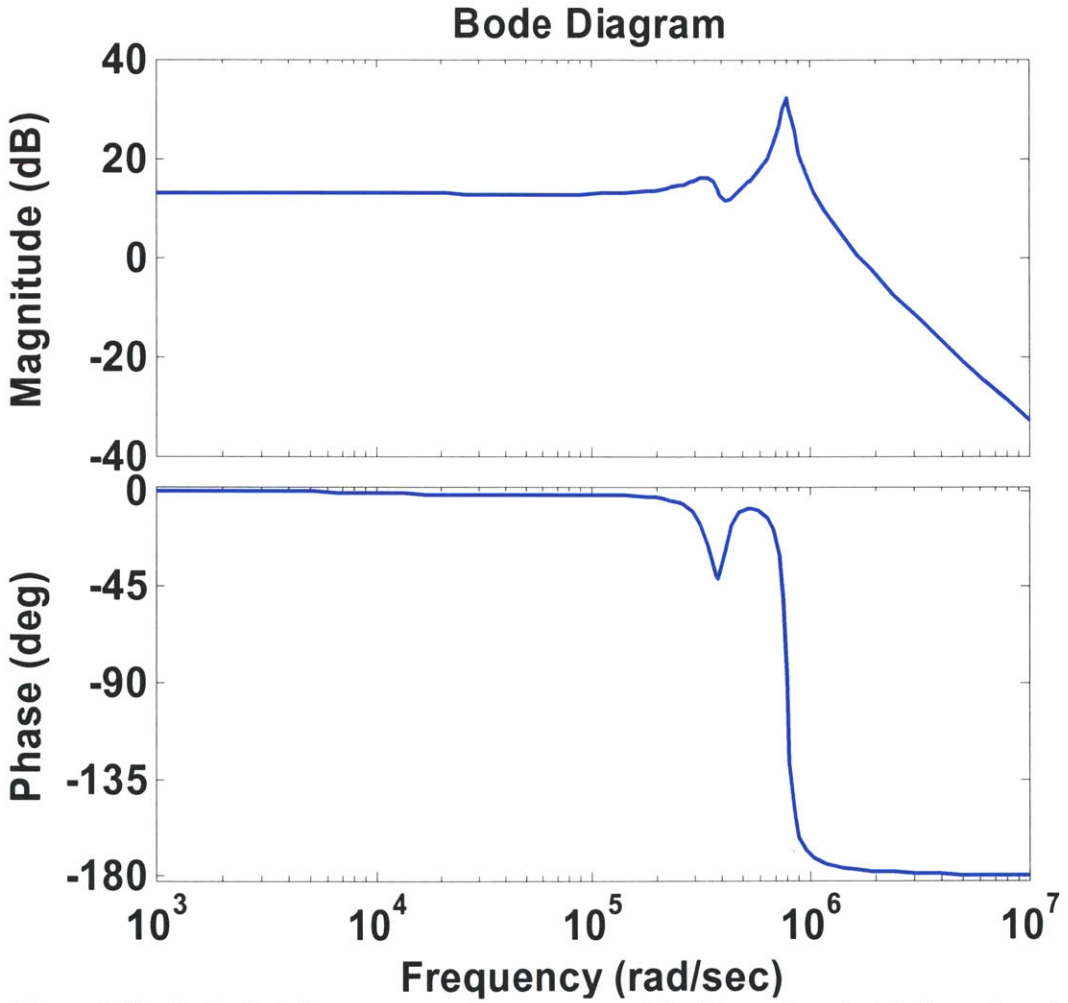

Figure 4-23. Bode plot of two sources of resonance model with no piezoelectric force from input force to basilar membrane displacement.
The second peak is probably too sharp to be realistic.

The second peak can be minimized by increasing the damping of the basilar membrane. Increasing ξ_{bm} by an order of magnitude to 3.033 x 10^{-7} N·s/m, the resulting

Bode diagram in Figure 4-24 shows a much more highly damped system. Increasing the value of the OHC gain sharpens the first peak but does not affect the second peak greatly as seen in Figure 4-25. This is expected because the second peak results from the complex poles further away from the origin, which, from the root locus plot in Figure 4-17, do not move to a great extent compared with the complex poles closer to the origin.

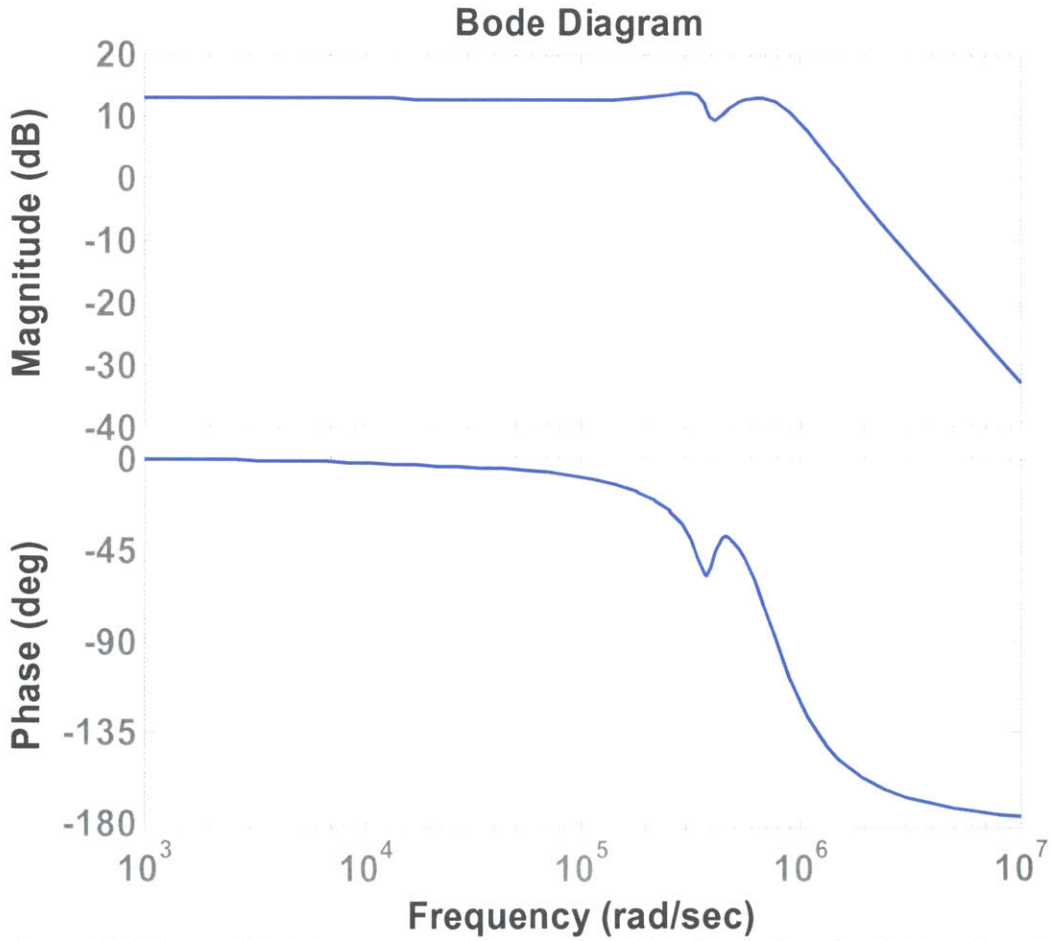

Figure 4-24. Bode plot of two sources of resonance model with no piezoelectric force from input force to basilar membrane displacement where basilar membrane damping, $\xi_{bm} = 3.033 \times 10^{-7}$ N·s/m.

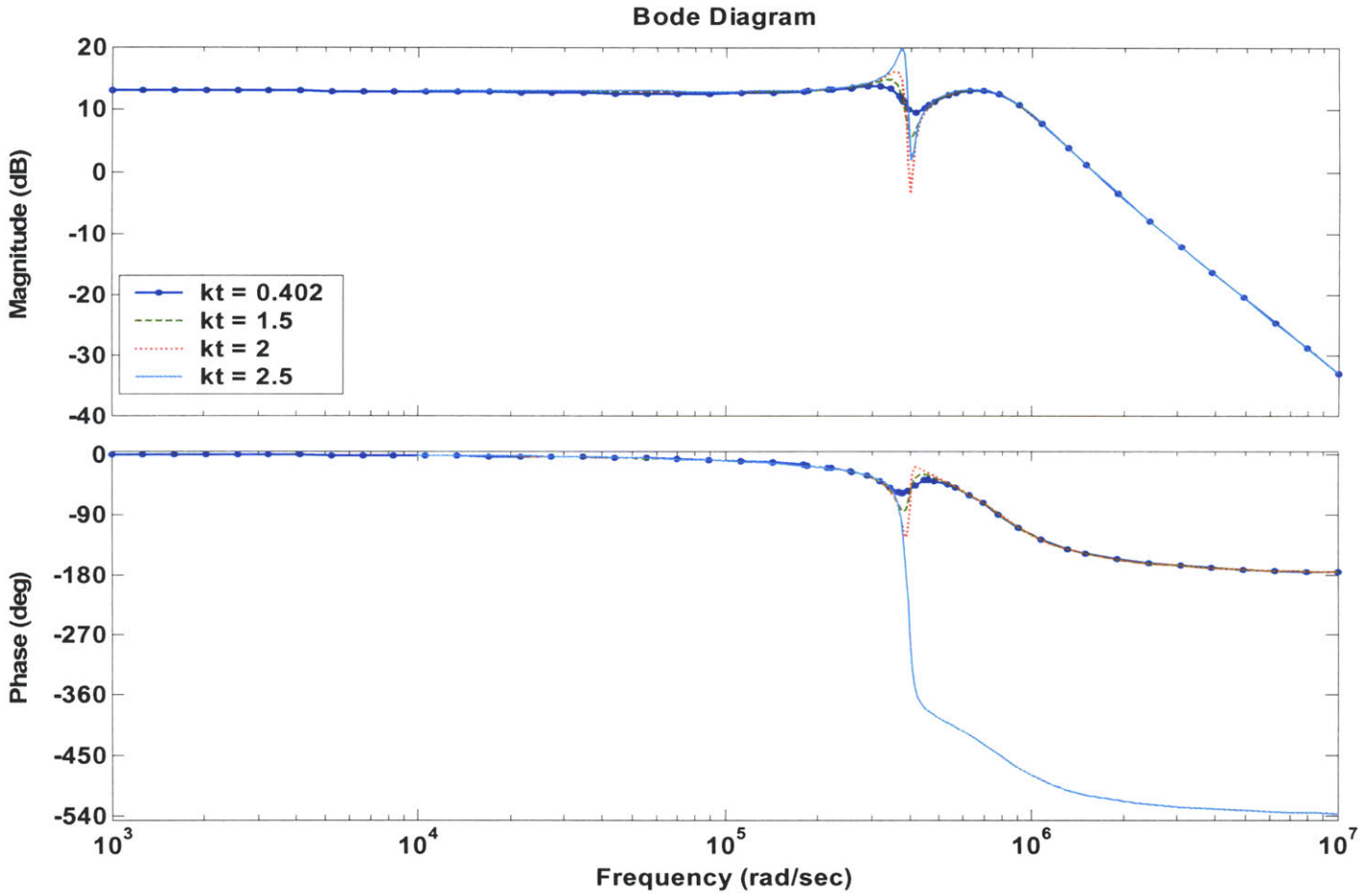

Figure 4-25. Bode plot of two sources of resonance model with no piezoelectric force from input force to basilar membrane displacement where ξ_{bm} = 3.033 x 10^{-7} N·s/m. Different gain settings are shown.
At large values of k_t, such as k_t = 2.5 N/m, the phase nature of the system changes dramatically.

As the OHC gain, k_t, is increased, the first peak increases in magnitude and also becomes sharper while the second peak barely changes. After a certain value of k_t, the phase of the system changes dramatically, as shown by the k_t = 2.5 N/m case in Figure 4-25. The phase change results because the complex zeros introduced by the conversion block from the reticular lamina velocity to basilar membrane displacement move further to the right for larger values of k_t and eventually cross over into the right half plane. The pole-zero diagram in Figure 4-26 demonstrates this effect for different OHC gain settings.

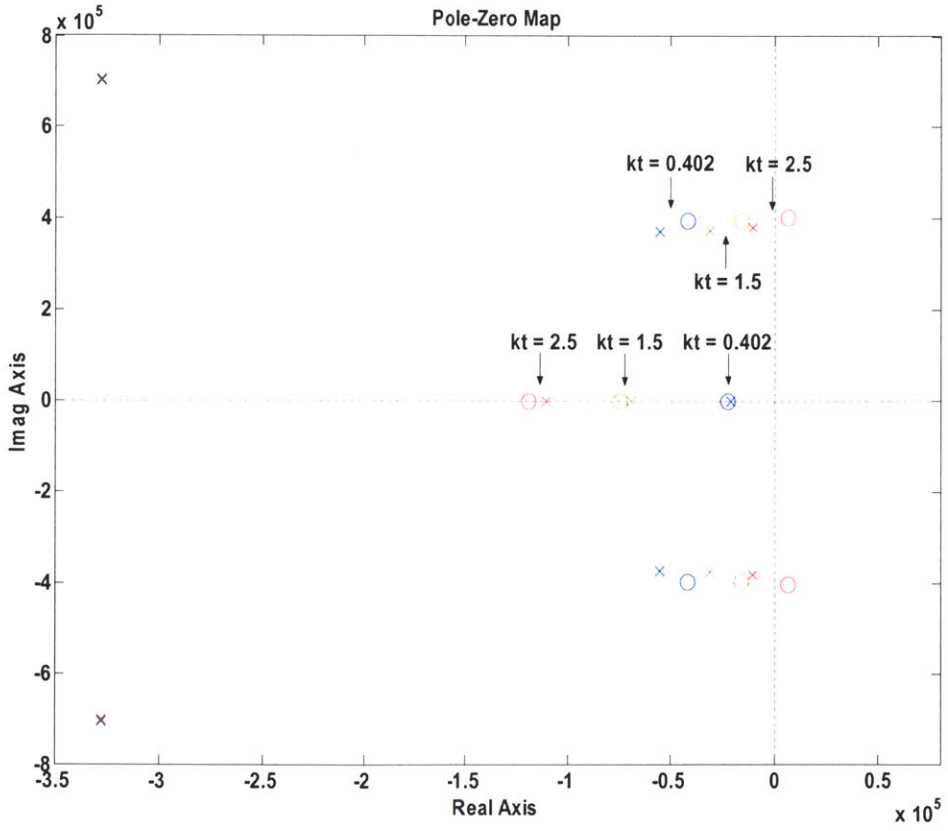

Figure 4-26. Pole-zero plot of two sources of resonance model with no piezoelectric force from input force to basilar membrane displacement where ξ_{bm} = 3.033 x 10^{-7} N·s/m. Different gain settings are shown, although k_t = 2.0 N/m is omitted for clarity. At large values of k_t, right half plane zeros result.

The responses of BM displacement to a step input force for the three gain settings in Figure 4-26 are shown in Figure 4-27 and zoomed in for clarity in Figure 4-28.

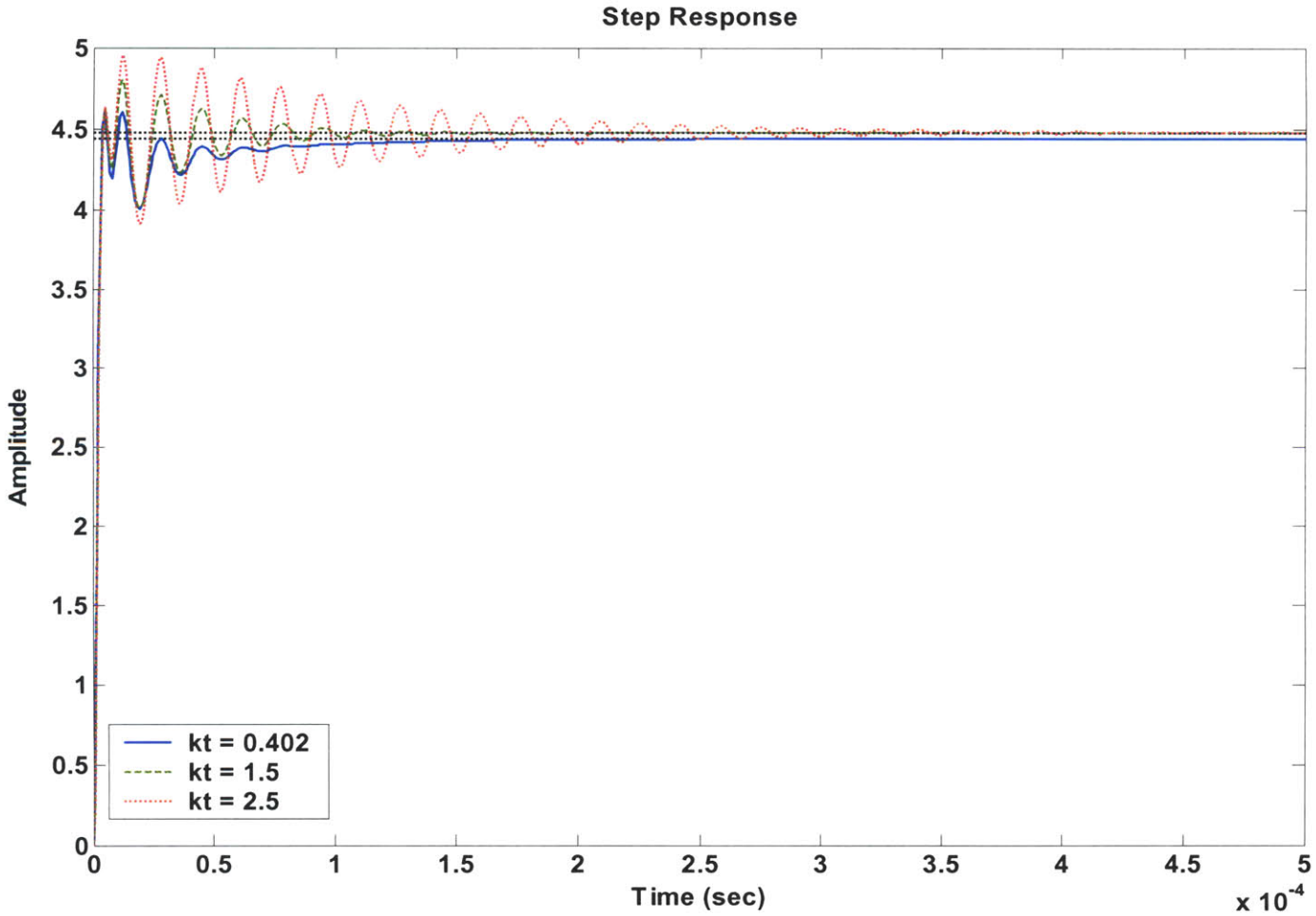

Figure 4-27. Step response of BM displacement for two sources of resonance model with no piezoelectric force where ξ_{bm} = 3.033 x 10^{-7} N·s/m.

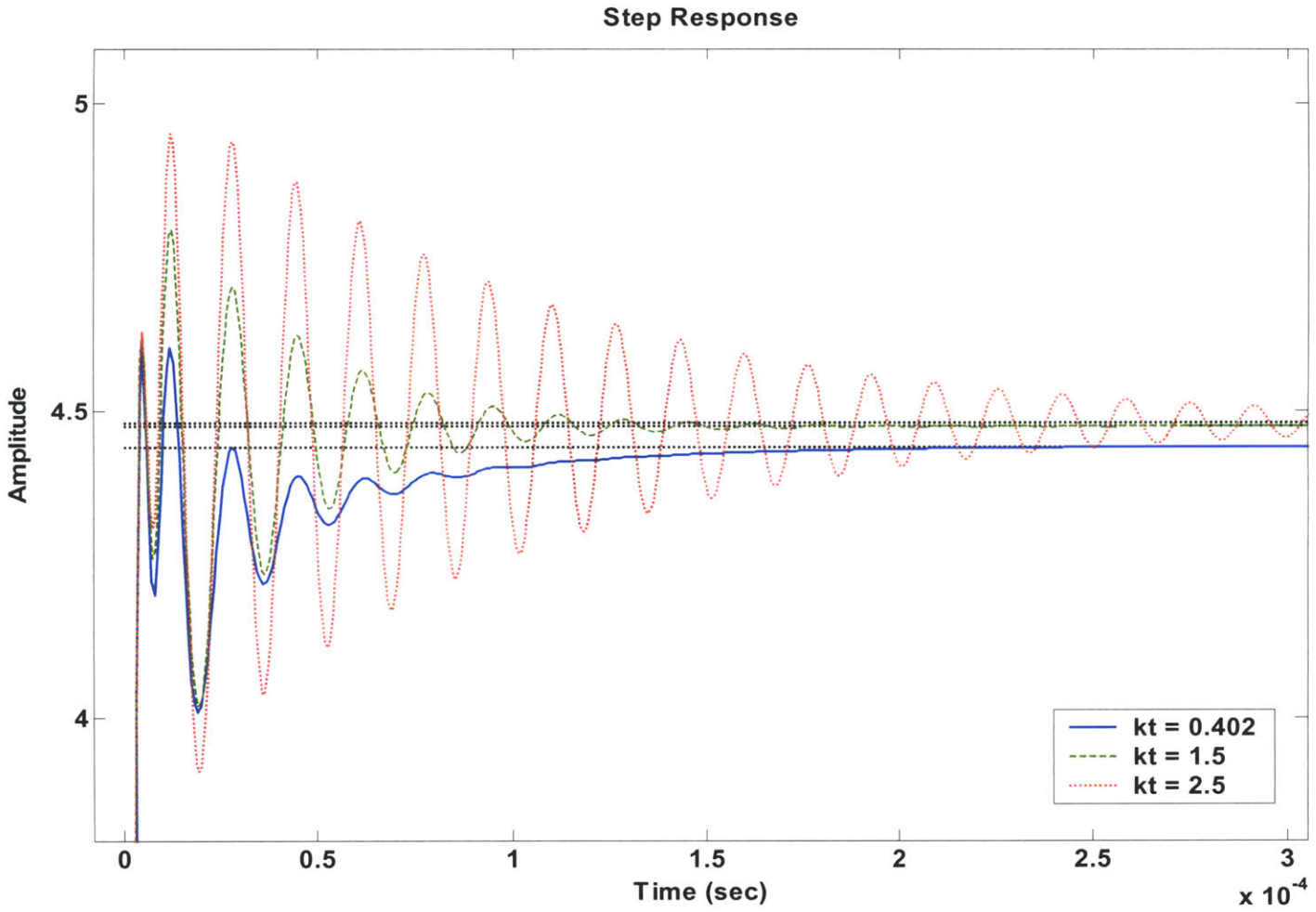

Figure 4-28. Zoomed step response of BM displacement for two sources of resonance model with no piezoelectric force where $\xi_{bm} = 3.033 \times 10^{-7}$ N·s/m.

As the step responses and Bode plots demonstrate, increased OHC gain results in a larger and sharper first peak. This translates into a slower settling time for a step response input and more ringing. The second peak comes later in frequency and is not largely affected by changes in OHC gain. Nonetheless, there is increased selectivity and gain at the first peak as the Q rises with higher values of OHC gain.

4.5.3 Analysis of Different Regimes using the Electrical Analog

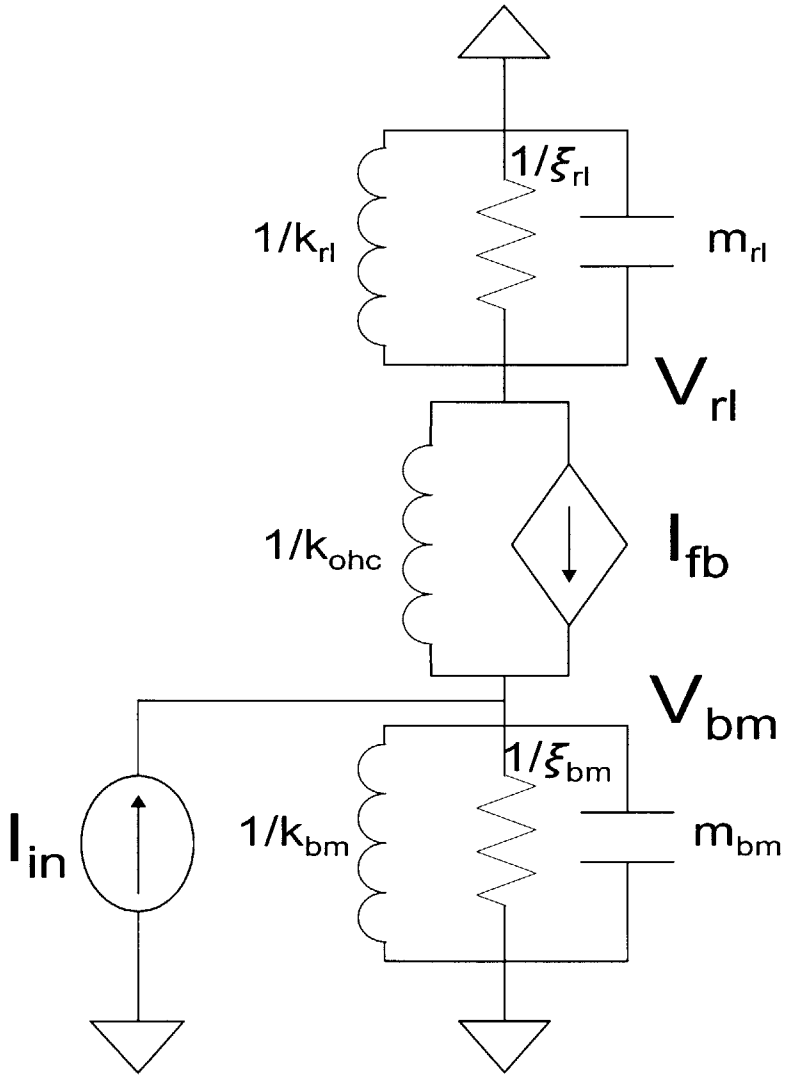

Figure 4-29. Electrical analog of the two resonator model with currents representing forces and voltages representing velocities. Same as Figure 1-1.

Figure 4-29 is the electrical analog of the two resonator model adopting the convention that currents are forces and voltages are velocities. Thus, inductors represent compliance, conductances are in analogy to damping, and capacitors are masses.

Around the first peak in the basilar membrane response, the reticular lamina is operating around resonance. Thus, the reticular lamina impedance is essentially a resistor. Since the peak frequency of the basilar membrane LRC tank is greater than that of the reticular lamina, the basilar membrane impedance around the first peak is dominated by the BM inductor (stiffness). We can model the resulting system as shown in Figure 4-30.

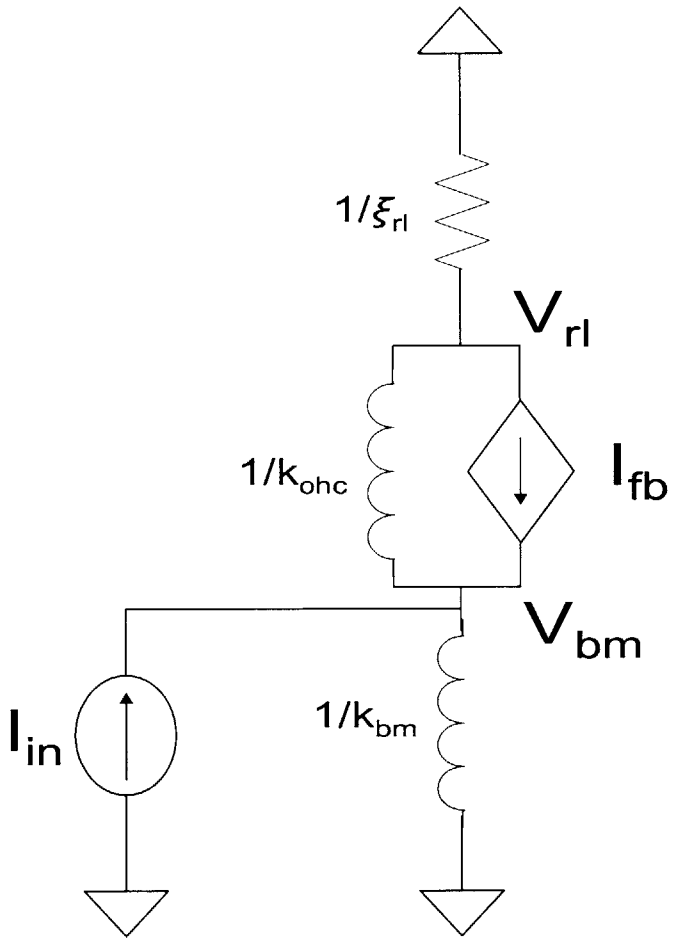

Figure 4-30. The electrical analog of the two resonator model operating around the first resonant peak in the BM response where the RL is damping dominated and the BM is stiffness dominated.

In this regime, the effective combined impedance of the reticular lamina and outer hair cell has a capacitive (mass) component added to it by the outer hair cell gain. Since $I_{fb} = k_t/(s\cdot(\tau s+1))$ and at the first peak in the BM response the system is operating far beyond $\omega = -1/\tau$, we can approximate I_{fb} as $k_t/(s^2\tau)$. The effective impedance of the RL and OHC combined, looking in from the basilar membrane, can be found by applying an input current and finding the resulting voltage as shown in Figure 4-31. Since all the incoming current, I_t, must pass through the resistor, v_{rl} is simply I_t/ξ_{rl} or I_tR. Writing KCL around the input node,

$$I_t + I_{fb} = \frac{v_t - v_{rl}}{Ls}$$

Equation 4-19. KCL around the input node of the test current in Figure 4-31.

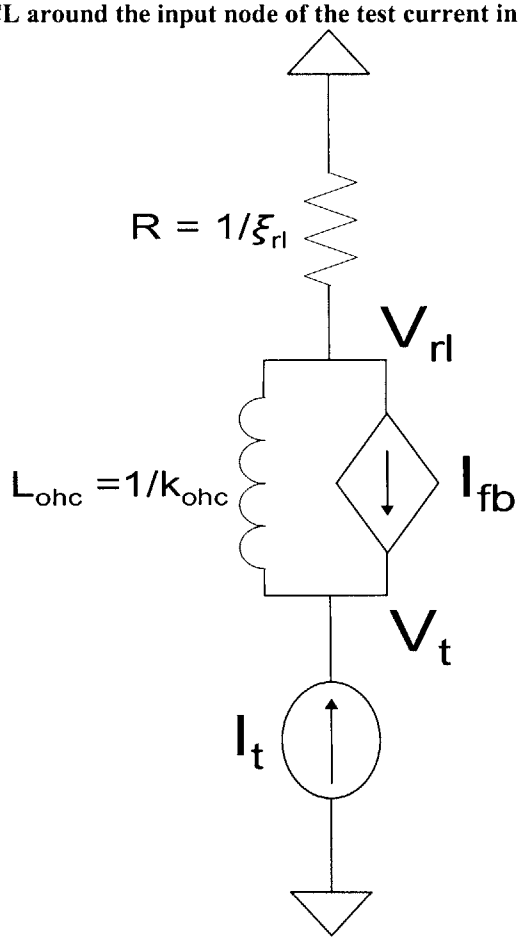

Figure 4-31. Finding the effective combined impedance of the OHC and RL looking in from the BM around the first resonant peak in the BM transfer function by using the electrical analog of the two resonator model.

As a result of Equation 4-19, $I_t \cdot (L_{ohc} \cdot s + R + L_{ohc} \cdot k_t \cdot R/\tau s) = v_t$, which implies that the effective impedance Z_{or} of the OHC and RL combined is given by Equation 4-20.

$$Z_{or} = \frac{v_t}{I_t} = L_{ohc}s + R + \frac{L_{ohc}Rk_t}{\tau s}$$

Equation 4-20. Effective impedance of the OHC and RL around the first BM peak has a capacitive (mass) component added to it due to the OHC gain.

Z_{or} is an LRC circuit in series and is in parallel with the basilar membrane inductor from the point of view of the input current (force). The introduction of a capacitor into the system allows the opportunity for resonance and can explain the sharpening of the first peak with increased OHC gain. The input impedance of the entire circuit is given by $Z_{bm} \parallel Z_{or}$:

$$Z_{bm} \parallel Z_{or} = \frac{\left(\frac{\tau}{Rk_t}s^2 + \frac{\tau}{L_{ohc}k_t}s + 1\right)L_{bm}s}{\frac{\tau}{Rk_t}\left(1 + \frac{L_{bm}}{L_{ohc}}\right)s^2 + \frac{\tau}{L_{ohc}k_t}s + 1}$$

Equation 4-21. Input impedance around the first BM peak has complex poles and zeroes.

This form of the input impedance explains a great deal of the behavior around the first basilar membrane peak. Let us examine the denominator of the input impedance first, which imposes a peaking behavior in the current to voltage response. The second term in the denominator represents the damping. Thus, an increased k_t will cause a greater peak, as was observed in Figure 4-25. Similarly, a faster OHC time constant (lower τ) increases the Q of the system. The first term in the denominator basically sets the resonant frequency. Increased OHC gain pushes the resonant frequency further out, which is also seen in Figure 4-25 as the peak shifts to a higher frequency with larger k_t. The numerator sets the dip that occurs after the first resonant peak in the basilar membrane response due to the effect of the complex zeros. Because the first term in the

numerator (τ/Rk_t) is less than the first term in the denominator by ($1+L_{bm}/L_{ohc}$), the dip occurs at a higher frequency than the peak, concomitant with the behavior in Figure 4-25. The dip also becomes sharper with increased OHC gain, leading to a greater rolloff. Therefore, the basic effect of the OHC gain around the first peak of the BM transfer function is to produce an effective capacitance in the combined OHC and RL impedance so that a resonant peak and dip are created. Larger k_t leads to sharpened responses at higher frequencies by lowering the effective capacitance (mass) created by the OHC gain because $C \sim 1/k_t$ in Equation 4-20.

If the OHC gain did not exist, the input impedance would be given by Equation 4-22 and would exhibit no peaking behavior, as expected.

$$Z_{bm} \| Z_{or} = \frac{(L_{ohc}s + R)L_{bm}s}{(L_{ohc} + L_{bm})s + R}$$

Equation 4-22. The input impedance with no OHC gain exhibits no peaking behaviors.

4.5.4 Reticular Lamina Response

The reticular lamina is also modified by increasing OHC gain. Unlike the basilar membrane response, however, the low frequency value of the reticular lamina displacement to input force transfer function decreases with larger gain. As expected, the peaking behavior of the reticular lamina transfer function sharpens with a higher gain value, as shown in Figure 4-32 where ξ_{bm} was increased to 3.033×10^{-7} N·s/m.

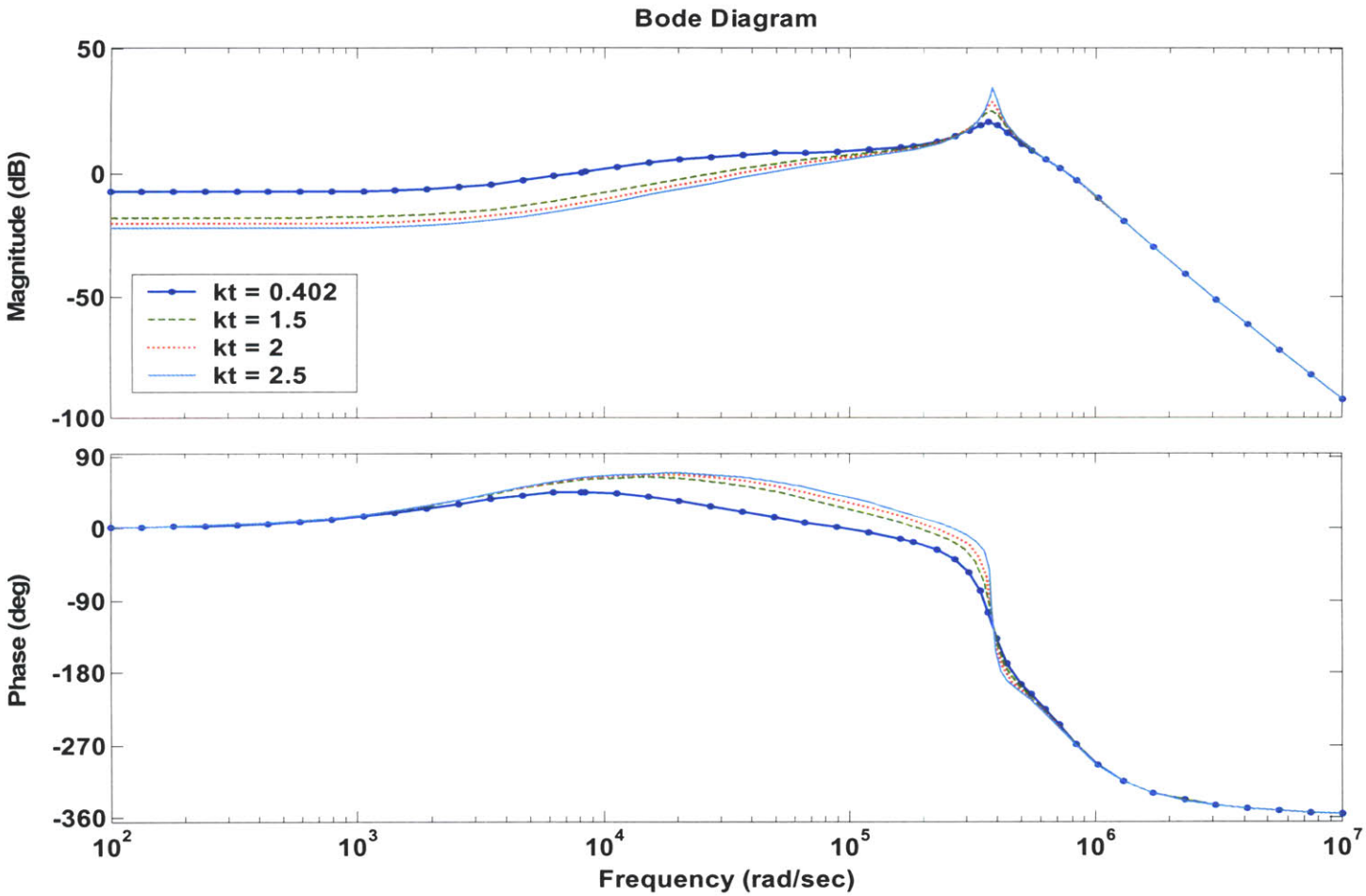

Figure 4-32. Bode plot of two sources of resonance model with no piezoelectric force from input force to reticular lamina displacement where ξ_{bm} = 3.033 x 10^{-7} N·s/m. Different gain settings are shown.

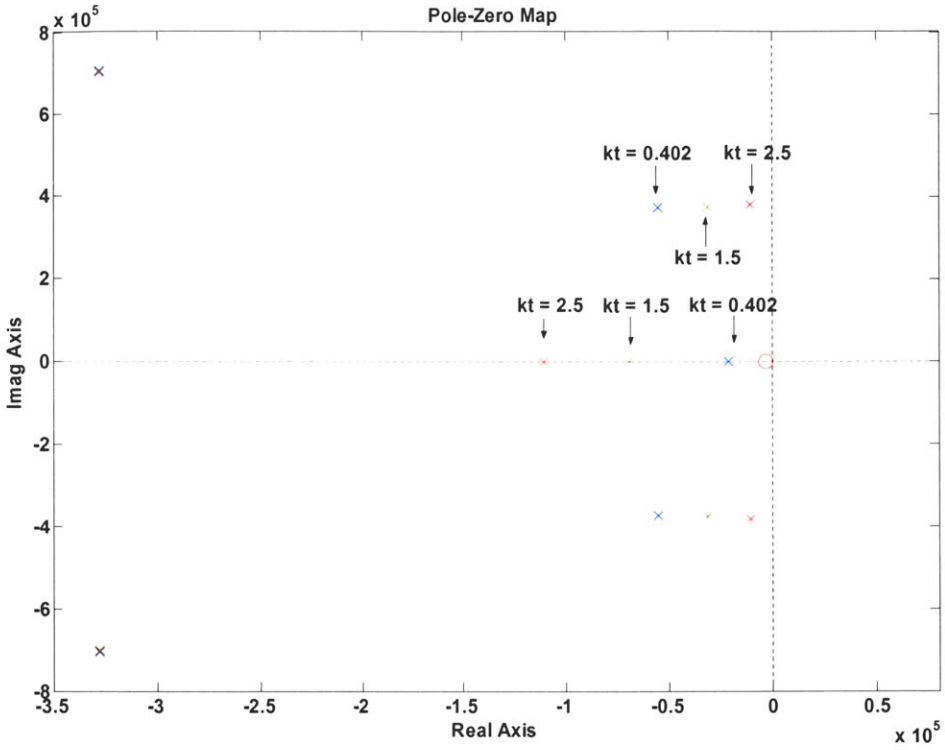

Figure 4-33. Pole-zero plot of two sources of resonance model with no piezoelectric force from input force to reticular lamina displacement where ξ_{bm} = 3.033 x 10^{-7} N·s/m. Different gain settings are shown, although k_t = 2.0 N/m is omitted for clarity. The zero is from the membrane time constant.

Figure 4-33 illustrates the pole-zero plot of the input force to RL displacement transfer function. With increased gain, the complex poles of the reticular lamina move closer and closer to the jω-axis while the poles of the basilar membrane are not affected greatly. The amplifier time constant is clearly sped up with increasing gain while a zero is fixed at $-1/\tau$ due to the amplifier time constant being in the feedback path. It is this real left half plane zero that generates the phase increase seen in Figure 4-32. If the OHC gain is made too large, the reticular lamina will go unstable, which may play a role in creating spontaneous otoacoustic emissions also.

4.6 Issues to be Resolved

There are several issues with this local model that need to be resolved by combining many local sections with appropriately scaled parameters to yield a traveling-wave model or by comparing the local model to experimentally observed cochlear micromechanics.

The effective basilar membrane damping, ξ_{bm}, was increased by a factor of 10 in Section 4.5.2 to reduce the sharpness of the second peak in Figure 4-23. A more detailed fluid mechanics analysis of the interactions between the basilar membrane and its surrounding fluid must be carried out in order to justify an increase in this parameter.

It may be that damping acts over a greater effective area than the OHC area itself. If this is true, then the reticular lamina damping coefficient may need to be magnified along with the BM damping coefficient to be accurate. In Figure 4-34, ξ_{rl} is also increased by a factor of 10 to 4.58 x 10^{-7} N·s/m and the Bode plot from input force to output basilar membrane displacement is shown for k_t set to 10, 15, 20, and 25. Note that with these changes, the shift of the first peak to higher frequencies with increased OHC gain is more pronounced but the general form of the diagram is similar to that in Figure 4-25. This suggests that increasing both the effective area of damping for the basilar membrane and reticular lamina may be a justified modification to the assumptions made earlier in this section as long as a larger OHC gain can be justified as well.

The amount of OHC gain that is necessary to produce a significant sharpening of the first peak in the basilar membrane displacement response is unclear and depends on the values of the mechanical parameters. Clearly, values of k_t in the range of 1 N/m can enhance the selectivity and gain on a local scale, as shown in Figure 4-25. With a greater

reticular lamina damping as in Figure 4-34, values of k_t had to be in the range of 15 N/m to yield significant sharpening. It could be that the OHC gain in bats or animals that require higher frequencies of hearing is greater than assumed here, implying higher values for the gain constant. Also, it may be the case that *in vitro* characterizations of the OHC gain underestimate the *in vivo* gain due to changes in physiological condition and possible damage. The local model must be incorporated into a traveling-wave system to determine what gain settings are sufficient to produce realistic responses and whether or not such gain settings are physiologically reasonable.

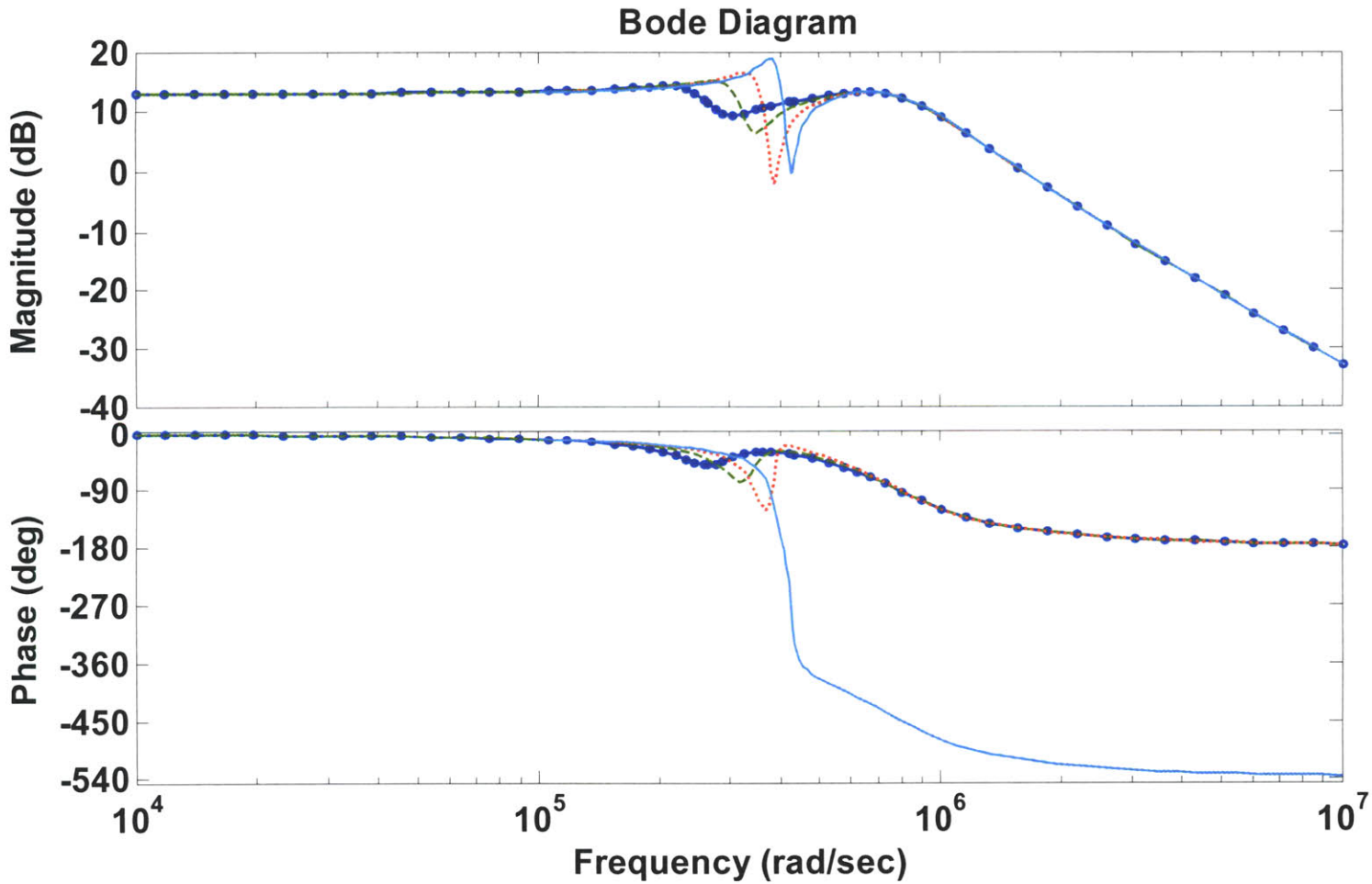

Figure 4-34. Bode plot of two sources of resonance model with no piezoelectric force from input force to basilar membrane displacement where ξ_{bm} = 3.033 x 10^{-7} N·s/m and ξ_{bm} = 4.58 x 10^{-7} N·s/m. Different gain settings are shown.

All parameters used in this model were scaled to the average area of the top surface of a single OHC, which has a diameter of about 9 μm [1]. However, such scaling may lead to inaccurate results if the action of a single OHC results in mechanical motion of its surrounding structures, such as the basilar membrane or the reticular lamina, that is much greater or much less than the area of the top surface of a single OHC. Thus, it is important to determine the space constant for this local model through experimental data and to scale the parameters accordingly.

Furthermore, this model does not include motion of the tectorial membrane, ignores the mechanical properties of the stereocilia and Deiters' cells, and does not incorporate the effect of the piezoelectric displacement current described in Section 4.3. These effects may modify the overall system response and need to be explored in later revisions. The model also combines parameter estimates from several different experimental studies and animals, including guinea pigs and bats. Whether or not these parameters can provide a realistic picture of cochlea mechanics must be explored using both a traveling-wave model and experimental data.

The overall transfer function from input force to basilar membrane displacement is not a canonical second-order system. Instead, it involves two pairs of complex poles along with one pair of complex zeros as well as a real pole and real zero. Whether or not such a system can generate realistic traveling-wave responses must be examined in detail along with experimental data. The special dynamics introduced by the complex zeros, which may enter into the right half plane while the poles remain in the left half plane, as shown in Figure 4-26, must be considered in particular.

4.7 Conclusions

Two mechanical models with a single source of resonance were presented in Sections 4.1 and 4.2. The former model had only one source of damping, the gap drag between the tectorial membrane and the reticular lamina. The latter model added drag to the basilar membrane. The amplifier membrane time constant manifested itself as a pole on the real axis at $-1/\tau$ and was sped up as it moved further into the left half plane with increasing OHC gain. In both these cases, only the basilar membrane had mass associated with it.

However, the first two models had the problem that increasing OHC gain did not increase the Q of the system significantly. This was due to a pair of complex zeros in the loop transmission that were too close to the pair of complex poles to generate considerable movement in the poles. Furthermore, the OHC gain, k_t, used was not large enough to push the amplifier pole past the 100 kHz point. These potential pitfalls were abolished by the introduction of another mode of resonance into the system by adding mass to the reticular lamina. This modification produced a root locus plot with two pairs of complex poles and one pair of complex zeros along with the membrane time constant. Thus, while one pair of poles traveled toward the complex zeros, the membrane time constant moved deeper into the left half plane and the other pair of complex poles had a trajectory into the right half plane, resulting in speedup of the membrane pole and increased Q for the system.

After converting the reticular lamina velocity, upon which the negative feedback of the OHC acts, into basilar membrane displacement, a zero was introduced to the overall transfer function that nearly canceled out the pole of the membrane time constant.

Thus, the effect of the membrane time constant on the basilar membrane was minimized by being sped up in the root locus plot and partially cancelled out by the zero. The transfer function from input force to basilar membrane displacement had a Bode plot with two peaks resulting from the two pairs of complex poles from the negative feedback loop and one pair of complex zeros generated by the conversion from RL to BM displacement. The second peak, however, was quite sharp and probably not very realistic using the initial parameters described in Table 4-1. Increasing the basilar membrane damping parameter, ξ_{bm}, by an order of magnitude reduced the second peak. Successively larger values of the OHC gain amplified and sharpened the first peak but barely affected the second peak. After a certain critical value of k_t, the pair of complex zeros were pushed into the right half plane, which results in a monotonically decreasing phase instead of one that dips, rises, and then decreases further, as shown in Figure 4-25. It was found in Figure 4-34 that increasing the reticular lamina damping parameter, ξ_{rl}, along with ξ_{bm} and a concomitant increase in OHC gain allowed a similar sharpening and amplification of the first peak to occur.

Thus, in the modified model with two sources of resonance, the magnitude of the overall transfer function from input force to BM displacement increases and sharpens with greater OHC gain. Because of the OHC time constant speedup, the membrane voltage at high frequencies should be larger than expected; as a result, the OHC and the overall cochlear amplifier can operate at much higher frequencies than previously expected. The additional near pole-zero cancellation from the RL velocity to BM displacement conversion means the membrane RC does not degrade the basilar membrane displacement characteristics significantly. However, the transfer function is

certainly not a canonical second-order system and so whether or not this local model can produce physiologically realistic responses must be evaluated by assembling a traveling-wave model. In addition, further work, experimental and theoretical, must be carried out regarding the cochlear micromechanics that led to the specific parameters and assumptions about the mechanical structures surrounding the OHC.

5 Traveling Wave Model

5.1 Relevant Issues

This section will describe relevant issues that must be addressed in the traveling-wave model to be developed in future work and will attempt to predict some qualitative behavior of the resulting system. A traveling-wave model can be constructed by coupling sections of the outer hair cell model described above. The two resonator model was only derived for a single outer hair cell and will be extended so that each section is composed of three outer hair cells, each OHC in one row of cells that travels down the length of the cochlea, and the relevant mechanical structures. Since there are about 4000 cells in each row, about 4000 sections will be constructed and coupled together to form the traveling-wave model [32]. If this is too computationally intense, several sections may be combined by aggregating and scaling the parameters appropriately to yield less individual pieces in the overall model.

Setting physiological parameters for the individual sections is crucial to obtaining a realistic response that matches experimental data. The OHC gain must be adjusted to accommodate for the different stereocilia heights when moving from the basal to apical regions and other effects, such as changes in the membrane conductance and the angle of inclination of the reticular lamina relative to the basilar membrane. The membrane time constant must be modified as well since the membrane capacitance should increase with longer cells as one travels towards the apex of the basilar membrane. The number of ion channels in the membrane may change as well, affecting the membrane conductance.

The parameters of the two resonators will be adjusted down the length of the traveling-wave model. Greenwood developed a function to model the characteristic

frequency along the length of the cochlea (x in mm, measured form the apex), which is given in Equation 5-1, where CF is the characteristic frequency, A is a constant in Hz that dictates the high-frequency limit of the function, a controls the slope of the frequency map, L is the length of the cochlea in mm, and K is a constant that determines the low-frequency behavior of the function [33].

$$CF = A\left(10^{ax/L} - K\right)$$

Equation 5-1. The Greenwood function determines the characteristic frequency, CF, at a position x (in mm) from the apex along the cochlea [34].

Based on the Greenwood function, the approximate resonant frequency that the two resonators should be at in each section will be approximated, thus determining the ratio of stiffness to mass. The Greenwood function has been determined for several species and has been shown to be a good predictor of experimental results with the parameter values shown in Table 5-1. Based on measurements by Fernández [26], the thickness of the basilar membrane decreases from ~7 μm to ~1 μm while the width of the basilar membrane increases from ~0.1 mm to ~0.3 mm from the basal to apical end. As an approximation, the mass of the basilar membrane will be considered a constant throughout the length of the cochlea and thus, the stiffness will be set according to the Greenwood function. The damping on the basilar membrane should probably be modified to take into account the CF at each position since the frequency of interest affects the boundary layer approximation.

Table 5-1. Greenwood function parameters for various species. Reproduced from Earlab [34] with parameters originally specified by Greenwood [33].

Species	Common name	A	a	K	L
Homo sapiens	Human	165	2.1	1.0	35
Chinchilla lanigera	Chinchilla	163.5	2.1	0.85	18.4
Cavia porcellus	Guinea pig	350	2.1	085	18.5
Mus musculus	House mouse	960	2.04	0.85	6.8

The stiffness of the reticular lamina will be determined by assuming that the reticular lamina is 5 to 10 times more compliant than the basilar membrane [11]. Based on observations by Mammano and Ashmore, the effective mass that must be moved with reticular lamina displacement may be assumed to be equal to that of the basilar membrane. The damping on the reticular lamina will also be adjusted to account for changes in gap length and the frequency of operation.

For simplicity, the coupling between individual local models will be initially approached with a 1-D model in which the fluid mass is assumed to be dominant. Since the output of each section is a displacement of the basilar membrane, this needs to be converted into a force that is transmitted to the next section. It may be sufficient to only include the fluid mass in a 1-D model [35]. Adopting this view of the cochlea, fluid incompressibility implies that scala tympani motion is exactly equal in magnitude and opposite in phase to scala vestibule motion and thus, the scala tympani can be discarded for analysis [35]. The resulting view of the model is shown in Figure 5-1.

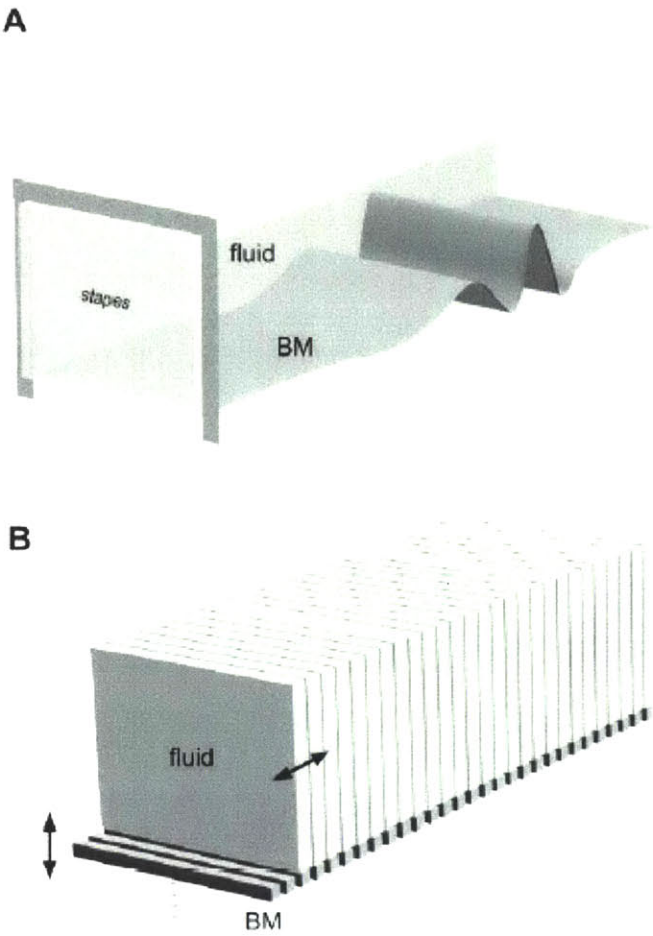

Figure 5-1. Generalized 1-D model of the traveling wave in the cochlea, where fluid motion is coupled with motion in the cochlear partition.
Reproduced from Kolston [35]

We assume that the velocity of the basilar membrane in the vertical direction couples directly into the longitudinal velocity of the fluid mass. Adopting the typical convention when converting fluid mechanics to electrical analogs that current represents velocity and voltage represents velocity, the corresponding electrical element that can be used to relate velocity to force is an inductor, where the inductance is equal to the fluid mass. This is diagrammatically shown in Figure 5-2, where V_{fm} the net force applied to the fluid mass and I_{fm} is the velocity of the fluid mass. Hubbard [15] also uses an inductor to model the fluid mass and thus includes an inductor connected in series with

the two local model sections. This convention for the fluid mechanics is opposite to the convention used in the local model sections in Section 4. Thus, when using the electrical model to simulate the solution, care must be taken to convert between the two conventions correctly. SPICE or Matlab will be used to provide traveling-wave solutions.

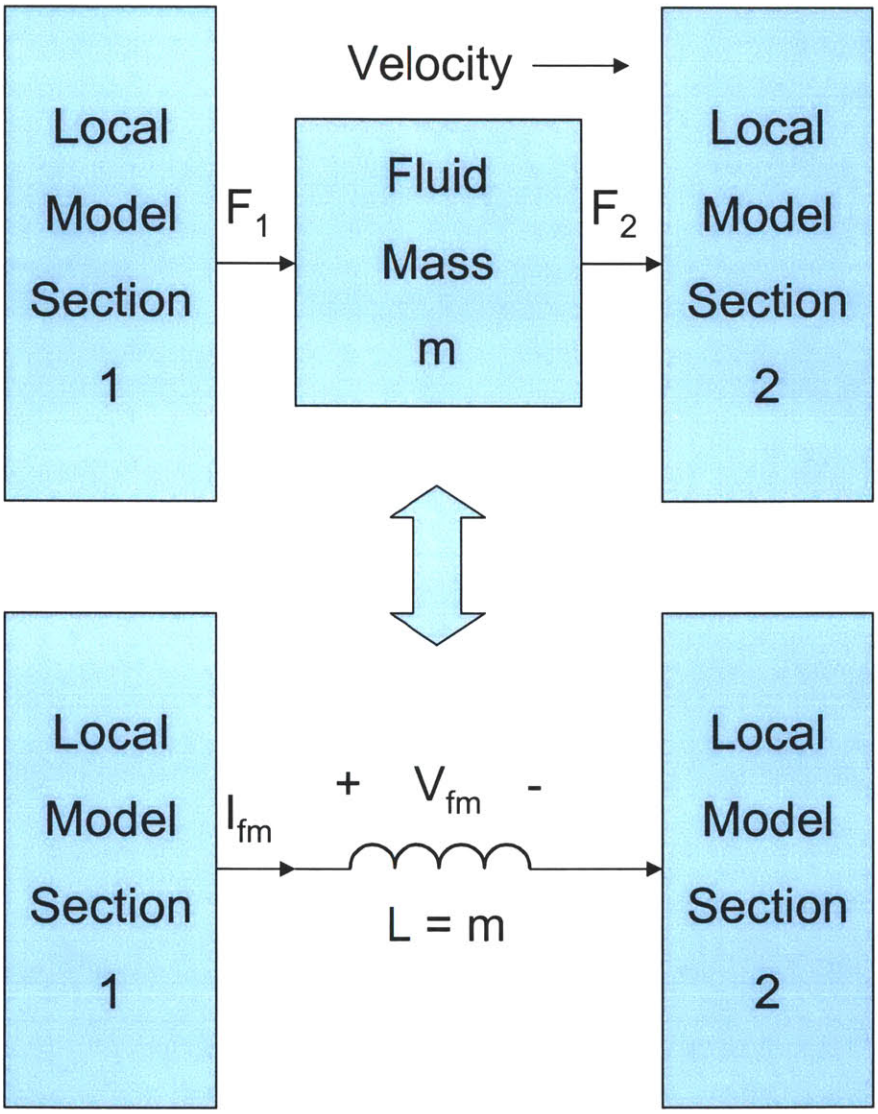

Figure 5-2. 1-D coupling via fluid mass can be modeled with an inductor with L = mass of the fluid. F_1 and F_2 refer to mechanical forces, V_{fm} refers to the net force across the fluid mass, and I_{fm} is the electrical analog current to mechanical velocity.

Despite the tremendous advantage in simplicity that a 1-D model gives, it may not be accurate enough to account for experimental observations, especially in producing a realistic phase response [35]. Kolston argues that the 1-D approximation is only valid

when the wavelength of the traveling wave is greater than that of the cross-sectional dimension of the cochlear duct [35]. As the traveling wave slows down near its CF as it is amplified significantly and encounters a large group delay, the wavelength of fluid motion decreases as well [35]. This wavelength drop results in additional fluid flow both vertically and radially, reducing the longitudinal flow and effectively increasing the fluid mass [35]. In modeling the traveling-wave nature of the model presented here, the fluid mass may be adjusted to increase to account for this effect or a 3-D model may be used instead. However, the Hubbard [15] model was essentially 1-D and seemed to be able to produce realistic magnitude and phase characteristics, so it remains to be seen what dimensionality is required in the traveling-wave model described here.

6 Comparison with Empirical Observations

6.1 Available Data

Comparing the output of the local two resonator model described in Section 4.5 directly to micromechanical measurements is currently unfeasible due to experimental difficulties in stimulating and recording over a limited spatial extent along the cochlea. Thus, a traveling-wave model must be constructed using the local sections in order to compare with empirical information. The majority of experimental data available describes the gain from the middle ear, either the malleus or the stapes, to basilar membrane displacement. Experiments have also characterized isovelocity mechanical tuning curves of the basilar membrane and frequency-threshold neural tuning curves.

Georg von Békésy won the Nobel Prize in 1961 for his measurements on the vibration of the cochlear partition in dead cochleas. He found that sound pressure waves moved down the cochlea as a traveling wave. In comparison with experiments on live cochleas performed a few decades later, von Békésy's data indicated poorer frequency selectivity [36]. An example of his experimental results is shown in Figure 6-1.

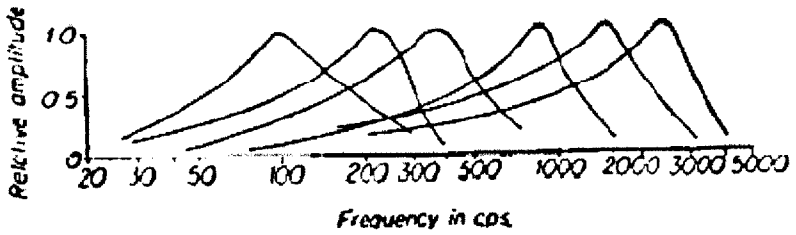

Figure 6-1. Data taken by von Békésy at six different points along a dead cochlear partition. The response exhibits poor selectivity compared to cochleas in which the cochlear amplifier is functioning. Reproduced from von Békésy [36].

In one of the first experiments using the Mössbauer technique to measure the amplitude and phase characteristics of basilar membrane motion *in vivo* for live cochleas,

Rhode produced the data shown in Figure 6-2 using squirrel monkeys [37]. The solid curve, indicated by the subscript 1, was measured at a location about 1.5 mm apical to the dashed-dotted curve, indicated by the subscript 2. Clearly, the amplitude ratio reaches a peak at a particular frequency and has an extremely sharp cutoff afterwards, indicating that with the cochlear amplifier operating, basilar membrane displacement exhibits a greater sensitivity and selectivity than in dead cochleas such as those examined in Figure 6-1. The phase data in Figure 6-2 shows that at low frequencies, the basilar membrane motion in squirrel monkey leads that of the malleus by about 90°. Rhode also found the phase lead in guinea pig cochleas to be about 90° [38].

Furthermore, the data in Figure 6-2 shows that a smaller secondary peak resides after thee sharp rolloff beyond the primary amplitude peak. It is not too clear from this figure whether or not the amplitude flattens out or continues to decrease after this point. Around the same region where the amplitude bump occurs is a small peak in the phase followed by a plateau.

The amplitude notch and phase plateau are evident in other data as well. For example, Ruggero et al. [39] measured the velocity gain from the stapes to the basilar membrane in a chinchilla at a point 3.5 mm from the stapes and found a notch in the gain at about 3 to 4 kHz from the peak. This data is shown in Figure 6-3. It is an interesting to note that the gain measured in Ruggero et al. [39] is almost 60 dB greater than that in Rhode [37], probably due to the sensitivity of the experiments to the preparation protocols used. The phase plot Ruggero et al. present also exhibits a plateau beyond the sharp rolloff [39]. Unlike the 90° phase lead of the squirrel monkey basilar membrane

displacement to stapes/malleus displacement seen in Figure 6-2 at low frequencies, there is a 180° phase lead in the chinchilla in Figure 6-4.

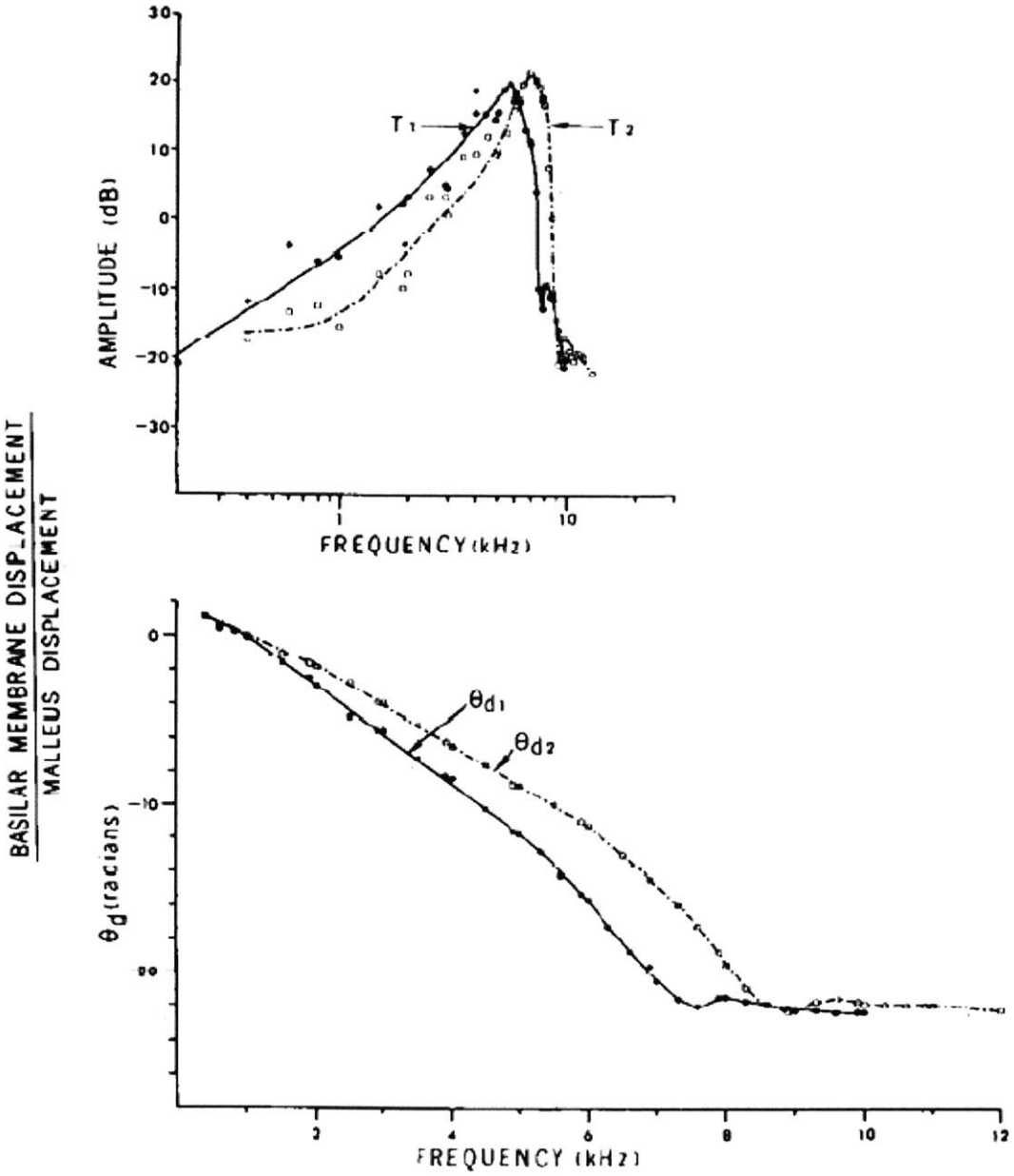

Figure 6-2. Ratio and phase of basilar membrane to malleus displacement in squirrel monkeys using the Mössbauer technique.
The dashed-dotted lines were measured at a location at about 1.5 mm basal to the sold lines. Note the there is a secondary peak after the primary peak in the amplitude around the same location as a plateauing of the phase. Reproduced from Rhode [37].

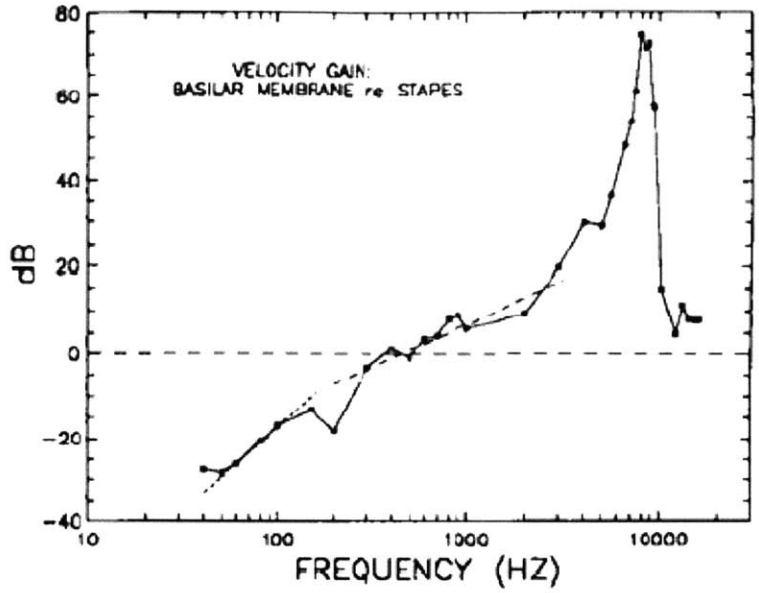

Figure 6-3. Velocity gain from the stapes to the basilar membrane in a chinchilla measured 3.5 mm from the stapes.
The short dotted line shows 12 dB/oct while the long dashed line is 6 dB/oct for reference. Reproduced from Ruggero et al. [39].

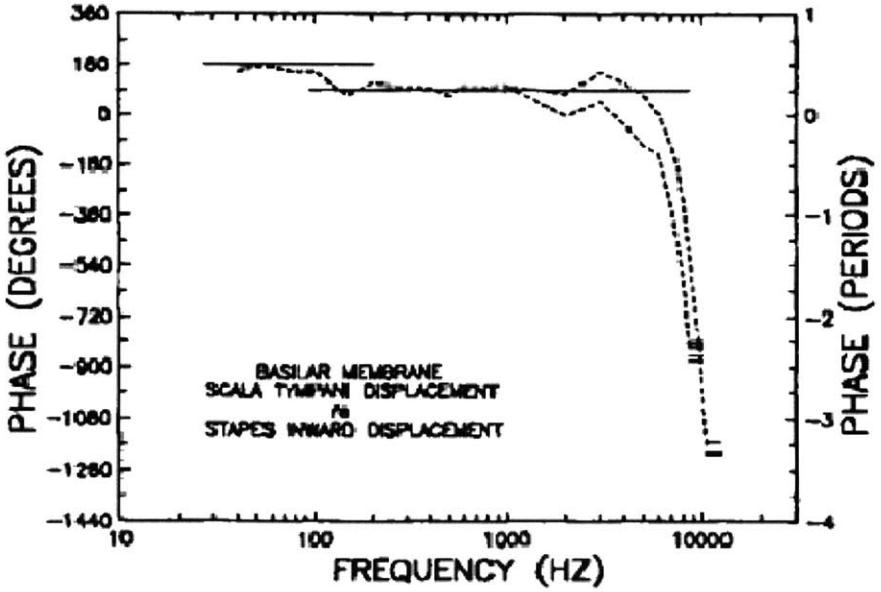

Figure 6-4. Phase of basilar membrane displacement referenced to the stapes inward displacement in a chinchilla.
The low frequency asymptote is 180° and the phase seems to plateau at high frequencies after a sharp cutoff. Reproduced from Ruggero et al. [39].

The amplitude notch is also evident in data taken on the sensitivity of basilar membrane displacement over stimulus pressure (expressed in SPL) in the chinchilla and guinea pig cochleas. Figure 6-5 demonstrates that the sensitivity in both the chinchilla

(data on the left) and the guinea pig (data on the right), exhibits amplitude notches and possible plateaus above the characteristic frequencies. These notches are more prominent for higher stimulation pressures and cannot be ruled out for the lower pressure levels because the data taken did not extend far enough past the characteristic frequencies.

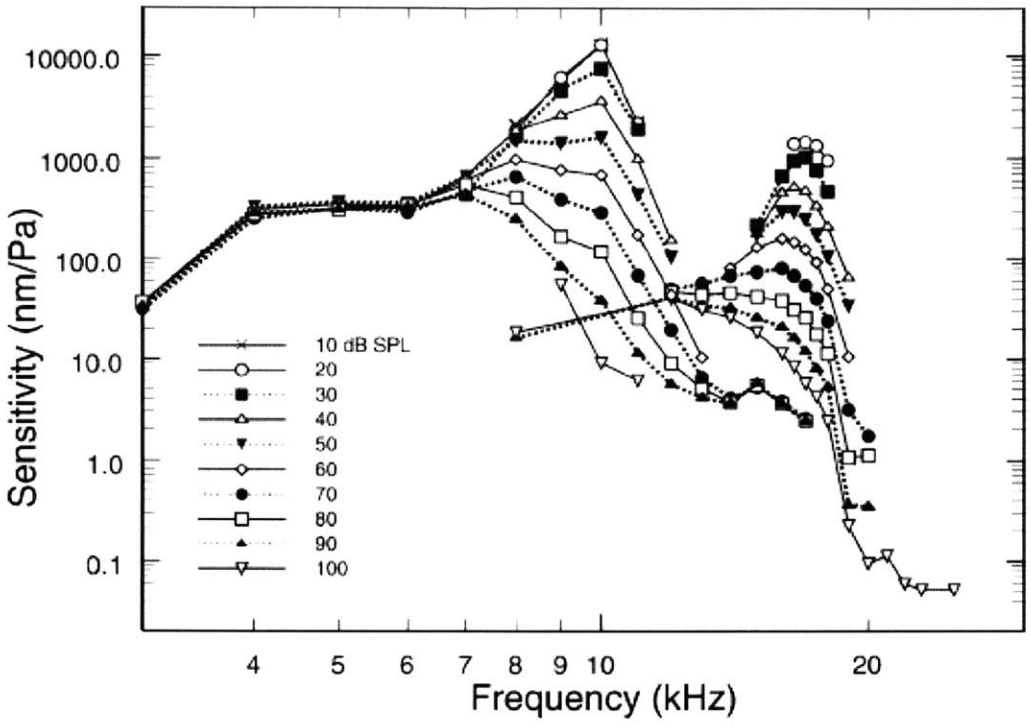

Figure 6-5. Family of isointensity curves where the sensitivity is plotted in a chinchilla. The sensitivity is given by the basilar membrane displacement over the stimulus pressure. The data on the left was taken in a chinchilla at 3.5 mm along the cochlea while the data on the right was from the basal region of the guinea pig cochlea. Reproduced from Robles and Ruggero [40].

In addition to the gain characterizations shown above, investigators have compared mechanical tuning to neural tuning in the form of frequency-threshold curves. In these experiments, mechanical tuning curves are derived by finding the stimulus level at which the displacement or velocity attains a certain value for each frequency. Neural tuning curves are found by determining the sound pressure levels that elicit a specified threshold spike rate. Since conventional theory posits that basilar membrane motion, either velocity or displacement, is directly translated into inner hair cell depolarization

and thus stimulation of the auditory nerve, mechanical tuning curves for the basilar membrane and neural turning curves for auditory-nerve fibers have been compared.

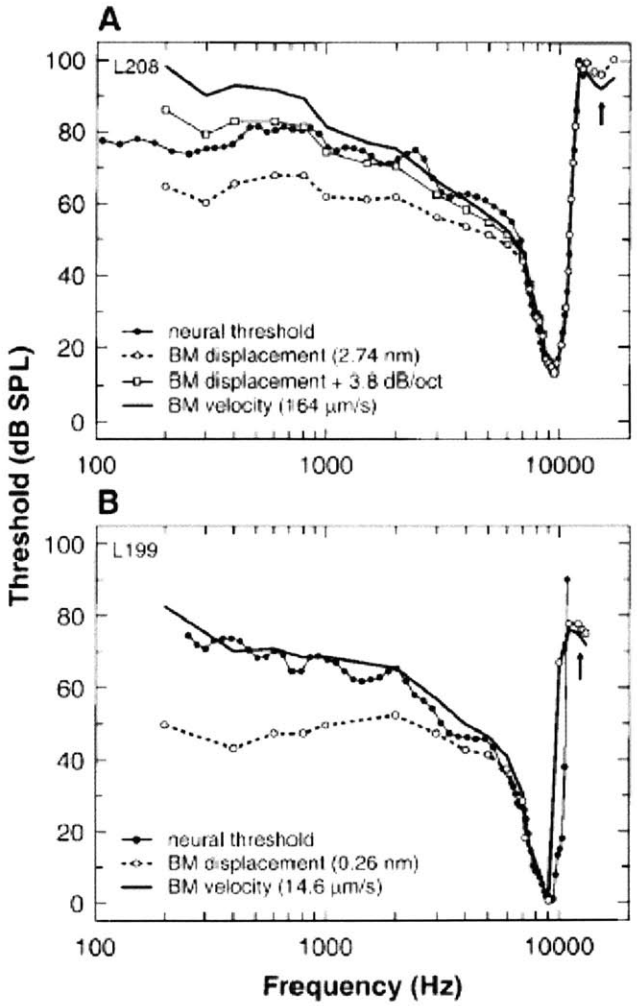

Figure 6-6. Frequency-threshold tuning curves for basilar membrane displacement and velocity as well as auditory neural fibers in two different chinchilla cochleas. The data in squares in part A refer to basilar membrane displacement with a 3.8 dB/oct high-pass filter. The fibers had spontaneous firing rates of 11.2 and 76.3 spikes per second in A and B, respectively. Reproduced from Narayan et al. [41].

Narayan et al. obtained mechanical and neural tuning curves from the same locations in chinchilla cochleas, as shown in Figure 6-6 [41]. From their data, it appears that near the characteristic frequency, both BM displacement and velocity are in good agreement with the neural threshold tuning curves. However, at frequencies lower than the characteristic frequency, the neural threshold curve is not well predicted by either BM

displacement or velocity alone. In part A of Figure 6-6, Narayan et al. high-pass filtered basilar membrane displacement with a rate of 3.8 dB/oct and found that the resulting mechanical tuning curve was able to better predict the neural tuning curve [41]. This data suggests that basilar membrane motion undergoes some mechanical signal transformation before affecting the stimulation of the auditory nerve fiber.

Mechanical tuning curves can be derived from the traveling-wave model developed using local sections of the two resonator model described in Section 4.5. However, to compare that model to neural tuning curves requires analysis of the inner hair cell and its surrounding structures. The traditional view of auditory nerve fiber stimulation is that movement of the BM towards the scala vestibule should cause IHC stereocilia to rotate in an excitatory direction away from the modiolus, depolarizing the membrane and causing a spike to be fired [42]. IHCs in the basal region of the cochlea have been found to depolarize in phase with the velocity of the BM in the direction of the scala vestibule [42]. However, data recorded by Ruggero et al. [42] in the basal region of the cochlea indicates instead that auditory-nerve-fiber excitation follows an intermediate between BM velocity and displacement towards the scala tympani! As shown in Figure 6-7, the phase of auditory nerve fiber firing corresponds with basilar membrane motion towards the scala tympani, at least for low frequency stimulation. The phase difference between inner hair cell depolarization and auditory nerve responses is not present in the apical region of the cochlea [42]. It will be important to reconcile this paradox with the model described in this thesis in both the basal region and apical region, where the cochlea amplifier may not be significant. It may be that RL or TM motion is more intimately connected with IHC depolarization and auditory nerve firing than BM motion.

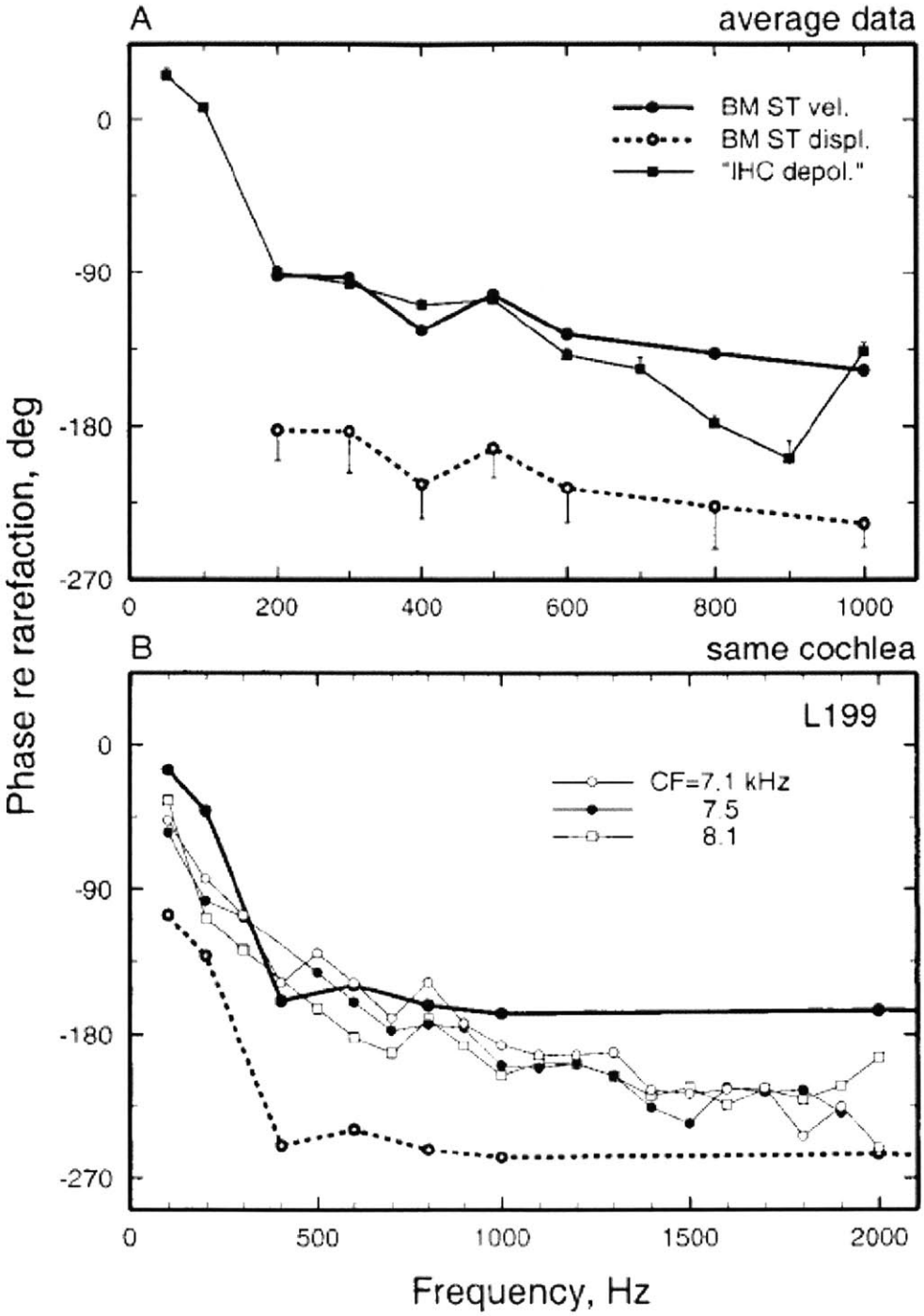

Figure 6-7. Phase responses of basilar membrane velocity and displacement and auditory nerve fiber firing in the basal region of the cochlea.
Part A shows average auditory nerve fiber data indicated by the squares. Part B shows three sets of data from single auditory nerve fibers with different characteristic frequencies. Note that basilar membrane motion towards the scala tympani instead of the scala vestibuli that seems to predict auditory nerve fiber response. Reproduced from Ruggero et al. [42].

6.2 Theoretical versus Experimental Predictions

6.2.1 Local Model Comparisons

Few experiments have been conducted where a local section of the cochlea is stimulated and local mechanical deformations are observed. This makes it difficult to validate the local model described in Section 4. Luckily, Mammano and Ashmore [11] did do a local study where they injected current into a section of outer hair cells and observed the reticular lamina and basilar membrane motion. The two resonator model is able to compare favorably with the data they obtained.

Since the Mammano and Ashmore study was conducted at low frequencies, the parameters used in Section 4 must be modified [11]. They observed basilar membrane motion to have a resonant frequency of about 2.3 kHz and reticular lamina motion to resonate at about 1.0 kHz at a location 11 mm along the base of the cochlea. The mass of the basilar membrane is estimated by multiplying the thickness of the BM and the area of the bottom face of the cylindrical OHC with the density of water, as in Section 4. Since the thickness of the BM is about 3 μm at 11 mm along the base of the guinea pig cochlea [26], we assume that the OHC radius is constant at 4.5 μm and thus we determine the mass of the BM, $m_{bm} = 1.9 \times 10^{-13}$ kg. For convenience, we set $m_{bm} = m_{rl}$, where we note, as before, that m_{rl} may include the effective mass of the tectorial membrane and other related structures. Knowing the masses and the resonant frequencies of the RL and BM allows the determination of the RL stiffness and the BM stiffness by $\sqrt{(k/m)}$ = resonant frequency. Thus, k_{rl} is approximately 7.5×10^{-6} N/m and k_{bm} is 3.968×10^{-5} N/m.

In lieu of exact anatomical data, we assume that the OHC cell length is about 60 μm at this location with a maximum stereocilia height (and thus gap height) of 4 μm [43].

Thus, according to the 360/L mN/m scaling relationship from Dallos [25], k_{ohc} is about 6 mN/m. At 1 kHz, the boundary layer is $\delta \sim 15.1$ μm. Since this is much larger than the RL-TM gap, the damping on the RL is calculated using the gap height and found to be about 3.026×10^{-9} N·s/m. The basilar membrane drag is calculated using the boundary layer δ and found to be about 1.145×10^{-8} N·s/m. According to Housley and Ashmore [44], the time constant of a 60 μm cell is approximately 1 ms. Here, we assume $\tau \sim 2$ ms which is reasonable as well. The OHC gain, k_t, is reduced from 0.402 N/m to 0.0602 N/m, which may be accurate since the gain is expected to decrease for lower frequency operation. Since the current that Mammano and Ashmore [11] injected did not all make it into the OHC, a sensitivity factor, r, is introduced into the block diagram of the system shown in Figure 6-8 to fit the data more accurately. r represents the gain from the input current injected into the cochlea to the voltage inside of the outer hair cell and includes effects such as current spreading from the pipette, the resistance of the cell membrane, and other factors. The magnitude of r is given as 24.8 V/A by Mammano and Ashmore [11] but is adjusted to about 150 V/A here in order to provide a better fit to data. This is not a drastic change since the other parameters affect the DC gain of the system as well and parameters are being culled from many different sources and experimental setups.

Mammano and Ashmore injected 100 μA current into a local section of the cochlear partition through a 5 μm stimulating pipette [11] and observed the resulting basilar membrane and reticular lamina motion with a displacement-sensitive laser interferometer. The block diagram in Figure 6-8 attempts to model this experimental setup as the input force, F_{in}, is set to zero and the input current, I_{in}, adds to the membrane potential. I_{in} also modifies the RL displacement to BM displacement transfer function.

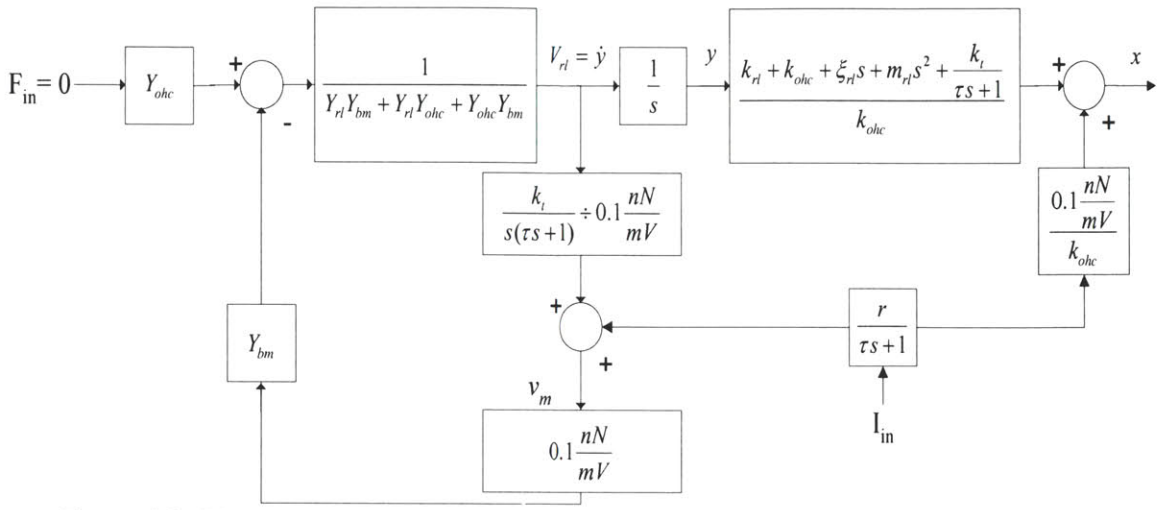

Figure 6-8. Block diagram for current stimulation as done in Mammano and Ashmore [11]. Current injected into the OHC adds to the membrane potential and must also be included in calculating the transfer function from the reticular lamina displacement (y) to the basilar membrane displacement (x). r is the gain from input current to OHC membrane potential.

The model's BM and RL displacements for I_{in} = 100 μA are shown in Figure 6-9 and Figure 6-10, respectively. Experimental data from Mammano and Ashmore is shown in Figure 6-11 [11].

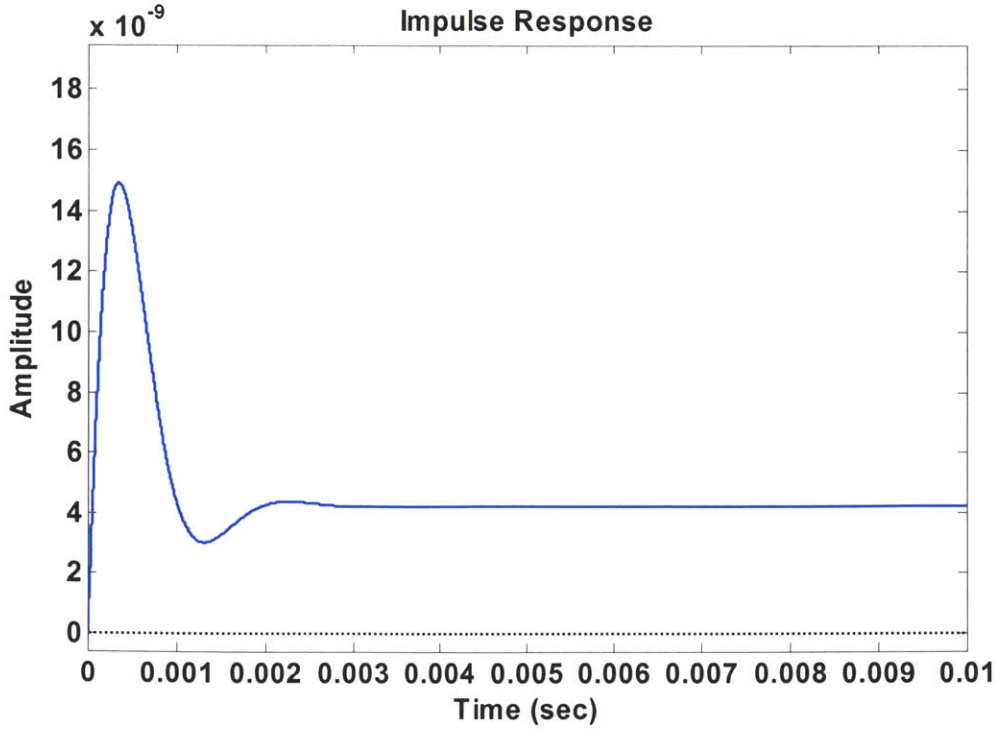

Figure 6-9. BM response to a step in I_{in} for the Mammano and Ashmore [11] experiment. Amplitude is in meters.

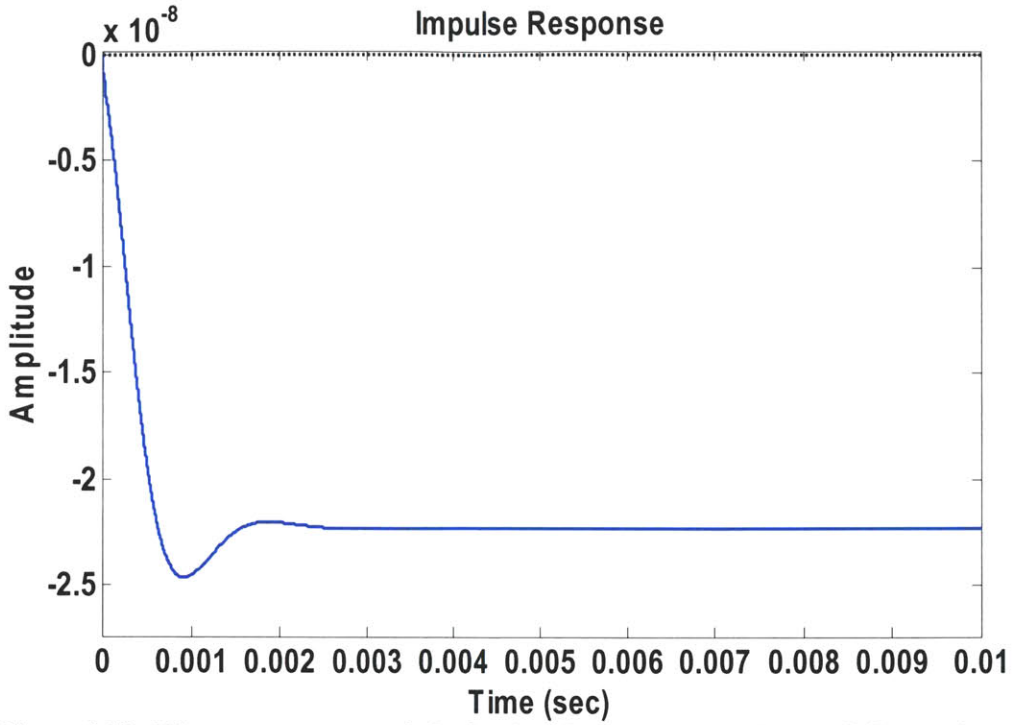

Figure 6-10. RL response to a step in I_{in} for the Mammano and Ashmore [11] experiment. Amplitude is in meters.

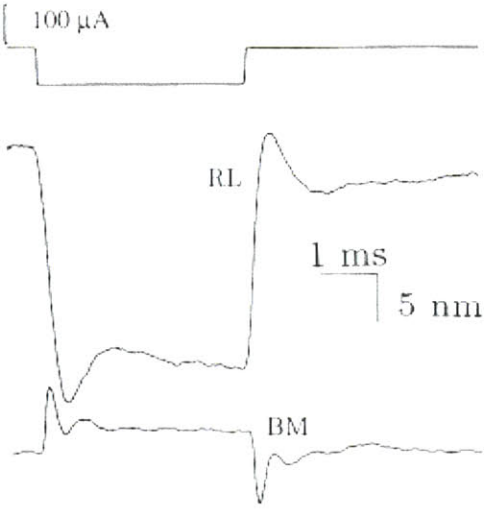

Figure 6-11. Data from the Mammano and Ashmore local current injection experiment [11]. RL indicates reticular lamina displacement and BM is basilar membrane displacement. Reproduced from Mammano and Ashmore [11].

As predicted, BM is upwards and RL is downwards in the two resonator model and matches the experimental data. The BM response has a faster rise time in both the model and the experimental data as well. The BM also shows a smaller second peak in

both the model and the data while the RL only seems to ring once before settling. The final BM displacement also matches well, being about 4 nm in Figure 6-9 and about 3 nm in Figure 6-11. The RL displacement settles to about 25 nm in both the model and the data as well. The largest discrepancy between the data and the two resonator system is the peak of the basilar membrane displacement, though the peaking behavior of the RL in the model matches quite well with experiment. In Figure 6-9, the apex of the basilar membrane response rises to about 15 nm while the data indicates a peak of only about 6 nm. This problem may need to be reexamined in future revisions of the two resonator model or removed by modifying the parameters used. Thus, despite the discrepancy between BM peaks in the model and the data, the two resonator system appears to match Mammano and Ashmore's [11] data well in response to a step in input current.

6.2.2 Traveling-Wave Comparisons

Since the traveling-wave model has not been fully developed, only qualitative comparisons between the theoretical traveling-wave model using local sections in Section 4 and the experimental data described in Section 6.1 will be discussed.

The general form of the two resonator model is encouraging because the first peak of the BM transfer function is amplified and sharpened with increasing outer hair cell gain while the second peak remains quite constant. Experimental data described above demonstrates that the gain from stapes motion to BM motion increases at low frequencies, peaks at the characteristic frequency, proceeds to drop sharply in amplitude, and then exhibits a notch. This notch may be due to the second peak in the local outer hair cell model. The first peak in empirically observed gain plots such as Figure 6-5 sharpens with presumably increased OHC gain, which would be predicted from the local outer hair

cell model. Furthermore, the first peak also moves to a higher frequency with outer hair cell gain as also observed in the local OHC model in Figure 4-25.

The phase data must also be compared to ensure that the model correlates with observations. As described above, both 90° and 180° phase leads at low frequencies have been observed in different animals for the transfer function between stapes movement and basilar membrane movement. In the 1D model described in Section 5, motion of the stapes is coupled through the fluid mass to impose an input force on the first local section. The velocity to force transfer function assuming the impedance is composed of just fluid mass has a phase of 90°. Thus, going from stapes displacement to input force to the first stage has a phase shift of 180°. Since the first stage has an input force to basilar membrane displacement transfer function with a low frequency phase of 0° as seen in Figure 4-25, the low-frequency phase between BM and stapes motion of the traveling-wave model should have a 180° value. In order to obtain a 90° phase lead as observed in some animals, a traveling-wave model with a higher order of dimensionality or a model where the fluid impedance is composed of viscous elements as well as mass elements may be required.

The phase data described earlier in this section shows the tendency to plateau to a value that is usually an integer multiple of π ($\Theta = N\pi$ where N = 7, 8, 9), according to Rhode [37]. Since the phase in experimental data flattens out at frequencies higher than the CF, we see from Figure 4-25 that this should correspond to the high frequency region where the phase of the basilar membrane transfer function reaches -180° (assuming that the complex zeros are not in the right half plane). Thus, in order to produce phase plateauing, the coupling between each individual section should have a phase of 180°

from the output velocity of a basal section to the input force onto a more apical section. After the CF, the transfer function from input force to output BM displacement is essentially mass dominated. Since the 1-D model assumes that only fluid mass is significant, the resulting system is a mass network composed of fluid mass and the mass-dominated basilar membrane response. In such a system, the phase shift may not significant. If true, this effect in the model would match the expected experimental phase behavior.

7 Future Work

This thesis developed a local outer hair cell feedback model that incorporated two resonators coupled together by the outer hair cell passive and active characteristics. Although qualitative simulations of the model seem to be supported by experimental data described in Section 6, there is a tremendous amount of work that must be carried out for this model to be ultimately confirmed or rejected. In this section, I will attempt to describe the most pressing issues and some potential methods of approach.

Negative feedback is used in engineered systems to provide stability, robustness to sensitive parameters, and to limit the effect of noise. Biological systems such as the cochlea are likely to require these benefits to operate. Thus, future work should explore how negative feedback or other mechanisms in the local outer hair cell and traveling-wave models can generate these effects. Other feedback analysis techniques such as return ratio analysis or Mason's rule may be beneficial in helping to understand the underlying dynamics of this complicated system.

The piezoelectric effect was largely ignored in the analysis described in Section 5 in an attempt to simplify the system. However, piezoelectricity may play an important role in limiting the effect of the membrane time constant and will need to be examined in greater detail in future work [14]. The fact that the hair cell piezoelectric coefficient of guinea pigs is over four orders of magnitude greater than any man-made material suggests that the outer hair cell piezoelectric characteristics are biologically relevant [16]. Like minor loop feedback, piezoelectricity may work to minimize the sensitivity of the system to variations in poorly controlled parameters or to provide additional speedup of

the slow membrane time constant. Thus, the piezoelectric effect will be explored extensively in future work.

Another issue that should be addressed immediately is the construction and simulation of the traveling-wave model. As described in Section 6, verification of the local outer hair cell model is only likely to occur if traveling-wave results can be compared to experimental data. Issues regarding the assembly of local sections to form a traveling-wave amplifier were discussed in Section 5 and are currently being addressed. The effect of changes in the local OHC model on the overall traveling-wave system should also be characterized.

The tectorial membrane was assumed to have a displacement of zero in the local outer hair cell model. This is almost certainly incorrect in the real biological system since movement of the reticular lamina can be coupled into the tectorial membrane via the stereocilia and the fluid in the TM-RL gap. The static and dynamical properties of the tectorial membrane have been characterized and should be included in future models for completeness [19]. The TM may be important in stimulating inner hair cells and causing auditory nerve fibers to fire. Furthermore, the reticular lamina response was sped up by the effect of negative feedback. This may also affect IHC stimulation and should be also investigated in future work. Thus, after developing an accurate traveling-wave system to simulate basilar membrane displacement, a model for describing inner hair cell and auditory nerve firing as a result of mechanical motion and fluid flow will be analyzed. The literature indicates that the true cause of inner hair cell depolarization is unknown. Nonetheless, this is an important endeavor to pursue so that neural tuning curves can be used to verify or disprove this model as well.

Parameters used in this model need to be verified with greater theoretical rigor and experimental data. For example, the assumption that viscous drag dominates the fluid flow in the TM-RL gap over inertial effects needs to be examined with the Navier-Stokes equation and other concepts in fluid mechanics. The viscoelastic properties of outer hair cells may be important as well and should be analyzed in future work. Of particular importance is the scaling of the OHC stiffness as well as the gain of the OHC. At low frequencies, outer hair cells are more compliant and the gain may decrease, thus affecting the dynamics of the system.

The ability of the putative cochlear amplifier to generate spontaneous otoacoustic emissions provides hints into the inner workings of the outer hair cell feedback system. From the results presented in Section 4, increased OHC gain can lead to instability in the basilar membrane and the OHC membrane potential. How such instability can generate spontaneous otoacoustic emissions must be explored. Future efforts should address the production of these spontaneous emissions from the model presented in this thesis.

Perhaps most importantly, *in vivo* and *in situ* experimental work is required to truly verify the validity of this model. Measuring the actual frequency response of the OHC membrane voltage in response to auditory inputs at the stapes or in response to local forces applied on the basilar membrane directly would be very useful. Beads could be bound to the basilar membrane and modulated with optical traps to provide a suitable local input. Specific data about the characteristics of reticular lamina motion similar to the experiments and measurements that have been carried out for basilar membrane motion would provide another way to test this model. Additionally, measuring the space constant over which outer hair cell motility is significant over its surrounding structures

would provide a better estimate of the parameters to be used. Studies to characterize the dominant sources of viscous drag in the cochlea are also necessary to determine how the outer hair cell must operate as a cochlea amplifier.

Much of the future work described in this section is under active research but was not included in this thesis. However, these are certainly only a few of the items of interest and the author encourages others to pursue these research directions to help advance the understanding of this field.

8 Key Insights

Eight key insights about the local outer hair cell model were developed in Section 4 and Section 6 and will be described here in summary. These points are important for understanding the operation of the putative cochlear amplifier in the biological cochlea.

The first model described in Section 4 only had damping on the reticular lamina and not on the basilar membrane. The BM was composed of a mass and spring while the RL was made up of a dashpot and a spring. If the damping on the RL was increased to infinity, the Q of the basilar membrane response approached infinity as the basilar membrane dynamics were essentially decoupled from the RL dynamics. From an electrical circuit perspective, the reticular lamina voltage (velocity) was essentially grounded. On the other hand, if the reticular lamina damping was too small, the Q of the basilar membrane response reached infinity as well, because the dashpot on the RL was essentially too slow to affect the system dynamics. Therefore, if there is only damping on the reticular lamina as in the first local outer hair cell model, there is an optimum reticular lamina damping for minimum Q at the basilar membrane. From an evolutionary standpoint, it seems unlikely that the cochlea would develop into a system with minimum Q when both extremes of a passive parameter like damping would yield greater selectivity and sensitivity, which is desirable in sensory organ.

As a result of the first key insight, damping was added at the basilar membrane. However, in this second model, the lack of mass at the reticular lamina prevented the cochlea amplifier from providing a great deal of speedup and significant Q sharpening. Figure 4-13 demonstrates that without mass at the RL, the reticular lamina pole is on the real axis. Thus, the RL pole and the amplifier pole come together and split off the real

axis, which limits the speedup of the amplifier time constant and slows down the reticular lamina dynamics. Furthermore, the basilar membrane poles move to complex zeros that are nearby, limiting the sharpening and selectivity generated by the cochlear amplifier.

The limitations of the first two models developed resulted in the adoption of a new model with resonant basilar membrane and reticular lamina dynamics. The third insight developed here is that the two resonator system can provide speedup and increased Q in the mechanical responses as well as the membrane potential. The resulting root locus plot for the membrane potential provided several desirable characteristics as shown in Figure 4-17. The only real pole was the amplifier time constant, which could be sped up without constraint with larger OHC gain. With two pair of complex poles and one pair of complex zeros, one pair of the complex poles were able to move closer to the $j\omega$-axis, increasing the gain and selectivity of the system at resonance. As seen in Figure 4-18, the resulting closed-loop transfer function from input force to output membrane voltage exhibits two resonant peaks that serve to increase the membrane potential at the respective resonant frequencies and a sped-up membrane time constant. Thus, the membrane potential is sufficient to operate the cochlear amplifier at high frequencies due to mechanical resonance and negative feedback.

The fourth insight presented by this thesis is that the primary effect of the cochlear amplifier is to move the poles due to the reticular lamina and not the poles due to the basilar membrane. As in the root locus plot in Figure 4-17, the complex basilar membrane poles, which are the ones at a higher frequency than the reticular lamina poles, are constrained by the complex basilar membrane zeros. However, the reticular lamina poles are unconstrained and can move out into the right half plane. Thus, in the

biological cochlea, this may mean that the reticular lamina plays a larger role in controlling the dynamics of the system than previously appreciated. For example, the reticular lamina may directly affect IHC stimulation and will be important to study in future experiments.

The fifth major insight developed in Section 4 pertains to the sharpening of the first peak in the basilar membrane transfer function and removing the effect of the membrane time constant on the BM response. As shown in Figure 4-26, the conversion from RL displacement to BM displacement introduces a pole at $-1/\tau$ that cancels out with the fixed zero at $-1/\tau$ in the closed-loop RL transfer function shown in Figure 4-33. In addition, the conversion introduces a pair of complex zeros and a complex pole that move with changing OHC gain, k_t. The complex zeros head towards the right half plane while the real zero travels into the left half plane with increased k_t. Thus, the zeros follow a root contour plot that mimics the motion of the amplifier pole and the reticular lamina poles, since the former moves into the left half plane while the latter move into the right half plane with larger OHC gain. This effect helps to further remove the effect of the amplifier time constant from the basilar membrane via a near pole-zero cancellation. Furthermore, the presence of the complex poles followed by faster complex zeros results in a sharp peak followed by a sharp dip around the resonance of the first peak in Figure 4-25. The sharp dip may be important for cutting off frequencies that are higher than the CF. Thus, the limitations of the slow OHC membrane time constant on the basilar membrane are minimal so that the OHC's primary purpose is to sharpen the resonant BM transfer function.

The sixth insight generated by the local outer hair cell model is that a realistic response may require greater basilar membrane damping than computed in the parameter derivation portion in Section 4. However, it was also seen that if both the RL and the BM damping are increased in the same proportion – which would be reasonable if the space constant of motion is larger than the OHC area itself – and the OHC gain, k_t, was also increased, a sensible result could be obtained, as shown in Figure 4-34. Thus, the outer hair cell gain in the biological cochlea may be larger than assumed here while the space constant may be larger than used here as well.

The seventh insight explains the sharpening and speedup of the first resonant peak in the basilar membrane transfer function with a circuit analogy. As explained in Section 4.5.3, the RL is damping dominated while the BM is stiffness dominated at the first peak in the BM. Without the outer hair cell gain, the impedance of the outer hair cell and reticular lamina together looks purely inductive (stiffness) and resistive (damping), as shown in Figure 4-30; since the BM is inductive in this regime, the resulting BM response does not peak. The introduction of the outer hair cell gain creates an effective capacitive component in the combined OHC and RL impedance looking in from the basilar membrane. Increasing the OHC gain, k_t, reduces the value of the capacitor and thus speeds up and sharpens the first resonant peak in Figure 4-25. This method of looking at the BM response around the first resonant peak also explains the sharp dip following the peak.

Finally, the last key insight developed in this thesis is that the two resonator model is able to match the observations of Mammano and Ashmore quite well. As demonstrated in Section 6.2.1, the reticular lamina and basilar membrane move in

opposite directions in response to outer hair cell contraction with damped characteristics. It is the anti-phase nature of the RL and BM movement that produces the negative feedback so crucial to the speedup of the outer hair cell time constant and the sharpening of the resonant mechanical system.

By analyzing the outer hair cell local model with feedback techniques, I was able to demonstrate several key features of the cochlear amplifier, which I described in this section. These points are valuable since they provide insight into the operation of the biological cochlea and help to explain how the limitation of the membrane time constant is overcome *in vivo*.

9 Conclusions

Outer hair cell motility is the most likely candidate for the putative cochlear amplifier but still has not been confirmed in that role due to many outstanding questions. One problem with existing cochlear amplifier theory is the outer hair cell time constant is generally a few orders of magnitude too slow to produce significant membrane voltages at high frequencies. Since the outer hair cell motor, prestin, is activated by its receptor potential, it seems unlikely that voltage-dependent motility of outer hair cells could operate at the high frequencies (≥ 100 kHz) at which mammalian hearing has been observed. Indeed, this is perhaps one of the largest stumbling blocks in establishing the outer hair cell as the cochlear amplifier. In this thesis, I attempted to propose a solution to the limiting dynamics of the electromotile response by using feedback analysis.

In mechanical or electrical systems, feedback is a commonly used technique to provide beneficial characteristics that are often difficult to achieve with open-loop or feed-forward techniques. In Section 2, I introduced several negative feedback methods used with mechanical systems, in particular those with DC motors. Velocity control can be achieved by sensing the output velocity with a tachometer and feeding this information back into the input with an appropriate compensator. Position control is often implemented by detecting the output position with a potentiometer and using this data for feedback. Both these methods can yield high DC gain systems with little steady-state error, closed-loop stability, and speedup of slow motor time constants. Minor loop feedback is also described in Section 2 as a method to gain more flexibility in shaping the closed-loop transfer function. Minor loop feedback is useful in minimizing the

sensitivity of the closed-loop transfer function to fluctuations in poorly maintained parameters like the moment of inertia of a flywheel.

An introduction to outer hair cell electromotility along with simple cochlear mechanics was presented in Section 3. Essentially, the cochlea supports a traveling fluid wave down the cochlear partition resulting from incoming sound. The traveling wave peaks at its characteristic frequency, stimulating inner hair cells to depolarize and causing auditory nerve fibers that are attached to IHCs to fire. Outer hair cells are important in this process because they amplify the incoming wave and sharpen the selectivity of the system. Basic mechanical and electrical properties of outer hair cells and surrounding structures were also described in Section 3. Then, a brief overview of previous work attempting to model and explain how outer hair cells can operate at frequencies beyond their membrane time constant was presented. Although previous endeavors on this topic have yielded many fruitful and interesting ideas, none have completely satisfied other researchers in the field.

Inspired by the simple feedback techniques used in mechanical motor systems, I developed a local outer hair cell model in Section 4. Since the outer hair cell is embedded between the reticular lamina and contracts when depolarized, it tends to pull the reticular lamina downwards and pull the basilar membrane upwards. The motion of the reticular lamina downwards tends to prevent further depolarization because the stereocilia of the OHCs are moved in the inhibitory direction. The motion of the basilar membrane upwards tends to increase depolarization since the stereocilia of the OHCs are moved in the excitatory direction. Thus, negative feedback is present around the reticular lamina while positive feedback is present on the basilar membrane. Since the stiffness of

the reticular lamina is 5-10 less than that of the basilar membrane, the RL moves a greater distance, making it likely that negative feedback is the dominant effect. To carry out the development of this model, I described systems with only a single resonator initially, one that had a dashpot to model the gap drag between the TM and the RL and the other that had an additional dashpot on the basilar membrane. To simplify analysis, I assumed that the reticular lamina had no mass in these initial systems. However, as shown in Section 4, these perfunctory models were unable to demonstrate a significant speedup of the membrane time constant and a sharpening of the mechanical response.

Thus, I introduced another mode of resonance into the system by adding an effective mass to the reticular lamina. The resulting two resonator model exhibited an input force to membrane voltage transfer function with two peaks that could provide sufficient membrane voltage for operation at appropriate frequencies. Furthermore, increased OHC gain resulted in a sharpening of the basilar membrane and reticular lamina transfer functions, which is expected from experimental data. Interestingly, the basilar membrane transfer function had two peaks in its magnitude plot; the first one sharpens with increased gain and is followed by a steep dip while the second one remains largely unaffected. The OHC's effect on the basilar membrane around the first peak is to create a capacitive component in the combined OHC and RL impedance looking in from the basilar membrane that can resonate with the spring-dominated basilar membrane in that regime as well as the inherent OHC spring and RL dashpot in that regime. This capacitor decreases with increasing OHC gain, which allows the peak and dip to move to a higher frequency and for the peak to have an increased Q value.

Section 5 described issues that are relevant to the construction of a full traveling-wave model, which is necessary to test the validity of the local OHC model. The dimensionality of the fluid mechanics and appropriate scaling of the parameters from base to apex are important in assembling an accurate model. A short description of a simple 1-D cochlear model was described and will be developed in the near future.

In order to compare the model to experimental data, empirical observations of vibrations of the cochlear partition and the basilar membrane were presented in Section 6. Neural and mechanical tuning curves were introduced as another way to verify or discard the model described here. Due to the lack of a full traveling-wave model, the local OHC model was compared to the local observations of Mammano and Ashmore [11] and could reproduce the data quite accurately.

This thesis has presented a possible solution to the slow OHC membrane time constant limitation on the high frequency operation of the cochlea amplifier. A two resonator model with negative feedback can provide a speedup of the membrane time constant. A near pole-zero cancellation further minimizes the effect of the time constant on the basilar membrane response. In addition, an increase of OHC gain can sharpen the mechanical response and lead to instability, which may be responsible for spontaneous otoacoustic emissions. However, many assumptions were made in order to simplify the first pass analysis of this system. These simplifications need to be justified or corrected in future revisions of this model. Thus, future work and potential issues were presented in Section 7 as a preview of what is to come. Section 8 provided eight key insights that were developed in this thesis about the operation of the local outer hair cell model. These

key insights are important for understanding speedup, selectivity, and amplification in the biological cochlea by the putative cochlear amplifier.

Perhaps the most important point that this thesis has attempted to convey is that the many years of accumulated knowledge and understanding of feedback systems in mechanical and electrical engineering can greatly enhance insight into the operation and dynamics of biological systems. Feedback theory can produce often counter-intuitive results such as the sharpening and amplification of resonant systems with increased loop gain in a *negative* feedback loop instead of a positive feedback loop or the increase in system speed by the use of negative feedback. Feedback is prevalent in many biological systems such as gene regulatory loops or in biomechanical control loops. Though biology is often nonlinear, a linearized analysis such as the one presented here may yield insight that would be otherwise missed with straightforward mathematical analysis or qualitative description, albeit at a certain operating point.

I used feedback analysis heavily in this thesis to describe the outer hair cell system to develop a local model that demonstrates that the slow membrane time constant can be sped up and almost cancelled out completely from the basilar membrane point of view. I conclude with the aspiration and hope that future work in this direction will alleviate the confusion surrounding the role of the outer hair cell as the putative cochlear amplifier.

10 References

[1] W.E. Brownell, A.A. Spector, R.M. Raphael, and A.S. Popel, "Micro- and Nanomechanics of the Cochlear Outer Hair Cell," *Annu. Rev. Biomed. Eng.,* vol. 3, pp. 169-194, 2001.

[2] P. Dallos and B. Fakler, "Prestin, a New Type of Motor Protein," *Nature Reviews Molecular Cell Biology,* vol. 3, pp. 104-111, 2002.

[3] P. Dallos and B. Evans, "High-Frequency Motility of Outer Hair Cells and the Cochlear Amplifier," *Science,* vol. 267, pp. 2006-2009, 1995.

[4] G. Frank, W. Hemmert, and A. Gummer, "Limiting Dynamics of High-Frequency Electromechanical Transduction of Outer Hair Cells," *PNAS,* vol. 96, pp. 4420-4425, 1999.

[5] K. Lundberg, *Control and Tangents for Feedback Systems.* Massachusetts Institute of Technology, 6.302 Feedback Systems Course Notes. Sep., 2003.

[6] C.D. Geisler, *From Sound to Synapse: Physiology of the Mammalian Ear.* New York, NY: Oxford University Press, 1998.

[7] L. Watts, "Cochlear Mechanics: Analysis and Analog VLSI," diss, California Institute of Technology, 1993.

[8] A.J. Hudspeth, Y. Choe, A.D. Mehta, and P. Martin, "Putting ion channels to work: Mechanoelectrical transduction, adaptation, and amplification by hair cells," *PNAS,* vol. 97, no. 22, Oct., pp. 11765-11772, 2000.

[9] P.G. Gillespie, "Molecular machinery of auditory and vestibular transduction," *Curr Opin Neurobiol,* vol. 5, Aug., pp. 449-455, 1995.

[10] B.J. Dannhof and V. Bruns, "The organ of Corti in the bat Hipposideros bicolor," *Hear. Res.,* vol. 53, no. 2, pp. 253-68, 1991.

[11] F. Mammano and J.F. Ashmore, "Reverse transduction measured in the isolated cochlea by laser Michelson interferometry," *Nature,* vol. 365, no. 6449, Oct. 28, pp. 838-841, 1993.

[12] G.K. Yates and D.L. Kirk, "Cochlear electrically evoked emissions modulated by mechanical transduction channels," *Journal of Neuroscience,* vol. 18, no. 6, pp. 1996-2003, 1998.

[13] D. Mountain and A. Hubbard, "A piezoelectric model of outer hair cell function," *Journal of the Acoustical Society of America*, vol. 95, no. 1, Jan., pp. 350-354, 1994.

[14] A. Spector, W. Brownell, and A. Popel, "Effect of outer hair cell piezoelectricity on high-frequency receptor potentials," *Journal of the Acoustical Society of America,* vol. 113, no. 1, Jan., pp. 453-461, 2003.

[15] A. Hubbard, "A Traveling-Wave Amplifier Model of the Cochlea," *Science,* vol. 259, Jan., pp. 68-71, 1993.

[16] M. Ospeck, X.X. Dong, and K.H. Iwasa, "Limiting Frequency of the Cochlear Amplifier Based on Electromotility of Outer Hair Cells," *Biophysical Journal,* vol. 84, Feb., pp. 739-749, 2003.

[17] P. Martin and A. Hudspeth, "Active hair-bundle movements can amplify a hair cell's response to oscillatory mechanical stimuli," *PNAS,* vol. 96, no. 25, Dec., pp. 14306-14311, 1999.

[18] A.J. Hudspeth, "Mechanical amplification of stimuli by hair cells," *Current Opinion in Neurobiology,* vol. 7, pp. 480-486, 1997.

[19] D.M. Freeman, C.C. Abnet, W. Hemmert, B.S. Tsai, and T.F. Weiss, "Dynamic Material Properties of the Tectorial Membrane: A Summary," *Hear. Res.,* submitted for publication, 2003.

[20] T. Gold, "The physical basis of the action of the cochlea," *Proc. Roy. Soc. (Lond.) B. Biol. Sci.,* vol. 135, pp. 492-498, 1948.

[21] G.K. Batchelor, *An Introduction to Fluid Dynamics.* Cambridge, UK: Cambridge University Press, 2000.

[22] A. Wright, "Dimensions of the cochlear stereocilia in man and the guinea pig," *Hear. Res.,* vol. 13, no. 1, pp. 89-98, 1984.

[23] R.D. Kamm, "Mechanics of the Cytoskeleton," Massachusetts Institute of Technology, BE.410J Molecular, Cellular, and Tissue Biomechanics Course Notes. May, 2003.

[24] P. Dallos, "Some Pending Problems in Cochlea Mechanics," in *Biophysics of the Cochlea,* A.W. Gummer, Ed. New Jersey: World Scientific, 2003, pp. 97-109.

[25] P. Dallos, personal communications, Nov. 3, 2003.

[26] C. Fernández, "Dimensions of the Cochlea (Guinea Pig)," *Journal of the Acoustical Society of America,* vol. 24, no. 5, Sep., pp. 519-523, 1952.

[27] I.J. Russell, G.P. Richardson, and A.R. Cody, "Mechanosensitivity of mammalian auditory hair cells *in vitro*," *Nature,* vol. 321, no. 6969, May 29, pp. 517-519, 1986.

[28] X.X. Dong, M. Ospeck, and K.H. Iwasa, "Piezoelectric Reciprocal Relationship of the Membrane Motor in the Cochlear Outer Hair Cell," *Biophysical Journal,* vol. 82, Mar., pp. 1254-1259, 2002.

[29] R. Hallworth, "Modulation of outer hair cell compliance and force by agents that affect hearing," *Hearing Research,* vol. 114, Dec., pp. 204-212, 1997.

[30] D. McFadden and H.S. Plattsmier, "Aspirin abolishes spontaneous oto-acoustic emissions," *Journal of the Acoustical Society of America,* vol. 76, no. 2, Aug., pp. 443-448, 1984.

[31] G.R. Long, A. Tubis, and K.L. Jones, "Modeling synchronization and suppression of spontaneous otoacoustic emissions using Van der Pol oscillators: Effects of aspirin administration," *Journal of the Acoustical Society of America,* vol. 89, no. 3, Mar., pp. 1201-1212, 1991.

[32] C.R. Steele, G.J. Baker, J.A. Tolomeo, and D.E. Zetes-Tolomeo, "Cochlear Mechanics," in *Biomedical Engineering Handbook,* J.D. Bronzino, Ed., D.J. Schneck, Section Ed. Boca Raton: CRC Press, 2000, pp. 35.1-35.15.

[33] D.D. Greenwood, "A cochlear frequency-position function for several species – 29 years later," *Journal of the Acoustical Society of America,* vol. 87, no. 6, Jun., pp. 2592-2605, 1990.

[34] "Earlab – Cochlear Frequency Placemaps," [Online document], 2003, [cited 2003 May 5], Available HTTP: http://earlab.bu.edu/anatomy/cochlea/Freq.aspx.

[35] P.J. Kolston, "The importance of phase data and model dimensionality to cochlea mechanics," *Hear Res,* vol. 145, no. 1-2, Jul., pp. 25-36, 2000.

[36] G. von Békésy, "On the Resonance Curve and the Decay Period at Various Points on the Cochlear Partition," *Journal of the Acoustical Society of America,* vol. 21, no. 3, May, pp. 245-254, 1949.

[37] W.S. Rhode, "Observations of the Vibration of the Basilar Membrane in Squirrel Monkeys using the Mössbauer Technique," *Journal of the Acoustical Society of America,* vol. 49, no. 4, Apr., pp. 1218-1231, 1971.

[38] W.S. Rhode, "Some observations on cochlear mechanics," *Journal of the Acoustical Society of America,* vol. 64, no. 1, Jul., pp. 158-176, 1978.

[39] M.A. Ruggero, N.C. Rich, L. Robles, and B.G. Shivapuja, "Middle-ear response in the chinchilla and its relationship to mechanics at the base of the cochlea," *Journal of the Acoustical Society of America,* vol. 87, no. 4, Apr., pp. 1612-1629, 1990.

[40] L. Robles and M.A. Ruggero, "Mechanics of the Mammalian Cochlea," *Physiological Reviews,* vol. 81, no. 3, Jul., pp. 1305-1352, 2001.

[41] S.S. Narayan, A.N. Temchin, A. Recio, and M.A. Ruggero, "Frequency Tuning of Basilar Membrane and Auditory Nerve Fibers in the Same Cochleae," *Science,* vol. 282, Dec., pp. 1882-1884, 1998.

[42] M.A. Ruggero, S.S. Narayan, A.N. Temchin, and A. Recio, "Mechanical bases of frequency tuning and neural excitation at the base of the cochlea: Comparison of basilar-membrane vibrations and auditory-nerve-fiber responses in chinchilla," *PNAS,* vol. 97, no. 22, Oct., pp. 11744-11750, 2000.

[43] "Earlab – Outer Hair Cell Dimensions," [Online document], 2003, [cited 2003 May 14], Available HTTP: http://earlab.bu.edu/anatomy/cochlea/OHCdimensions.aspx.

[44] G.D. Housley and J.F. Ashmore, "Ionic Currents of Outer Hair Cells Isolated from the Guinea-Pig Cochlea," *Journal of Physiology,* vol. 448, Mar., pp. 73-98, 1992.